

Iron complexes as electrocatalysts for the water oxidation reaction Kottrup, K.G.

Citation

Kottrup, K. G. (2018, February 28). *Iron complexes as electrocatalysts for the water oxidation reaction*. Retrieved from https://hdl.handle.net/1887/61046

Version: Not Applicable (or Unknown)

License: License agreement concerning inclusion of doctoral thesis in the

Institutional Repository of the University of Leiden

Downloaded from: https://hdl.handle.net/1887/61046

Note: To cite this publication please use the final published version (if applicable).

Cover Page



Universiteit Leiden



The handle http://hdl.handle.net/1887/61046 holds various files of this Leiden University dissertation

Author: Kottrup, Konstantin

Title: Iron complexes as electrocatalysts for the water oxidation reaction

Date: 2018-02-28

Iron complexes as electrocatalysts for the water oxidation reaction

PROEFSCHRIFT

Ter verkrijging van
de graad van Doctor aan de Universiteit Leiden,
op gezag van Rector Magnificus Prof. mr. C. J. J. M. Stolker,
volgens besluit van het College voor Promoties
te verdedigen op woensdag 28 Februari 2018
klokke 13:45 uur

door

Konstantin Georg Kottrup

geboren te Berlijn, Duitsland, 1988

Samenstelling Promotiecommissie

Promotor

Prof. Dr. E. Bouwman

Co-promotor

Dr. D. G. H. Hetterscheid

Overige Leden

Prof. Dr. M. T. M. Koper (Leiden University, The Netherlands)

Prof. Dr. H. S. Overkleeft (Leiden University, The Netherlands)

Prof. Dr. M. Costas (University of Girona, Spain)

Prof. Dr. B. de Bruin (University of Amsterdam, The Netherlands)

TABLE OF CONTENTS

Chapters

1.	Introduction9
2.	Investigation of structure-reactivity relationships of iron-based water oxidation catalysts with macrocyclic tetraaza-type ligands – an online electrochemical mass spectrometry approach
3.	Enhancement of the catalytic activity of a homogeneous iron-based water oxidation catalyst through substrate effects of graphitic electrodes
4.	Electrochemical versus chemical oxidation — re-evaluating the benchmark water oxidation catalyst α -[Fe(bpmcn)(OTf) ₂] via electroanalytical methods
5.	Interactions between metal complexes and the electrode surface – the influence of dissolved metal complexes on the surface of gold and graphitic carbon electrodes
6.	Summary, conclusions and outlook
	Appendices
A.	Supplementary information for Chapter 2
В.	Supplementary information for Chapter 3
C.	Supplementary information for Chapter 4 153
Samenvatting	
List of publications	
Curriculum Vitae	

LIST OF ABBREVIATIONS & SYMBOLS

Ligands

bpmcn *N,N'*-dimethyl-*N,N'*-bis(2-pyridylmethyl)-cyclohexane-1,2-diamine

bpy bipyridine

dba dibenzylideneacetone

dpa N,N-di(1,10-phenanthrolin-2-yl)-N-isopentylamine

Hbbpya N,N-bis(2,2'-bipyrid-6-yl)amine

L generic ligand

ppq 2-(pyrid-2'-yl)-8-(1",10"-phenanthrolin-2"-yl)-quinoline

TAML tetra-amido macrocyclic ligand

tpy terpyridine

Chemicals

BINAP 2,2'-bis(diphenylphosphino)-1,1'-binaphthyl

CAN cerium(IV) ammonium nitrate KOtBu potassium *tert*-butoxide

mCPBA meta-chloroperoxybenzoic acid

Et₂O diethyl ether OTf triflate anion

Spectroscopy and spectrometry

d doublet

dd doublet × doublet

ddd doublet × doublet × doublet

EPR electron paramagnetic resonance

ESI electrospray ionisation

IR infrared

J coupling constant

m multiplet

m/z mass-to-charge ratio MS mass spectrometry

NMR nuclear magnetic resonance

ppm parts per million

s sharp

SERS surface enhanced raman spectroscopy

t triplet
UV ultraviolet
vis visible

δ chemical shift

Electrochemistry

μA microampere

BDD boron-doped diamond CV cyclic voltammetry

EQCM electrochemical quarz crystal microbalance

FTO fluorine-doped tin oxide

GC glassy carbon

HOPG highly ordered pyrolytic graphite

ITO indium tin oxide

OLEMS on-line electrochemical mass spectrometry

PG pyrolytic graphite

RHE reversible hydrogen elecrode RRDE rotating ring-disc electrode

Other

μ prefix to indicate bridging ligands

a.u. arbitrary unitscf. comparee.g. for example

et al. et alii Fig. figure

FOTW foot of the wave

gram g h hour Hz hertz kelvin Κ M molar Me methyl milligram mg min minutes mL milliliter

MLCT metal-to-ligand charge-transfer

mM milimolar mmol millimol

OEC oxygen evolving complex

Ph phenyl

PSII photosystem II

s second

TOF turnover frequency turnover number

<u>Introduction</u>

In this chapter, the challenges which need to be overcome in order to move away from energy production relying on the unsustainable consumption of fossil fuels and towards a future of sustainable energy are discussed. In this context, recent advancements in the development of homogeneous water oxidation catalysts are outlined with a focus on catalysts based on first-row transition metals in general and iron in particular. Two aspects that receive particular attention are the importance of understanding structure-activity relationships in homogeneous water oxidation catalysis and the advantages and disadvantages of different methodologies for studying such catalysts. The latter aspect is explored by comparing the use of chemical oxidants — which is still a widely used standard in the field — to electrochemical techniques. This chapter is completed by a brief outline of the work presented in this thesis.

1.1 Challenges to overcome for a sustainable future

In 2014, humanity consumed a global total of 109 613 TWh of energy. [1] With the growth of modern societies, this global annual energy consumption is only going to increase in the future. [2] To meet this demand, energy production currently largely relies on the burning of fossil fuels, [1] which is problematic in several ways. Fossil fuels are formed in nature through extremely slow processes over millions of years and are therefore effectively finite as the rate of replenishment is much lower than the rate of consumption. Furthermore, burning these fuels releases among other pollutants - the carbon stored within them in the form of CO₂, raising the atmospheric levels of CO₂ and thereby contributing to anthropogenic climate change. [3] The gravity of these problems makes the development of new technologies, which allow us to move away from fossil fuels and towards a future of sustainable energy, one of the key challenges for science in the 21st century.^[4] While there are several sustainable sources of energy available such as wind, tides and geothermal heat, sunlight is the only sustainable source of energy which can be harvested in sufficient quantities to build a sustainable energy infrastructure on a global scale. [2] This makes solar energy a prime candidate for a long term solution to the impending energy crisis.

The technology for the conversion of solar energy to electricity already exists in the form of photovoltaics. However, fluctuations in the availability of sunlight due to clouds and day/night cycles and the uneven distribution of sunlight across the globe mean that additional technologies are required to not only capture energy from sunlight but to also store it. Ideally, solar energy would be stored in the form of chemical bonds through a solar-to-fuel conversion process since (liquid) fuels have considerably higher energy densities than other storage media such as batteries. [5] Moreover, not all existing technologies can be easily adapted from fuel to electricity.

Currently, the most promising approach to generating chemical fuels from solar energy is to oxidize water to produce oxygen and reduction equivalents in the form of protons and electrons. Water as a starting material is available in large quantities and O_2 as the only byproduct is environmentally friendly. The protons and electrons generated in such a process could subsequently be used for example to produce hydrogen gas or to generate more traditional carbon-based fuels through CO_2 reduction.

1.2 Natural vs. artificial photosynthesis

The formation of a chemical fuel from solar energy is sometimes referred to as "artificial photosynthesis", due to its conceptual analogy to the natural process of photosynthesis. [6-8] In natural photosynthesis, green plants and cyanobacteria use sunlight to generate biomass from CO₂ and water, releasing O₂ in the process. Natural photosynthesis is a highly complex process which can be divided into reactions which require light and reactions that occur in the dark. One of the essential pieces in the light-dependent part of photosynthesis is the oxygen evolving complex (OEC) in photosystem II (PSII). According to the best structural information currently available, the OEC contains four manganese centres, linked by bridging oxygen ligands, and one calcium ion which together form an Mn₄CaO₅ cluster. [9] While the exact mechanism is still a matter of some debate, [10-15] the OEC is capable of splitting water into oxygen as well as protons and electrons with remarkable efficiency. For the OEC itself, an overpotential of about 20 mV has been reported with respect to the thermodynamic standard potential for water splitting of 1.23 V. [16] However, when energy transport across the entire photosystem is taken into account, an effective overpotential for oxygen evolution of around 300-400 mV has been determined. [17-18] Similarly, the measured turnover frequency also depends on the exact conditions such as the intensity of the light and whether the measurement is conducted under in vivo or in vitro conditions. Accordingly, turnover frequencies of the order of 10¹ s⁻¹ to 10³ s⁻¹ have been reported. [18-20] Combined with turnover numbers of the order of 10^{5 [21]} this results in a net lifetime for PSII on the scale of minutes to hours, [22] after which PSII is so damaged from oxidative degradation that it is broken down and rebuilt inside the cell.

The electrons which are freed in the process of water oxidation are stored in the form of NADPH for the subsequent fixation of CO₂ in the form of carbohydrates in the light-independent part of photosynthesis.^[23]

Since the complexity of natural photosynthesis is clearly beyond the scope of current human-made technology, viable candidates for artificial photosynthesis are much simpler processes such as the splitting of water into hydrogen and oxygen.

The overall water splitting reaction consists of two parts, the oxidation of water and the reduction of protons, both of which need to be catalyzed (Fig. 1.1).

$$4 H^{+} + 4 e^{-} \longrightarrow 2 H_{2}$$
 $E^{\circ} = 0 V$

$$2 H_{2}O \longrightarrow O_{2} + 4 H^{+} + 4 e^{-}$$
 $E^{\circ} = 1.23 V$

$$2 H_{2}O \longrightarrow 2 H_{2} + O_{2}$$

Figure 1.1: Schematic representation of the overall water splitting reaction and its two half-reactions with their respective thermodynamic standard potentials.

Proton reduction is catalyzed very efficiently at virtually no overpotential by platinum metal. [24-25] Since platinum is a relatively scarce material, several other proton reduction catalysts based on more abundant materials have been and still are being developed. [26] Water oxidation on the other hand is a more complicated reaction as each turnover requires the rearrangement of four protons and four electrons, as well as the formation of an O–O bond, resulting in a kinetically very challenging reaction with several intermediates. [27] Because of these challenges, water oxidation is widely considered to be the bottleneck in developing water splitting processes. [28] Therefore water oxidation catalysis is still very much a research topic of great interest even after decades of research in this area.

Over the years, both homogeneous and heterogeneous catalysts for the water oxidation reaction have been developed with both areas having unique individual and often complementary strengths and weaknesses. [29] Heterogeneous catalysts in the form of e.g. metal oxides tend to be inherently more robust under strongly oxidizing conditions, resulting in generally higher turnover numbers compared to homogeneous catalysts. Homogeneous catalysts in the form of metal complexes on the other hand are more flexible in terms of their electronic and steric structures which makes it easier to employ rational design strategies. Additionally, the nature of active sites in heterogeneous catalysts is often poorly understood and their density on the catalyst surface is generally low whereas for homogeneous catalysts each individual complex in principle represents an active site which can be studied through spectroscopic techniques. Therefore, the main goal in homogeneous water oxidation catalysis is to understand structure-activity relationships of transition metal complexes for water oxidation.

1.3 Homogenoues water oxidation catalysts

The first example of a homogeneous water oxidation catalyst was published in 1982 by T. J. Meyer and co-workers. [30] The reported dimeric ruthenium complex $[(H_2O)Ru(bpy)_2-\mu-O-(bpy)_2Ru(H_2O)]$ (with bpy = bipyridine) is now commonly

known as the "blue dimer" thanks to its characteristic blue colour. Since the water oxidation reaction requires the catalyst to cycle through a fairly wide range of oxidation states and also due to the multinuclear nature of the OEC in PSII it was not until 2005 that it was realized that mononuclear complexes could also catalyze the water oxidation reaction. [31] Since then the field of homogeneous water oxidation catalysis has grown exponentially and a vast variety of different catalysts has been developed, based on many different transition metals, most prominently Ru, [31-39] Ir, [40-42] Fe, [43-58] Mn, [59-61] Co, [62-67] Ni [68-69] and Cu [70-74]. Even an example of an organic, metal-free water oxidation catalyst has been reported. [75] Of those aforementioned transition metals, catalysts based on ruthenium and iridium clearly stand out as being the most active ones in terms of turnover numbers, turnover frequencies and overpotentials. For ruthenium-based catalysts, turnover numbers as high as 10⁵-10⁶ have been reported. [39, 76] In terms of turnover frequencies, Llobet and co-workers determined the theoretical maximum TOF for their ruthenium-based system via foot-of-the-wave analysis and found values ranging from 8.000 to 50.000 s⁻¹ depending on the pH of the electrolyte solution. [38] Meanwhile, Crabtree and Brudvig have reported an iridium-based water oxidation system operating extremely close to the thermodynamic standard potential of water oxidation of 1.23 V. [42] From Tafel plots they extrapolated the onset potential of their catalyst to be only 14 mV above 1.23 V. While such a low overpotential is exceptional even for iridiumbased systems, other iridium-based systems have also been shown to operate at comparatively low overpotentials of less than 200 mV. [77]

In contrast to these excellent results, water oxidation catalysts based on the first-row transition metals Fe, Mn, Co, Ni and Cu generally yield considerably lower turnover frequencies and turnover numbers. Most of these systems operate at turnover frequencies below 1 s⁻¹ and show turnover numbers of the order of 10^0 - 10^2 . While a few exceptions exist, they all come with their own drawbacks. The Fe(bpmcn) system (with bpmcn = N,N'-dimethyl-N,N'-bis(2-pyridylmethyl)-cyclohexane-1,2-diamine) (Fig 1.2, left) reported by Costas et al. showed TON of >1000 under the right conditions but the corresponding TOF was low at only $0.06 \, \text{s}^{-1}$. More recently, Masaoka et al. reported a pentanuclear iron-based water oxidation catalyst (Fig. 1.2, middle) with an impressive TOF of 1.900 s⁻¹ and an estimated TON of >10⁷. However, this pentanuclear iron catalyst was found to be active only in acetonitrile solutions containing small amounts of water. In more water rich or aqueous environments the catalyst was found to be inactive.

For those first-row transition metal based catalysts that were studied electrochemically, overpotentials generally exceed 500 mV and faradaic efficiencies – if reported – are low. [43, 45, 53, 58, 64]

$$Fe^{\parallel}$$
 Fe^{\parallel}
 Fe^{\parallel}

Figure 1.2: Schematic representations of the structures of Fe(bpmcn) (left) and the pentanuclear iron cluster reported by Masaoka et al. (middle) and the ligand bridging the iron centres in the pentanuclear complex (right).

One concern that is always present when working with molecular catalysts under the harsh conditions that are required to achieve water oxidation, is the possibility of in situ formation of heterogeneous material as the true catalytically species.[29] Accordingly, heterogeneous active materials formed from homogeneous iron, manganese, cobalt, copper precursors have all been shown to be catalytically active. Consequently, one may falsely assume that one is studying an active homogeneous water oxidation catalyst when in fact minute amounts of heterogeneous material are being formed in situ which are responsible for part or even all of the observed catalytic activity. [79] When one wants to study the structure-activity relationships of homogeneous catalytic systems, it is therefore paramount to establish the molecular integrity of supposedly homogeneous water oxidation catalysts as part of routine experiments.

For those systems which have been found to be indeed molecular in nature, extensive investigations have revealed two dominant mechanistic pathways for the O–O bond formation step: (i) an intermolecular recombination of two metal oxo-species and (ii) a nucleophilic attack of water at the oxo ligand in a metal oxo intermediate (Fig. 1.3).^[84-88]

■ Bi-molecular O–O bond formation

$$M = \bigcirc \longrightarrow M =$$

■O–O bond formation via nucleophilic attack of water

$$M=O \xrightarrow{O-H} \xrightarrow{H^+} \xrightarrow{M-O} O-H$$

Figure 1.3: Schematic overview of the two main mechanisms of the O–O bond formation step in catalytic water oxidation (with M = metal)

Interestingly, the aforementioned ruthenium-based blue dimer was found to not undergo oxide coupling as one might expect based on the dinuclear structure. Instead, the mechanism is thought to proceed via a nucleophilic attack of water at one of the ruthenium oxo-sites in the [Ru $^{V}O(L)$ – μ -O–(L)Ru ^{V}O] intermediate which is aided by the abstraction of a proton from the incoming water molecule by the neighbouring ruthenium oxo-site (Fig. 1.4). [89] In fact, most homogeneous water oxidation catalysts are thought to catalyze water oxidation via a water nucleophilic attack mechanism. [84-88] An intermolecular recombination-type mechanism has so far only been found for a few ruthenium-based systems. [88]

Figure 1.4: Proposed mechanism of the O-O bond formation step of the blue dimer catalyst

1.4 Iron-based water oxidation catalysts

Even though water oxidation catalysts based on ruthenium and iridium show very promising results, the scarcity of these elements is prohibitive for a widespread application in solar fuels production. As a result, more and more attention has been given in recent years to the search for alternative catalysts based on more affordable and abundant first-row transition metals. Out of those first-row transition metals, iron is a prime candidate for the development of new water oxidation catalysts. Iron has a rich redox chemistry as is apparent from the availability of a wide range of accessible oxidation states from –IV to +VII. [90-91] Additionally, iron is present in many enzymes and metalloproteins found in

oxygen binding and oxygen transport systems in nature. However, while ruthenium and iridium tend to form predominantly low-spin complexes due to their position in the second and third row of the d-block, iron complexes are much more likely to adopt high-spin states. As a consequence, iron complexes tend to have more electron density in orbitals that are anti-bonding with respect to the metal–ligand bond, resulting in considerably faster ligand exchange kinetics for iron complexes compared to ruthenium and iridium. [92] This fundamental difference might explain at least in parts why first-row transition metal complexes in general and iron complexes in particular are generally deactivated significantly faster during water oxidation catalysis than iridium and ruthenium complexes, resulting in lower turnover numbers.

One of the first examples of homogeneous iron-based water oxidation catalysts that was reported in literature is comprised of the Fe-TAML complexes (TAML = tetra-amido macrocyclic ligand) (Fig. 1.5) which were developed by Collins et al. [46]

$$X_1$$
 X_2
 X_1
 X_2
 X_3
 X_4
 X_4
 X_4
 X_5
 X_5
 X_6
 X_7
 X_8
 X_8
 X_8
 X_8
 X_9
 X_9

Figure 1.5: Schematic representation of the structure of the Fe(TAML) system developed by Collins et al. with $X_1 = H$, NO_2 , Cl; $X_2 = H$, Cl; $R = CH_3$, $(CH_2)_2$, F; $Y = H_2O$

The TAML ligand platform was developed from rational ligand design to achieve maximum stability under strongly oxidative conditions. While the best Fe-TAML complex for water oxidation showed high initial-rate turnover frequencies of 1.3 s⁻¹ when driven by the sacrificial oxidant cerium(IV) ammonium nitrate (CAN), the activity was short-lived with only 16 turnovers. Several suggestions have been made about the cause of this rapid deactivation. Experimental studies conducted on a series of TAML complexes demonstrated that demetalation can occur in acidic media. [93] As a result, the loss of activity could at least in part be caused by degradation of the complex due to local acidification through protons generated in the water oxidation reaction. Theoretical calculations suggest the formation of a ligand-centered radical species which opens up degradation pathways. [94]
Substantially higher turnover numbers were reported in 2011 by Costas et al. for

their Fe(bpmcn) complex. [47] In the presence of excess CAN the complex

generated oxygen with a TOF of 0.23 s^{-1} for around 360 turnovers. By using periodate as the oxidant, instead of CAN, to drive the reaction the turnover number could be increased to around 1000 albeit at a lower rate of 0.06 s^{-1} .

One of the key findings Costas and co-workers reported was that the catalytic activity strongly depends on the coordination geometry of the complex. According to their results, iron complexes bearing neutral ligands with four nitrogen donor groups are active water oxidation catalysts if the complex has two available coordination sites in *cis*-position to each other. On the other hand, complexes with two available coordination sites in *trans*-position or complexes with only one available coordination site were found to be catalytically inactive (Fig. 1.6).

Figure 1.6: Schematic representation of the findings of Fillol et al. regarding the correlation between the coordination geometry of a complex and its catalytic activity towards water oxidation.

This finding was rationalized by invoking a mechanism which proceeds via an iron(V) oxo-hydroxo species (Fig. 1.7). In the proposed mechanism, the rate-limiting step is the O–O bond formation in the form of a nucleophilic attack of a water molecule at the oxo-ligand. This step is assumed to be facilitated by the abstraction of a proton from the incoming water molecule by the neighbouring hydroxo-ligand which acts as an internal base. The proposed mechanism was subsequently supported by DFT calculations. [95] The authors found that for the case of a *cis*-geometry the involvement of the neighbouring hydroxo-ligand indeed helps in the nucleophilic attack of water by accepting a proton from the incoming water molecule, leading to a reduced energy barrier of the O–O bond formation step compared to the *trans*-geometry for which O–O bond formation was found to be feasible only at significantly higher potentials.

Figure 1.7: Proposed mechanism of the O-O bond formation step of the Fe(bpmcn) catalyst

However, in 2015 Fillol and co-workers published a follow-up report in which they presented evidence for the formation of a Fe– μ -O–Ce species upon addition of stoichiometric amounts of CAN to the catalyst, raising questions about the actual mechanism under catalytic conditions in the presence of CAN. ^[96]

1.5 Chemical oxidants vs. electrochemistry

In order to achieve water oxidation, a driving force is needed which is strong enough to enable catalytic turnover. While water oxidation can in principle be driven chemically, photochemically and electrochemically, not all of these approaches are equally easy to implement. For the purpose of routine testing of new potential catalysts in the lab, the use of chemical oxidants to drive the catalyst is particularly attractive due to its ease of practical execution. Several chemical oxidants such as CAN or periodate are known to be capable of driving water oxidation catalysts^[97] and all that is required is to add an aqueous solution of the catalyst to an aqueous solution containing excess oxidant. The oxygen that is generated can be detected either in solution with the help of a Clark-type oxygen sensor or via headspace GC analysis. Because of this simplicity, chemical oxidants have been and still are routinely used for testing catalysts for the water oxidation reaction despite the fact that the results of such tests can only be considered very preliminary. The cost and waste associated with the use of stoichiometric amounts of chemical oxidants would make such a process economically unviable. Furthermore the original goal of producing a chemical fuel is also not achieved.

Unfortunately, the use of chemical oxidants is not without problems, even for mere routine testing purposes. The oxidants are generally only stable in a narrow pH region (e.g. around pH 1 for CAN) which means that the studies cannot necessarily be conducted at the pH which is most suitable for the catalyst. Furthermore, the potential which is applied in these cases is poorly defined. In the case of CAN, the potential is given by the relative concentration of Ce^{IV} to Ce^{III} according to the Nernst equation. At the beginning of the reaction, when only Ce^{IV} is present, the potential is therefore theoretically infinite. As the reaction proceeds and Ce^{III} is formed while Ce^{IV} is consumed, the potential also shifts over time. Therefore it is hardly possible to assess the overpotential of any given catalyst under such conditions. Finally, there has been more and more evidence in recent years which casts serious doubt about the nature of such chemical oxidants as mere innocent one-electron acceptors. In several cases it could be shown that

the oxidant is directly involved in the reaction mechanism. ^[96, 98-102] Therefore, the results obtained with chemical oxidants cannot be reliably generalized until one has established that the catalyst also functions in the absence of the oxidant, for example under electrochemical conditions.

An alternative method for the routine testing of water oxidation catalysts is by use of electrochemistry. Results obtained under electrochemical conditions are much more meaningful with respect to an actual application since the ambiguity caused by the presence of chemical oxidants is eliminated. Since it is already possible to convert solar energy into electricity via photovoltaics, a catalyst that works under electrochemical conditions could in principle be incorporated into a water splitting device that is driven by solar energy. In addition to this, electrochemistry also offers very practical advantages over the use of chemical oxidants such as more freedom in terms of reaction conditions (e.g. pH of the electrolyte) and much more precise control over the applied potential.

One aspect in electrochemical studies of water oxidation catalysts that has so far been largely overlooked in published literature is the role of the electrode material itself. In principle, electron transfer between the electrode and the catalyst can proceed via an outer sphere mechanism or an inner sphere mechanism. In the case of an outer sphere mechanism one would expect only a small influence of the electrode material. However, in the case of an inner sphere mechanism involving specific adsorption of the catalyst on the electrode surface a much more significant influence of the electrode material is to be expected. Despite the potentially significant influence of the electrode material on the catalytic results, only very few reports exist in literature in which the role of the electrode surface is discussed. [42, 75]

1.6 Aim and outline of this thesis

The goal of the research presented in this thesis is to provide insight into the redox behaviour of iron-based water oxidation catalysts, in particular under electrochemical conditions as opposed to conditions involving chemical oxidants. The intention behind this goal is to achieve a better understanding of what is required to make an active water oxidation catalyst. These requirements are assessed critically in this thesis by investigating the catalytic activities of different iron complexes under electrochemical conditions with respect to the structural and electronic properties of the complexes. Additionally, contributions from the

interplay of the electrode surface and the catalyst in solution receive strong consideration.

In chapter 2, three structurally related iron complexes are described for their capabilities in water oxidation catalysis. All three complexes have been studied electrochemically in both unbuffered electrolyte media and in the presence of a pH buffer. Their redox chemistry is investigated by cyclic voltammetry while their water oxidation capabilities have been studied with the help of on-line electrochemical mass spectrometry. Particular emphasis was also placed on obtaining evidence for the integrity of the molecular nature of the catalyst under operando conditions. The results for all three complexes are then compared to obtain insight into structure-activity relationships.

Following the findings of chapter 2, the synthesis and characterization of a second generation iron-based water oxidation catalyst in the form of a dinuclear iron complex is described in chapter 3. Avoiding halide ions in the structure of the complex allowed us to study the complex with several different electrode materials, revealing a strong substrate influence of the electrode material. This effect leads to a significant reduction in the overpotential required to achieve oxygen evolution in the case of electrodes made from graphitic carbon.

In chapter 4, the previously reported benchmark catalyst Fe(bpmcn)^[47] is revisited and investigated from an electrochemical perspective, using methodologies established in chapters 2 and 3. In particular, two isotopologues of the same complex, which have previously been found to display significantly different stabilities when driven with CAN, are compared in terms of their relative stability under electrochemical conditions.

The results discussed in chapters 3 and 4 show clear evidence for significant interactions between the surface of the working electrode and the complex in solution which go well beyond outer sphere electron transfer. Following these findings, the interactions of carbon and gold electrodes with metal complexes in solution have been studied in more detail with respect to the consequences for the electrode material, the results of which are described in chapter 5.

Finally, in chapter 6 a summary of the results discussed in this thesis is presented, followed by general conclusions about electroanalytical studies of iron-based water oxidation catalysts and an outlook for further research.

Parts of this thesis have already been published^[58] while other parts are submitted or in preparation for publication.

1.7 References

- [1] IEA, Key World Energy Statistics 2016
- http://www.iea.org/publications/freepublications/publication/KeyWorld2016.pdf (accessed 13-06-17 18:00)
- [2] N. S. Lewis; D. G. Nocera, Proc. Natl. Acad. Sci. U. S. A. 2006, 103, 15729-15735.
- [3] J. Chow; R. J. Kopp; P. R. Portney, *Science* **2003**, *302*, 1528-1531.
- [4] N. S. Lewis, Science 2007, 315, 798-801.
- [5] D. G. Nocera, ChemSusChem **2009**, 2, 387-390.
- [6] G. W. Crabtree; N. S. Lewis, Phys. Today 2007, 60, 37-42.
- [7] Y. Tachibana; L. Vayssieres; J. R. Durrant, Nat. Photonics 2012, 6, 511-518.
- [8] J. Barber, Chem. Soc. Rev. 2009, 38, 185-196.
- [9] Y. Umena; K. Kawakami; J. R. Shen; N. Kamiya, *Nature* **2011**, *473*, 55-60.
- [10] J. P. McEvoy; G. W. Brudvig, Chem. Rev. 2006, 106, 4455-4483.
- [11] G. W. Brudvig, Philos. Trans. R. Soc. Lond. B Biol. Sci. 2008, 363, 1211-1219.
- [12] M. M. Najafpour; S. Heidari; S. E. Balaghi; M. Hołyńska; M. H. Sadr; B. Soltani; M. Khatamian; A. W. Larkum; S. I. Allakhverdiev, *Biochim. Biophys. Acta, Bioenerg.* **2017**, *1858*, 156-174.
- [13] D. J. Vinyard; G. W. Brudvig, Annu. Rev. Phys. Chem. 2017, 68, 101-116.
- [14] J. R. Shen, Annu. Rev. Plant Biol. 2015, 66, 23-48.
- [15] P. E. M. Siegbahn, Proc. Natl. Acad. Sci. U. S. A. 2017, 114, 4966-4968.
- [16] M. Askerka; J. Wang; G. W. Brudvig; V. S. Batista, *Biochemistry* **2014**, *53*, 6860-6862.
- [17] H. Dau; I. Zaharieva, Acc. Chem. Res. 2009, 42, 1861-1870.
- [18] G. C. Dismukes; R. Brimblecombe; G. A. Felton; R. S. Pryadun; J. E. Sheats; L. Spiccia; G. F. Swiegers, *Acc. Chem. Res.* **2009**, *42*, 1935-1943.
- [19] D. Shevela; J. Messinger, *Biochim. Biophys. Acta* **2012**, *1817*, 1208-1212.
- [20] I. McConnell; G. Li; G. W. Brudvig, Chem. Biol. 2010, 17, 434-447.
- [21] H. Dau; C. Limberg; T. Reier; M. Risch; S. Roggan; P. Strasser, *ChemCatChem* **2010**, *2*, 724-761.
- [22] C. Vasilikiotis; A. Melis, Proc. Natl. Acad. Sci. U. S. A. 1994, 91, 7222-7226.
- [23] N. Bukhov; R. Carpentier, Photosynth. Res. 2004, 82, 17-33.
- [24] M. T. M. Koper, Nat. Chem. 2013, 5, 255-256.
- [25] J. K. Nørskov; T. Bligaard; A. Logadottir; J. R. Kitchin; J. G. Chen; S. Pandelov; U. Stimming, *J. Electrochem. Soc.* **2005**, *152*, J23.
- [26] R. M. Bullock; A. M. Appel; M. L. Helm, Chem. Commun. 2014, 50, 3125-3143.
- [27] M. T. M. Koper, Chem. Sci. 2013, 4, 2710.
- [28] H. Inoue; T. Shimada; Y. Kou; Y. Nabetani; D. Masui; S. Takagi; H. Tachibana, *ChemSusChem* **2011**, *4*, 173-179.
- [29] S. Fukuzumi; D. Hong, Eur. J. Inorg. Chem. 2014, 2014, 645-659.

- [30] S. W. Gersten; G. J. Samuels; T. J. Meyer, *J. Am. Chem. Soc.* **1982**, *104*, 4029-4030.
- [31] R. Zong; R. P. Thummel, J. Am. Chem. Soc. 2005, 127, 12802-12803.
- [32] Q. Daniel; L. Wang; L. Duan; F. Li; L. Sun, *Dalton Trans.* **2016**, *45*, 14689-14696.
- [33] Z. Lu; Y. Gao; H. Chen; Z. Liu; L. Chen; L. Sun, *Dalton Trans.* **2016**, *45*, 18459-18464.
- [34] L. Wang; K. Fan; Q. Daniel; L. Duan; F. Li; B. Philippe; H. Rensmo; H. Chen; J. Sun; L. Sun, *Chem. Commun.* **2015**, *51*, 7883-7886.
- [35] Y. Xie; D. W. Shaffer; A. Lewandowska-Andralojc; D. J. Szalda; J. J. Concepcion, *Angew. Chem., Int. Ed.* **2016**, *55*, 8067-8071.
- [36] J. J. Concepcion; J. W. Jurss; P. G. Hoertz; T. J. Meyer, *Angew. Chem., Int. Ed.* **2009**, *48*, 9473-9476.
- [37] L. Duan; F. Bozoglian; S. Mandal; B. Stewart; T. Privalov; A. Llobet; L. Sun, *Nat. Chem.* **2012**, *4*, 418-423.
- [38] R. Matheu; M. Z. Ertem; J. Benet-Buchholz; E. Coronado; V. S. Batista; X. Sala; A. Llobet, *J. Am. Chem. Soc.* **2015**, *137*, 10786-10795.
- [39] R. Staehle; L. Tong; L. Wang; L. Duan; A. Fischer; M. S. Ahlquist; L. Sun; S. Rau, *Inorg. Chem.* **2014**, *53*, 1307-1319.
- [40] O. Diaz-Morales; T. J. Hersbach; D. G. H. Hetterscheid; J. N. Reek; M. T. M. Koper, *J. Am. Chem. Soc.* **2014**, *136*, 10432-10439.
- [41] R. Lalrempuia; N. D. McDaniel; H. Muller-Bunz; S. Bernhard; M. Albrecht, *Angew. Chem., Int. Ed.* **2010**, *49*, 9765-9768.
- [42] S. W. Sheehan; J. M. Thomsen; U. Hintermair; R. H. Crabtree; G. W. Brudvig; C. A. Schmuttenmaer, *Nat. Commun.* **2015**, *6*, 6469.
- [43] M. K. Coggins; M. T. Zhang; A. K. Vannucci; C. J. Dares; T. J. Meyer, *J. Am. Chem. Soc.* **2014**, *136*, 5531-5534.
- [44] B. Das; B. L. Lee; E. A. Karlsson; T. Akermark; A. Shatskiy; S. Demeshko; R. Z. Liao; T. M. Laine; M. Haukka; E. Zeglio; A. F. Abdel-Magied; P. E. Siegbahn; F. Meyer; M. D. Karkas; E. V. Johnston; E. Nordlander; B. Akermark, *Dalton Trans.* **2016**, *45*, 13289-13293.
- [45] E. L. Demeter; S. L. Hilburg; N. R. Washburn; T. J. Collins; J. R. Kitchin, *J. Am. Chem. Soc.* **2014**, *136*, 5603-5606.
- [46] W. C. Ellis; N. D. McDaniel; S. Bernhard; T. J. Collins, *J. Am. Chem. Soc.* **2010**, *132*, 10990-10991.
- [47] J. L. Fillol; Z. Codola; I. Garcia-Bosch; L. Gomez; J. J. Pla; M. Costas, *Nat. Chem.* **2011**, *3*, 807-813.
- [48] W. A. Hoffert; M. T. Mock; A. M. Appel; J. Y. Yang, Eur. J. Inorg. Chem. **2013**, 2013, 3846-3857.
- [49] M. M. Najafpour; A. N. Moghaddam; D. J. Sedigh; M. Hołyńska, *Catal. Sci. Technol.* **2014**, *4*, 30-33.

- [50] M. Okamura; M. Kondo; R. Kuga; Y. Kurashige; T. Yanai; S. Hayami; V. K. Praneeth; M. Yoshida; K. Yoneda; S. Kawata; S. Masaoka, *Nature* **2016**, *530*, 465-468.
- [51] G. Panchbhai; W. M. Singh; B. Das; R. T. Jane; A. Thapper, *Eur. J. Inorg. Chem.* **2016**, *2016*, 3262-3268.
- [52] A. R. Parent; T. Nakazono; S. Lin; S. Utsunomiya; K. Sakai, *Dalton Trans.* **2014**, *43*, 12501-12513.
- [53] P. Tan; H. K. Kwong; T. C. Lau, Chem. Commun. 2015, 51, 12189-12192.
- [54] D. Wang; L. Que, Jr., Chem. Commun. 2013, 49, 10682-10684.
- [55] Z.-Q. Wang; Z.-C. Wang; S. Zhan; J.-S. Ye, Appl. Catal., A 2015, 490, 128-132.
- [56] L. D. Wickramasinghe; R. Zhou; R. Zong; P. Vo; K. J. Gagnon; R. P. Thummel, *J. Am. Chem. Soc.* **2015**, *137*, 13260-13263.
- [57] B. Zhang; F. Li; F. Yu; H. Cui; X. Zhou; H. Li; Y. Wang; L. Sun, *Chem. Asian J.* **2014**, *9*, 1515-1518.
- [58] K. G. Kottrup; D. G. H. Hetterscheid, Chem. Commun. 2016, 52, 2643-2646.
- [59] Y. Gao; R. H. Crabtree; G. W. Brudvig, *Inorg. Chem.* **2012**, *51*, 4043-4050.
- [60] Y. Gao; J. Liu; M. Wang; Y. Na; B. Åkermark; L. Sun, *Tetrahedron* **2007**, *63*, 1987-1994.
- [61] W. T. Lee; S. B. Munoz, 3rd; D. A. Dickie; J. M. Smith, *Angew. Chem., Int. Ed.* **2014**, *53*, 9856-9859.
- [62] T. Abe; K. Nagai; S. Kabutomori; M. Kaneko; A. Tajiri; T. Norimatsu, *Angew. Chem., Int. Ed.* **2006**, *45*, 2778-2781.
- [63] M. Chen; S. M. Ng; S. M. Yiu; K. C. Lau; R. J. Zeng; T. C. Lau, *Chem. Commun.* **2014**, *50*, 14956-14959.
- [64] D. K. Dogutan; R. McGuire, Jr.; D. G. Nocera, *J. Am. Chem. Soc.* **2011**, *133*, 9178-9180.
- [65] T. Ishizuka; A. Watanabe; H. Kotani; D. Hong; K. Satonaka; T. Wada; Y. Shiota; K. Yoshizawa; K. Ohara; K. Yamaguchi; S. Kato; S. Fukuzumi; T. Kojima, *Inorg. Chem.* **2016**, *55*, 1154-1164.
- [66] T. Nakazono; A. R. Parent; K. Sakai, Chem. Commun. 2013, 49, 6325-6327.
- [67] Y. Zhao; J. Lin; Y. Liu; B. Ma; Y. Ding; M. Chen, *Chem. Commun.* **2015**, *51*, 17309-17312.
- [68] J. Masud; P. C. Ioannou; N. Levesanos; P. Kyritsis; M. Nath, *ChemSusChem* **2016**, *9*, 3128-3132.
- [69] J.-W. Wang; X.-Q. Zhang; H.-H. Huang; T.-B. Lu, *ChemCatChem* **2016**, *8*, 3287-3293.
- [70] S. M. Barnett; K. I. Goldberg; J. M. Mayer, Nat. Chem. 2012, 4, 498-502.
- [71] P. Garrido-Barros; I. Funes-Ardoiz; S. Drouet; J. Benet-Buchholz; F. Maseras; A. Llobet, *J. Am. Chem. Soc.* **2015**, *137*, 6758-6761.
- [72] X. J. Su; M. Gao; L. Jiao; R. Z. Liao; P. E. Siegbahn; J. P. Cheng; M. T. Zhang, *Angew. Chem., Int. Ed.* **2015**, *54*, 4909-4914.

- [73] F. Yu; F. Li; J. Hu; L. Bai; Y. Zhu; L. Sun, *Chem. Commun.* **2016**, *52*, 10377-10380.
- [74] T. Zhang; C. Wang; S. Liu; J. L. Wang; W. Lin, J. Am. Chem. Soc. **2014**, 136, 273-281.
- [75] E. Mirzakulova; R. Khatmullin; J. Walpita; T. Corrigan; N. M. Vargas-Barbosa; S. Vyas; S. Oottikkal; S. F. Manzer; C. M. Hadad; K. D. Glusac, *Nat. Chem.* **2012**, *4*, 794-801.
- [76] J. Creus; R. Matheu; I. Penafiel; D. Moonshiram; P. Blondeau; J. Benet-Buchholz; J. Garcia-Anton; X. Sala; C. Godard; A. Llobet, *Angew. Chem., Int. Ed.* **2016**, *55*, 15382-15386.
- [77] Y. Tamaki; A. K. Vannucci; C. J. Dares; R. A. Binstead; T. J. Meyer, *J. Am. Chem. Soc.* **2014**, *136*, 6854-6857.
- [78] D. G. H. Hetterscheid; J. N. Reek, Angew. Chem., Int. Ed. 2012, 51, 9740-9747.
- [79] M. M. Najafpour; R. Safdari; F. Ebrahimi; P. Rafighi; R. Bagheri, *Dalton Trans.* **2016**, *45*, 2618-2623.
- [80] M. M. Najafpour; A. N. Moghaddam, Dalton Trans. 2012, 41, 10292-10297.
- [81] S. Duraisamy; H. Kim; W. Shin, Int. J. Hydrogen Energy 2017, 42, 7908-7916.
- [82] C. J. M. van der Ham; F. Işık; T. W. G. M. Verhoeven; J. W. Niemantsverdriet; D. G. H. Hetterscheid, *Catal. Today* **2017**, *290*, 33-38.
- [83] P. Abril; M. P. del Río; C. Tejel; T. W. G. M. Verhoeven; J. W. H. Niemantsverdriet; C. J. M. Van der Ham; K. G. Kottrup; D. G. H. Hetterscheid, *ACS Catal.* **2016**, *6*, 7872-7875.
- [84] J. D. Blakemore; R. H. Crabtree; G. W. Brudvig, *Chem. Rev.* **2015**, *115*, 12974-13005.
- [85] M. D. Karkas; O. Verho; E. V. Johnston; B. Akermark, *Chem. Rev.* **2014**, *114*, 11863-12001.
- [86] M. D. Karkas; B. Akermark, Dalton Trans. 2016, 45, 14421-14461.
- [87] S. Berardi; S. Drouet; L. Francas; C. Gimbert-Surinach; M. Guttentag; C. Richmond; T. Stoll; A. Llobet, *Chem. Soc. Rev.* **2014**, *43*, 7501-7519.
- [88] D. J. Wasylenko; R. D. Palmer; C. P. Berlinguette, *Chem. Commun.* **2013**, *49*, 218-227.
- [89] F. Liu; J. J. Concepcion; J. W. Jurss; T. Cardolaccia; J. L. Templeton; T. J. Meyer, *Inorg. Chem.* **2008**, *47*, 1727-1752.
- [90] J. Köhler; M.-H. Whangbo, Solid State Sci. 2008, 10, 444-449.
- [91] J. B. Lu; J. Jian; W. Huang; H. Lin; J. Li; M. Zhou, *Phys. Chem. Chem. Phys.* **2016**, *18*, 31125-31131.
- [92] J. Reedijk, *Platinum Metals Review* **2008**, *52*, 2-11.
- [93] A. Ghosh; A. D. Ryabov; S. M. Mayer; D. C. Horner; D. E. Prasuhn, Jr.; S. Sen Gupta; L. Vuocolo; C. Culver; M. P. Hendrich; C. E. Rickard; R. E. Norman; C. P. Horwitz; T. J. Collins, *J. Am. Chem. Soc.* **2003**, *125*, 12378-12379.
- [94] R.-Z. Liao; X.-C. Li; P. E. M. Siegbahn, Eur. J. Inorg. Chem. 2014, 2014, 728-741.

- [95] F. Acuna-Pares; Z. Codola; M. Costas; J. M. Luis; J. Lloret-Fillol, *Chem. Eur. J.* **2014**, *20*, 5696-5707.
- [96] Z. Codola; L. Gomez; S. T. Kleespies; L. Que, Jr.; M. Costas; J. Lloret-Fillol, *Nat. Commun.* **2015**, *6*, 5865.
- [97] A. R. Parent; R. H. Crabtree; G. W. Brudvig, *Chem. Soc. Rev.* **2013**, *42*, 2247-2252.
- [98] I. Pecht; Z. Luz, J. Am. Chem. Soc. 1965, 87, 4068-4072.
- [99] T. J. Demars; M. K. Bera; S. Seifert; M. R. Antonio; R. J. Ellis, *Angew. Chem., Int. Ed.* **2015**, *54*, 7534-7538.
- [100] D. G. H. Hetterscheid; J. N. H. Reek, Eur. J. Inorg. Chem. 2014, 2014, 742-749.
- [101] D. J. Wasylenko; C. Ganesamoorthy; M. A. Henderson; C. P. Berlinguette, *Inorg. Chem.* **2011**, *50*, 3662-3672.
- [102] M. Yoshida; S. Masaoka; J. Abe; K. Sakai, *Chem. Asian J.* **2010**, *5*, 2369-2378.

Investigation of structure-reactivity relationships of iron-based water oxidation catalysts with macrocyclic tetraaza-type ligands – an online electrochemical mass spectrometry approach

The use of on-line electrochemical mass spectrometry in combination with classical electroanalytical techniques makes it possible to distinguish between competing reactions such as water oxidation and the formation of carbon dioxide at high electrochemical potentials. In this chapter, a selection of three different iron complexes based on the macrocyclic tetraaza-type ligand cyclam is examined using this methodology. For the complex cis-[Fe(cyclam)Cl₂]Cl (1) water oxidation activity was found which is in agreement with previous studies that predict iron complexes based on neutral amine ligands with two vacant coordination sites in cis configuration to be active catalysts for water oxidation. The complex [Fe(cyclamacetate)Cl] (2) bearing an additional 5th donor ligand in axial position in the form of an acetate group was also found to be an active catalyst for the water oxidation reaction. Meanwhile, the complex trans-[Fe(cyclam)Cl₂] (3) which was predicted to be inactive for water oxidation indeed shows very little catalytic activity up until 2.0 V under the same conditions. The results presented in this chapter suggest the presence of a strong correlation between the electronic structure of the iron centre and the observed water oxidation activity.

2.1 Introduction

Since fossil fuel reserves are dwindling and CO₂ emissions from fossil fuel consumption contribute to human-made climate change, new technologies are needed to ensure a sustainable energy future. To produce chemical fuels in a sustainable way, electrons are needed in order to reduce substrates such as CO₂ or protons to fuel. A cheap and abundant source of electrons is water, however, this requires a catalyst for the water oxidation reaction. In order to ultimately achieve fuel production on a global scale by means of oxidizing water, a water oxidation catalyst needs to be not only sufficiently efficient and robust but also made from affordable and abundant materials. While excellent catalysts have been developed based on iridium and ruthenium, [1-4] these materials are too scarce and too expensive to be implemented on a large scale. To address this issue, in recent years more and more attention has been given to the development of new catalysts based on more abundant first-row transition metals such as iron, cobalt, nickel, manganese and copper. [5-6] Of those elements, iron in particular has received a lot of interest due to its ability to access a wide range of oxidation states and its importance in oxygen-binding systems in nature.

However, the structure-reactivity relationships that enable efficient, low overpotential water oxidation catalysis based on iron, which are important for the design of new and efficient catalysts, are still not fully understood. In 2011, Fillol et al. reported on a series of iron-based water oxidation catalysts with tetradentate amine ligands. [7] Their key finding was that those complexes which have two vacant coordination sites in cis-configuration are active water oxidation catalysts while a structure with two vacant coordination sites in trans-positions leads to a catalytically inactive complex. In contrast to that, Collins et al. reported in 2010 that iron-TAML complexes which do not have two vacant sites in cispositions do show water oxidation activity – albeit short lived – with remarkably high turnover frequencies. [8] This juxtaposition already indicates that other factors must also play a role in determining the catalytic activity of a given complex aside from its geometry. Fillol and co-workers were able to support their proposed mechanism involving cis vacant sites through subsequent DFT calculations. [9] However, in a follow-up publication they reported that the use of the sacrificial oxidant cerium(IV) ammonium nitrate (CAN) to drive the reaction results in the formation of a Fe- μ -O-Ce species, [10] suggesting a direct involvement of the oxidant in the catalytic mechanism.

Intrigued by these findings we synthesized a selection of iron-based complexes with different structural motifs and investigated their redox behaviour and their water oxidation capabilities by means of electroanalytical techniques.

Despite their possibly limited stability under highly oxidative conditions, macrocyclic cyclam-based ligands (Fig. 2.1) were selected in this study for complexation to iron because such complexes are expected to be relatively stable towards ligand dissociation and the corresponding iron complexes bearing vacant sites in *cis*- and *trans*-configuration have been synthesized^[11] and used in oxidation chemistry^[12] previously. Furthermore, previous studies have suggested that macrocyclic ligands can enable catalytic water oxidation activity of iron complexes in some cases.^[13] The results of the experiments discussed in this chapter show no considerable catalytic activity for *trans*-[Fe(cyclam)Cl₂] (3). In contrast, the complexes *cis*-[Fe(cyclam)Cl₂]Cl (1) and [Fe(cyclamacetate)Cl] (2) are found to be capable of catalyzing the water oxidation reaction. To the best of our knowledge, [Fe(cyclamacetate)Cl] (2) is the first iron-based water oxidation electrocatalyst with only one free coordination site which is active in aqueous media.

Figure 2.1: Structures of complexes 1, 2 and 3

2.2 Results and Discussion

2.2.1 Synthesis and characterization

Cis-[Fe(cyclam)Cl₂]Cl (1) was synthesized according to literature procedures.^[11] The complex was isolated as orange crystals of high purity, which was confirmed by elemental analysis. Whereas complex 1 was obtained as a Fe^{III} species, the complexes 2 and 3 were isolated as Fe^{III} species and oxidized to the Fe^{III} species *in situ* prior to electrochemical experiments.

Complex 2 can be isolated as a white powder and oxygen-free solutions of 2 in acetonitrile, water and methanol are all colourless which is indicative of a high-

spin Fe^{II} configuration. Upon exposure to air, solutions of complex **2** quickly turn (dark) yellow indicating oxidation from Fe^{II} to Fe^{III}. EPR-measurements indicate that complex **2** is EPR-silent (X-band), which is not uncommon for high-spin iron(II) species. After exposure of the aqueous solution to air, the oxidized complex yields an EPR spectrum with three distinct g-values of 2.48, 2.21 and 1.89 (Fig. A.1a, Appendix A) which is in good agreement with previous reports. For the C=O stretch vibration of the carboxyl group, a shift of 139 cm⁻¹ was observed by comparing the IR spectra of the ligand and complex **2**, suggesting that the acetate group coordinates to the iron-centre in the solid state (Fig. A.2, Appendix A).

The Fe^{III} trans-analogue of complex **1** has been reported previously.^[11] However, the complex was isolated as a [FeCl₄]⁻ salt and attempts to recrystallize it with other counter-ions proved to be difficult. To avoid the presence of any [FeCl₄]⁻ in the catalytic experiments, a different approach was taken instead. *Trans*-[Fe(cyclam)Cl₂] (**3**) was synthesized as the Fe^{II} species in a procedure analogous to that of complex **2** and was isolated as a light pink powder.

Previous reports show that the iron-centre in complex 1 is in the high-spin state whereas the analogous *trans*-species has a low-spin Fe^{III} centre due to a Jahn-Teller distortion. In the EPR spectrum obtained for the oxidized form of complex 3 (Fig. A.1b, Appendix A), the predominant signal shows g-values of 2.39, 2.24 and 1.93, which suggests that the major species present in solution has a similar structure to the oxidized form of complex 2, indicating the desired *trans*-configuration. Next to the main signal, the EPR spectrum of 3 also shows 2 additional minor signals which might arise from traces of the *cis*-conformer or traces of residual FeCl₂ in the sample. The presence of chloride ions and glycerol in the sample further complicate the system and may cause unexpected signals.

UV-vis experiments of complexes **1** and **3** in aqueous solution show that the absorption spectrum of complex **1** remains stable over the course of at least 90 minutes while the spectrum of complex **3** changes notably, most likely due to oxidation from the Fe^{III} to the Fe^{III} oxidation state in air. Comparison of the UV-vis spectra of both complexes also shows that the spectra remain distinctly different for both complexes, showing that no significant interconversion between the *cis* and the *trans* species takes place under these conditions (Fig. A.3, Appendix A).

2.2.2 Electrochemical studies

2.2.2a General

The redox behaviour and catalytic activity of cis-[Fe(cyclam)Cl₂]Cl (1), [Fe(cyclamacetate)Cl] (2) and trans-[Fe(cyclam)Cl₂] (3) were studied via electroanalytical techniques using a pyrolytic graphite (PG) working electrode in aqueous solutions of either unbuffered 0.1 M NaClO₄ or 0.1 M phosphate buffer (pH 7.5). Electrochemical experiments using acidic media (pH 1) yielded poor results and preliminary tests with chemical oxidants showed only low single digit turnover numbers and rapid catalyst deactivation. We refrained from catalytic studies under very alkaline conditions to avoid formation of iron oxide which could potentially obscure catalytic activity of the molecular complexes. [16] To investigate whether the catalytic results depend on the electrode of choice, we tested working electrodes made from gold as well as PG. Gold electrodes form a layer of gold oxide on the surface, starting around 1.2-1.3 V vs. a reversible hydrogen electrode (RHE). The gold oxide surface is not stable in the presence of chloride ions, resulting in the formation of [AuCl₄] which gives rise to a large current between 1.2 and 1.6 V vs. RHE which potentially obscures other features in the CV (Fig. 2.2). Additionally, it has been proposed that the presence of halide ions can interfere with the mechanism of the water oxidation reaction.^[17] Since isolation of complexes 1-3 with different counter ions proved to be difficult, PG was selected as the best electrode material for our purposes since the presence of chloride ions seems to have no significant effect on the resulting CV (Fig. 2.3).

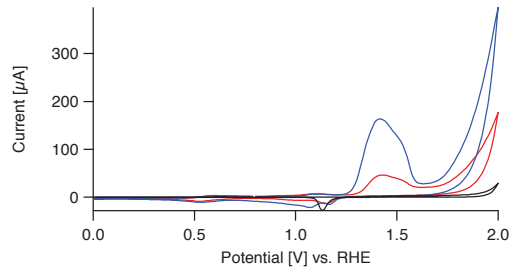


Figure 2.2: Voltammogram showing a blank gold working electrode (black) and a gold working electrode in the presence of complex **1** without (red) and with the addition of 6 eq. NaCl (blue). The current of the oxidation peak at $^{\sim}1.4$ V vs. RHE correlates directly with the concentration of Cl $^{-}$ ions. Conditions: 0.1 M NaClO₄, 1.1 mM complex **1**, scan rate 10 mV/s.

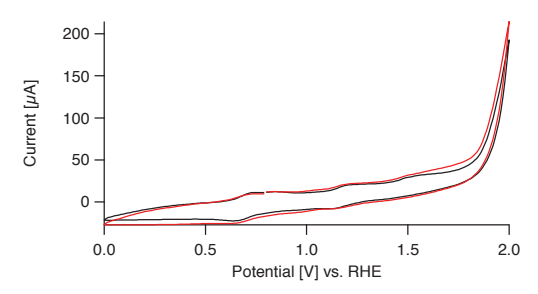


Figure 2.3: Voltammograms of complex **1**, using a PG working electrode with and without added NaCl. The black line represents the voltammogram of complex **1** using a PG working electrode, the red line represents the voltammogram after the addition of 6 eq. NaCl. In contrast to the observed chloride oxidation on gold (cf. Fig. 2.2), the addition of several equivalents of NaCl produces no significant difference in the voltammogram recorded for complex **1** with a PG working electrode. Conditions: 0.1 M NaClO₄, 1.1 mM complex **1**, scan rate 10 mV/s.

2.2.2b Electrochemical studies in unbuffered solution

In an unbuffered 0.1 M NaClO₄ solution, complex **1** shows a reversible wave at 0.7 V which is assigned to the Fe^{II/III} couple (Fig. 2.4a). At 1.2 V vs. RHE another redox couple can be seen in the CV as well as an irreversible oxidative wave at 1.5 V vs. RHE. Starting at about 1.8 V, a sharp increase in current is observed in the voltammogram (Fig. 2.4b).

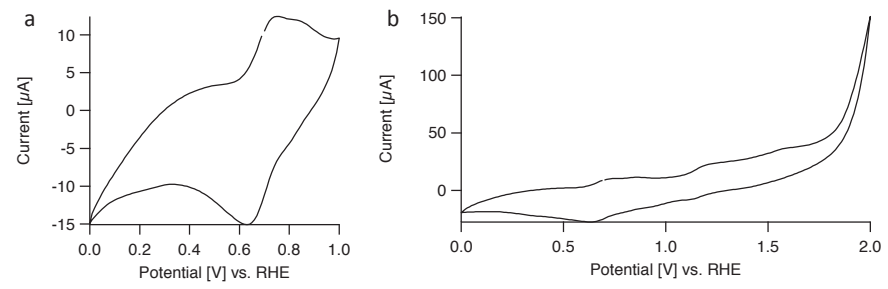


Figure 2.4: Results of a CV measurement of 1.1 mM complex 1 using a PG working electrode in a 0.1 M NaClO₄ solution measured at 10 mV/s with a starting potential of 0.7 V vs. RHE with a scan range of (a) 0.0 to 1.0 V vs. RHE and (b) 0.0 to 2.0 V vs. RHE.

To identify the products formed upon electrochemical oxidation and to determine the onset potentials of these reactions, online electrochemical mass spectrometry (OLEMS) was used. In OLEMS measurements, the m/z traces for selected gaseous products, sampled close to the electrode surface in solution, are recorded during electrochemical measurements. In chronoamperometry measurements at 1.9 V, immediate O_2 evolution was detected via OLEMS, without any induction period or any CO_2 formation preceding the onset of O_2 evolution (Fig. 2.5a). This indicates that the catalytic reaction is mediated by a molecular species. The mass trace of

 O_2 was also measured as a function of potential to determine the onset potential for O_2 evolution. Following the recorded traces for m/z = 32 (Fig. 2.6a), an increase in signal can be observed indicating the formation of dioxygen starting near 1.8 V which correlates with the sharp onset of oxidative current seen in the CV. Additionally, the trace of m/z = 44 was measured to monitor the formation of CO_2 which is expected to be a product of oxidative decomposition of the ligand. Comparison of the mass traces shows that the formation of CO_2 starts at lower potentials than the evolution of O_2 (Fig. 2.6a).

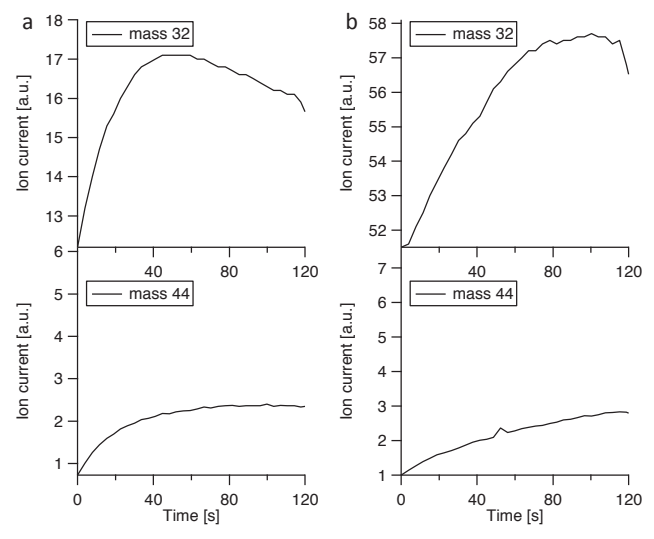


Figure 2.5: m/z traces of O_2 (top) and CO_2 (bottom) recorded during chronoamperometry measurements in a 0.1 M NaClO₄ solution with 1.1 mM of (a) complex **1** at 1.9 V vs. RHE and (b) complex **2** at 2.0 V vs. RHE.

The formation of CO_2 points to a weakness of the ligand framework under these oxidizing conditions. This finding is in line with the results of previous reports of iron-based molecular catalysts for water oxidation which generally show low Faradaic efficiencies or low turn-over numbers.^[7, 13, 18] It has to be noted that the observed CO_2 may originate at least in part from oxidation of the carbon electrode itself, mediated by the presence of high-valent iron oxo-species. To get further insight into the catalyst stability, cyclic voltammetry was performed in the presence of complex 1, followed by chronoamperometry for 180 s at 1.9 V vs. RHE, immediately followed by another cyclic voltammetry run, starting with a cathodic scan from 2.0 V to 0.0 V vs. RHE. The voltammogram recorded before and after chronoamperometry experiment are almost superimposable, except for an increase in reductive current between 0.5 V and 0.0 V vs. RHE (Fig. 2.7), which

most likely stems from the reduction of the dioxygen produced during the chronoamperometry experiment and a slightly increased oxidative current beyond 1.5 V which is ascribed to oxidative modification of the PG electrode under high potential conditions. Aside from the reductive current below 0.5 V and a slightly higher oxidative current beyond 1.5 V, the basic features of the CV are identical before and after the chronoamperometry experiment, indicating that the complex remains mostly intact. It is to be expected that diffusion of unreacted complex from the bulk solution to the electrode surface will mask the effect of catalyst decomposition to some extent. However, from these results the catalyst appears to be reasonably stable within the time span of the experiments.

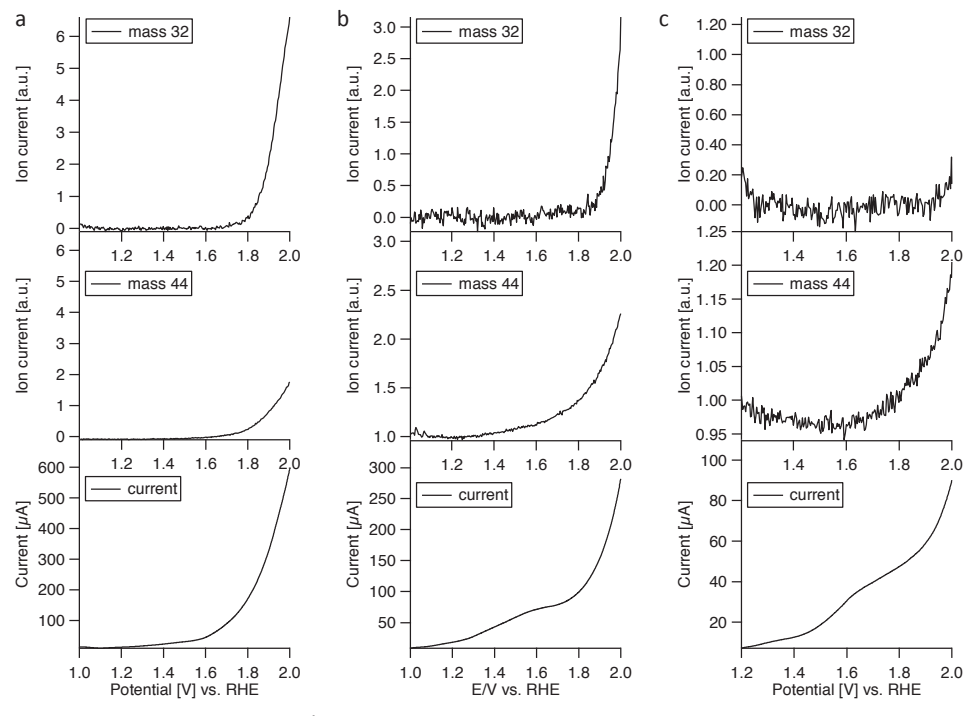


Figure 2.6: Shown are the m/z traces of O_2 (top), CO_2 (middle) and the corresponding current (bottom) of OLEMS measurements recorded during electrochemical potential cycling at 1 mV/s. For the sake of clarity, only the forward scan of each experiment is depicted. Conditions: (a) 1.1 mM complex 1 in a 0.1 M NaClO₄ solution, scanning between 1.0 and 2.0 V vs. RHE, starting at 1.0 V vs. RHE. (b) 1.1 mM complex 2 in a 0.1 M NaClO₄ solution, scanning between 1.0 and 2.0 V vs. RHE, starting at 1.0 V vs. RHE. (c) 1.1 mM complex 3 in a 0.1 M NaClO₄ solution, scanning between 1.2 and 2.0 V vs. RHE, starting at 1.2 V vs. RHE.

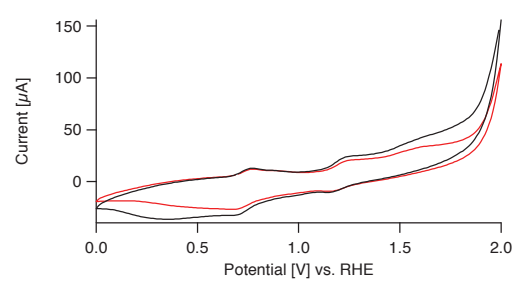


Figure 2.7: Comparison of voltammograms of 1.1 mM complex $\bf 1$ in a 0.1 M NaClO₄ solution at a scan rate of 10 mV/s before (red) and after (black) chronoamperometry (180 s at 1.9 V).

Similar to complex **1**, complex **2** shows a reversible $Fe^{\parallel/\parallel}$ redox-couple at 0.7 V (Fig. 2.8a). Starting at 1.3 V, an irreversible oxidative current can be observed in the voltammogram with a sharp increase in current starting at 1.8 V (Fig. 2.8b).

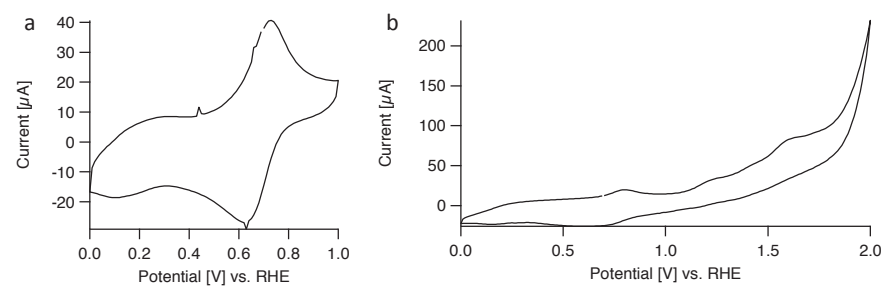


Figure 2.8: Results of a CV measurement of 1.1 mM complex 2 using a PG working electrode in a 0.1 M NaClO₄ solution measured at 10 mV/s with a starting potential of 0.7 V vs. RHE with a scan range of (a) 0.0 to 1.0 V vs. RHE and (b) 0.0 to 2.0 V vs. RHE.

Chronoamperometry measurements for complex $\mathbf{2}$ at 2.0 V again show immediate O_2 evolution without any sign of an induction period or CO_2 formation preceding the evolution of O_2 (Fig. 2.5b). Measuring the mass trace of O_2 as a function of potential shows that the onset of O_2 evolution correlates with the sharp increase in oxidative current at 1.8 V (Fig. 2.6b). The current observed between 1.3 and 1.8 V correlates with CO_2 formation (Fig. 2.6b).

The reversible Fe^{II/III} couple of complex **3** was observed at 0.9 V in a 0.1 M NaClO₄ solution (Fig. 2.9a). From 1.5 V onwards, an irreversible oxidative current can be observed with a sharp increase at 1.9 V (Fig. 2.9b). In the OLEMS measurements of complex **3**, detectable amounts of CO_2 are observed beyond 1.6 V and the irreversible oxidative current starting at 1.9 V can be attributed to O_2 evolution (Fig. 2.6c).

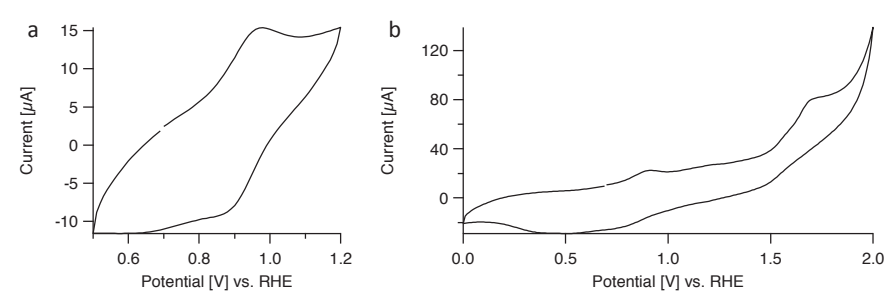


Figure 2.9: Results of a CV measurement of complex 1.1 mM $\bf 3$ using a PG working electrode in a 0.1 M NaClO₄ solution measured at 10 mV/s with a starting potential of 0.7 V vs. RHE with a scan range of (a) 0.0 to 1.0 V vs. RHE and (b) 0.0 to 2.0 V vs. RHE.

By comparing the relative amounts of O_2 and CO_2 that are observed in the OLEMS measurements, it appears that the catalytic activity of complex **3** is substantially lower than that of **1** and **2**. Considering the presence of some high-spin Fe^{III} species in aqueous solutions of **3** (Fig. A.1b, Appendix A), one might wonder whether the *trans*-complex is active at all or whether the observed catalytic activity for **3** is merely an artefact, due to small amounts of *cis*-complex present in solution.

2.2.2c Electrochemical studies in pH 7.5 phosphate buffer

For applications of a catalytic system at neutral pH, it is relevant to know whether the catalyst is active in the presence of a pH buffer. Both complexes **1** and **3** are fully deactivated in phosphate-containing media. Both complexes show a cathodic shift of the Fe^{II/III} redox couple to 0.3 V vs. RHE (Fig. 2.10a-b), indicating a strong interaction with phosphate.

OLEMS measurements of complex ${\bf 1}$ in a 0.1 M phosphate buffer solution show a similar CO_2 formation profile as seen previously in an unbuffered NaClO₄ solution but no signs of O_2 evolution up to 2.0 V (Fig. 2.11a). At low scan rates (1 mV/s) in the presence of phosphate, complex ${\bf 3}$ forms a deposit of an unidentified blue material on the surface of the PG electrode (Fig. A.4, Appendix A). The blue deposit itself is active for water oxidation (Fig. 2.11b), albeit with an onset for O_2 evolution at around 1.9 V. In the OLEMS experiment of complex ${\bf 3}$ in phosphate buffer, a steady increase in the dioxygen signal between each consecutive scan can be seen (Fig. 2.12) as a result of the slow formation of the deposit during high-potential conditions in each scan.

In the presence of 0.1 M phosphate (pH 7.5), complex **2** shows redox couples at 0.3 V and 0.6 V, indicating only partial inhibition by phosphate. (Fig. 2.10c). An

onset for O_2 evolution was observed at 1.9 V in an OLEMS measurement (Fig. 2.11c).

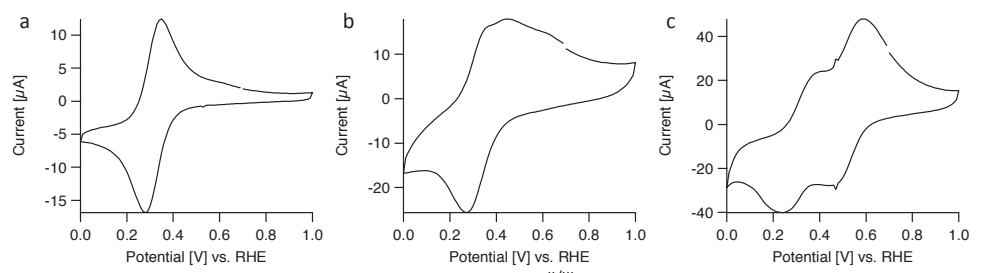


Figure 2.10: Results of CV experiments, showing the Fe^{II/III} redox couples of complex **1** (a), complex **3** (b) and complex **2** (c), each in a 0.1 M phosphate buffer solution (pH 7.5). All three CVs were recorded at 10 mV/s between 0.0 and 1.0 V vs. RHE with a starting potential of 0.7 V vs. RHE.

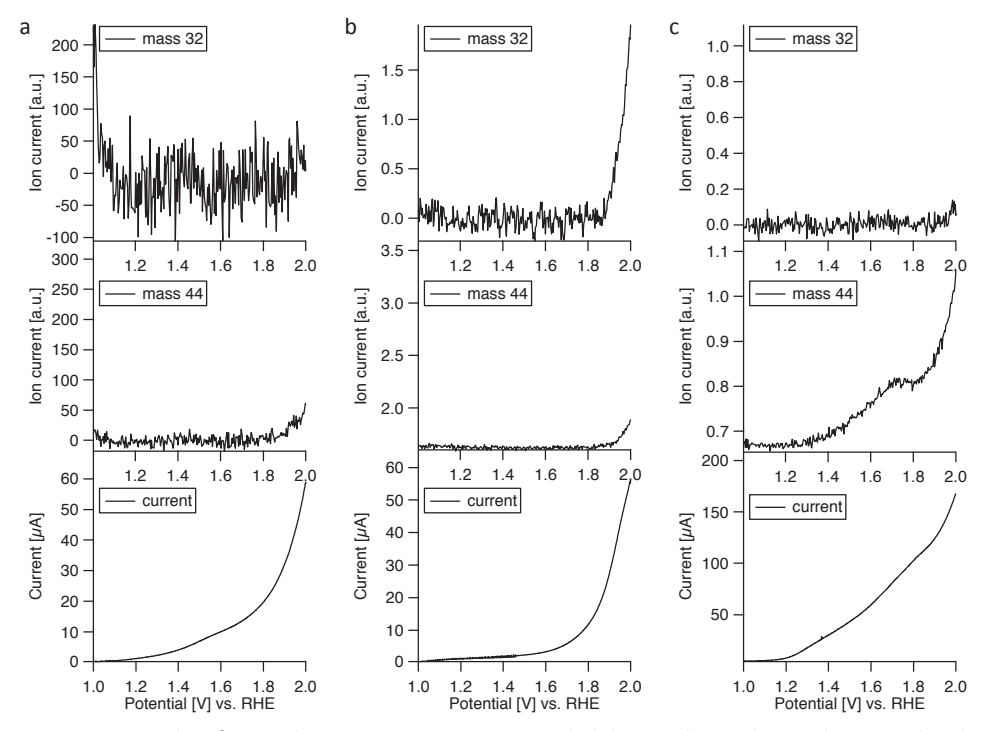


Figure 2.11: Results of several OLEMS experiments recorded during electrochemical potential cycling between 1.0 and 2.0 V vs. RHE at 1 mV/s, starting at 1.0 V vs. RHE. Shown are the m/z traces of O_2 (top) and CO_2 (middle) and the corresponding current (bottom) recorded. For the sake of clarity, only the forward scan of each experiment is depicted. The graphs correspond to: (a) 1.1 mM complex 1 in a 0.1 M phosphate buffer solution (pH 7.5), (b) the blue deposit which was formed while cycling the potential 3 times beween 1.0 and 2.0 V vs. RHE at 1 mV/s, starting at 1.0 V vs. RHE in the presence of 1.1 mM complex 3 in 0.1 M phosphate buffer solution (pH 7.5) and (c) 1.1 mM complex 3 in a 0.1 M phosphate buffer solution (pH 7.5)

In contrast to complex **3**, complexes **1** and **2** showed no visible signs of deposition of (blue) material onto the electrode surface even after prolonged potential cycling between 1.0 and 2.0 V at a scan rate of 1 mV/s. Electrodes which were taken out of a phosphate buffer solution containing complex **1** or **2**, rinsed with Milli-Q water and placed in a fresh phosphate buffer solution of identical concentration and pH did not produce any significant current above the PG background.

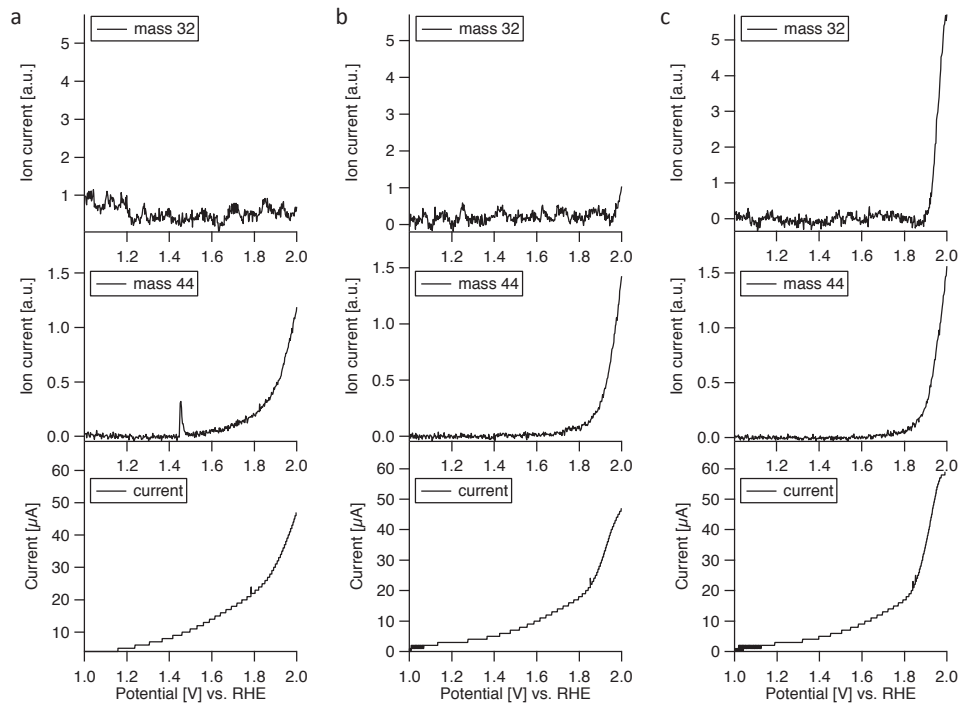


Figure 2.12: Three scans of an OLEMS experiment of 1.5 mM complex 3 in a 0.1 M phosphate buffer solution (pH 7.5). Shown are the m/z traces of O_2 (top), CO_2 (middle) and the corresponding current (bottom). For the sake of clarity, only the forward scan of each experiment is depicted. (a) Scan 1 of 3 between 1.0 and 2.0 V vs. RHE, recorded at 1 mV/s, starting at 1.0 V vs. RHE. (b) Scan 3 of 3 between 1.0 and 2.0 V vs. RHE, recorded at 1 mV/s, starting at 1.0 V vs. RHE. (c) Scan 3 of 3 between 1.0 and 2.0 V vs. RHE, recorded at 1 mV/s, starting at 1.0 V vs. RHE.

2.3 Conclusions

The use of on-line mass spectrometry techniques makes it possible to differentiate between catalytic current and current caused by side-reactions such as CO_2 formation. This offers valuable new insights for studying water oxidation

catalysts and can help to alleviate some of the ambiguity caused by the use of sacrificial chemical oxidants.

While *cis*-[Fe(cyclam)Cl₂]Cl (1) displays water oxidation activity which was expected based on the results previously reported for comparable molecular iron-based catalysts, [Fe(cyclamacetate)Cl] (2) is the first water oxidation catalyst of its kind to operate in aqueous media. In contrast to complexes 1 and 3, complex 2 was found to be more tolerant towards the presence of phosphate buffer.

In the three complexes investigated in this study, water oxidation activity was demonstrated to be enabled both by the motif of *cis* vacant sites as well as a fifth donor ligand in axial position. Both structural motifs seem to affect the electronic structure of the corresponding complexes in a similar way, leading to a cathodic shift of the Fe^{II/III} redox event compared to *trans*-[Fe(cyclam)Cl₂] (3) and enabling water oxidation at lower onset potentials. These results highlight the importance of the electronic features as a design principle for creating new iron-based electrocatalysts for the water oxidation reaction.

The observation of CO_2 formation during the measurements could be indicative of oxidative decomposition of the ligand structure under catalytic conditions, suggesting the need for a more oxidatively stable ligand framework. However, the presence of a carbon-based electrode material makes it difficult to determine the source of the CO_2 .

2.4 Experimental

2.4.1 General

All chemicals were used as received and without further purification. Cyclam was obtained from Alfa Aesar and iodoacetic acid was obtained from Acros Organics. FeCl₂·4H₂O was obtained from Sigma Aldrich and stored under argon. Cylcamacetate·4HCl and *cis*-[Fe(cyclam)Cl₂]Cl (1) were synthesized according to literature procedures. ^[11, 19] The syntheses of complexes 2 and 3 were performed using standard Schlenk-line techniques. Acetonitrile was degassed using standard freeze-pump-thaw protocols.

IR spectra were recorded on a Perkin Elmer UATR (Single Reflection Diamond) Spectrum Two device. Mass spectra were measured on a Finnigan Aqua Mass ESI spectrometer. NMR spectra were measured on a Bruker DPX 300 spectrometer. EPR spectra were recorded on a Bruker EMXplus X-band spectrometer. Elemental analyses were performed by Mikroanalytisches Laboratorium Kolbe in Germany.

2.4.2 Electrochemical experiments

Electrochemical measurements were performed in a custom made single-compartment glass cell on Ivium potentiostats, operated by IviumSoft software, using a three-electrode setup. The working electrode was a pyrolytic graphite (PG) disc with a (geometric) surface area of 0.2 cm² used in hanging meniscus configuration. A large surface area gold plate was used as a counter electrode. The reference electrode was a reversible hydrogen electrode (RHE) made up of a platinum mesh in H₂-saturated electrolyte at the same pH as the working solution. The cell and the reference electrode were connected via a Luggin capillary. A fresh PG surface was prepared before each experiment by polishing the working electrode with sandpaper and subsequent removal of excess debris by sonication in Milli-Q water for at least 5 minutes.

All glassware used in electrochemical measurements was routinely cleaned of any organic contamination by boiling in 3:1 mixture of concentrated sulfuric and nitric acid. Prior to each experiment the glassware was cleaned by threefold rinsing and boiling in Milli-Q water. The electrolyte solutions were prepared from p.a. grade chemicals obtained from Merck (Suprapur®) and Milli-Q water.

Prior to measurements, the electrolyte solution was purged of air by bubbling with argon (Linde, Ar 6.0) for at least 20 minutes. During the measurements, the cell was constantly kept under argon flow to prevent air from entering.

Except for preliminary tests with a gold working electrode (Fig. 2.2), all experiments were performed on a PG disc working electrode.

For the OLEMS measurements, the gasses formed at the working electrode were collected via a hydrophobic tip (KEL-F with a porous Teflon plug) in close proximity to the surface of the working electrode and analyzed in a QMS 200 mass spectrometer. A detailed description of the OLEMS setup is available elsewhere. [20] All electrochemical potential cycling in combination with OLEMS was done at a scan rate of 1 mV/s. For the mass spectrometry data recorded via OLEMS during cylic voltammetry measurements, background correction was done by assuming an exponential decay fit (concerns Figures 2.6, 2.11 and 2.12).

2.4.3 Synthesis of [Fe(cyclamacetate)Cl] (2)

Cyclamacetate·4HCl (112 mg, 0.28 mmol) was suspended in 5 mL acetonitrile and dissolved upon addition of triethylamine (0.2 mL, 1.42 mmol). Subsequently $FeCl_2\cdot4H_2O$ (60 mg, 0.30 mmol) dissolved in 5 mL acetonitrile was added. The mixture was left to stir over night. The white precipitate was subsequently filtered

off, washed with acetonitrile (3 x 5 mL) and dried in vacuo to give **2** as a white solid. Yield: 67 mg (0.19 mmol, 69%)

ESI-MS (1:1 MeOH: H_2O) calcd. for $C_{12}H_{25}CIFeN_4O_2$ [M]⁺ 348.1; Found: [M-Cl]⁺ 313.1, [M-Cl+OH]⁺ 330.1, [M-Cl+OMe]⁺ 344.2

IR (neat): 1595 cm^{-1} (s, C=O stretch).

Elemental analysis calcd. (%) for $C_{12}H_{25}CIFeN_4O_2$ (348.65 g/mol): C 41.34, H 7.23, N 16.07 Found: C 41.16, H 7.47, N 15.87.

2.4.4 Synthesis of trans-[Fe(cyclam)Cl₂] (3)

To a suspension of cyclam (40 mg, 0.20 mmol) in 5 mL acetonitrile, FeCl₂·4H₂O (40 mg, 0.20 mmol) dissolved in 5 mL acetonitrile was added. The mixture was left to stir over night. The pale pink precipitate was subsequently filtered off, washed with acetonitrile (3 x 5 mL) and dried in vacuo to give **3** as a pale pink solid. Yield: 42 mg (0.13 mmol, 64%)

ESI-MS (MeOH) calcd. for $C_{10}H_{24}Cl_2FeN_4$ [M]⁺ 326.1; Found: [M-H-Cl]⁺ 290.1, [M]⁺ 326.0

Elemental analysis calcd. (%) for $C_{10}H_{24}Cl_2FeN_4$ (327.07 g/mol): C 36.72, H 7.40, N 17.13 Found: C 38.31, H 8.08, N 16.48.

2.4.5 Elemental analysis of cis-[Fe(cyclam)Cl₂]Cl (1)

Elemental analysis calcd. (%) for $C_{10}H_{24}Cl_3FeN_4$ (362.52 g/mol): C 33.13, H 6.67, N 15.45 Found: C 33.33, H 6.50, N 15.38.

2.4.6 Sample preparation

For electrochemical experiments with the *in situ* oxidized complexes **2** and **3**, the respective Fe^{II}-complex was dissolved in air-saturated electrolyte and measured within minutes. In case of EPR experiments, the solution was kept under air for the entire duration. For EPR measurements, glycerol was added to the aqueous solution prior to freezing at 77 K in order to obtain a good glass. In electrochemistry experiments with samples of oxidized complexes **2** and **3**, the electrolyte solution was purged again by bubbling with argon for several minutes after the oxidized complex was added to the cell.

Complete dissolution of crystalline complex **1** was achieved by sonication for at least 20 minutes. Since the dissolution of **1** in 0.1 M NaClO₄ solution appears to be substantially slower compared to 0.1 M phosphate buffer, for the experiments in NaClO₄ media the complex was dissolved in Milli-Q water instead and

subsequently added to the electrolyte solution. In these experiments, the concentration of electrolyte in the cell was adjusted to account for the resulting dilution. After addition of complex **1**, the electrolyte was purged again by bubbling with argon for several minutes.

In electrochemical experiments described in this chapter, catalyst concentrations of 1.1 mM were used unless otherwise specified.

2.5 Supporting Info

The following supplementary information can be found in Appendix A: Results of EPR measurements of complexes **2** and **3** in frozen aqueous sample at 77 K (Fig. A.1), a comparison of the IR spectra of the free cyclamacetate·4HCl ligand and complex **2** (Fig. A.2), UV-vis spectra of complexes **1** and **3** in aqueous solution (Fig. A.3) and a picture of the blue deposit formed from complex **3** in pH 7.5 phosphate buffer on the surface of a PG electrode (Fig. A.4).

2.6 References

- [1] J. D. Blakemore; R. H. Crabtree; G. W. Brudvig, *Chem. Rev.* **2015**, *115*, 12974-13005.
- [2] D. G. H. Hetterscheid; J. N. Reek, Angew. Chem., Int. Ed. 2012, 51, 9740-9747.
- [3] X. Sala; I. Romero; M. Rodriguez; L. Escriche; A. Llobet, *Angew. Chem., Int. Ed.* **2009**, *48*, 2842-2852.
- [4] D. J. Wasylenko; R. D. Palmer; C. P. Berlinguette, *Chem. Commun.* **2013**, *49*, 218-227.
- [5] M. D. Karkas; B. Akermark, Dalton Trans. 2016, 45, 14421-14461.
- [6] A. Singh; L. Spiccia, Coord. Chem. Rev. 2013, 257, 2607-2622.
- [7] J. L. Fillol; Z. Codola; I. Garcia-Bosch; L. Gomez; J. J. Pla; M. Costas, *Nat. Chem.* **2011**, *3*, 807-813.
- [8] W. C. Ellis; N. D. McDaniel; S. Bernhard; T. J. Collins, *J. Am. Chem. Soc.* **2010**, *132*, 10990-10991.
- [9] F. Acuna-Pares; Z. Codola; M. Costas; J. M. Luis; J. Lloret-Fillol, *Chem. Eur. J.* **2014**, *20*, 5696-5707.
- [10] Z. Codola; L. Gomez; S. T. Kleespies; L. Que, Jr.; M. Costas; J. Lloret-Fillol, *Nat. Commun.* **2015**, *6*, 5865.
- [11] R. Guilard; O. Siri; A. Tabard; G. Broeker; P. Richard; D. J. Nurco; K. M. Smith, *J. Chem. Soc., Dalton Trans.* **1997**, 3459-3463.
- [12] M. Costas; M. P. Mehn; M. P. Jensen; L. Que, Jr., *Chem. Rev.* **2004**, *104*, 939-986.
- [13] B. Zhang; F. Li; F. Yu; H. Cui; X. Zhou; H. Li; Y. Wang; L. Sun, *Chem. Asian J.* **2014**, *9*, 1515-1518.

- [14] G. Mathies; S. D. Chatziefthimiou; D. Maganas; Y. Sanakis; S. Sottini; P. Kyritsis; E. J. Groenen, *J. Magn. Reson.* **2012**, *224*, 94-100.
- [15] W. S. Szulbinski; D. H. Busch, Inorg. Chim. Acta 1995, 234, 143-148.
- [16] G. Chen; L. Chen; S. M. Ng; W. L. Man; T. C. Lau, *Angew. Chem., Int. Ed.* **2013**, *52*, 1789-1791.
- [17] Z. Chen; J. J. Concepcion; N. Song; T. J. Meyer, *Chem. Commun.* **2014**, *50*, 8053-8056.
- [18] Z.-Q. Wang; Z.-C. Wang; S. Zhan; J.-S. Ye, Appl. Catal., A 2015, 490, 128-132.
- [19] M. Studer; T. A. Kaden, Helv. Chim. Acta 1986, 69, 2081-2086.
- [20] A. H. Wonders; T. H. M. Housmans; V. Rosca; M. T. M. Koper, *J. Appl. Electrochem.* **2006**, *36*, 1215-1221.

Enhancement of the catalytic activity of a homogeneous iron-based water oxidation catalyst through substrate effects of graphitic electrodes

The synthesis, characterization and electrochemical studies of the dinuclear complex [(MeOH)Fe(Hbbpya)- μ -O-(Hbbpya)Fe(MeOH)](OTf)₄ (1) (with Hbbpya = N,N-bis(2,2'-bipyrid-6-yl)amine) are described. With the help of on-line electrochemical mass spectrometry, the complex is demonstrated to be active as a water oxidation catalyst. The complex shows a significantly lower catalytic overpotential on graphitic working electrodes compared to other electrode materials which is ascribed to specific interactions between the Hbbpya ligand in the complex and the surface of an sp^2 carbon electrode. Cyclic voltammetry experiments provide evidence that the structure of complex 1 undergoes reversible changes under high potential conditions, regenerating the original structure of complex 1 upon returning to lower potentials. Results from electrochemical quartz crystal microbalance experiments rule out that catalysis proceeds via deposition of catalytically active material on the electrode surface.

3.1 Introduction

An important aspect in homogeneous electrocatalysis which has so far received only little attention is the influence of the electrode surface on the reaction mechanisms involving homogeneous electrocatalysts. If the electron transfer between the catalyst and the electrode proceeds exclusively via an outer sphere mechanism, one would expect only a small influence of the electrode material. However, in case of an inner sphere mechanism involving adsorption of the catalyst on the electrode surface, a much larger influence of the electrode material is to be expected. Despite the potentially very important role of the electrode material in electrochemical water oxidation catalysis only few examples of research on this subject can be found in literature.

In this chapter we introduce the dinuclear oxo-bridged iron complex $[(MeOH)Fe(Hbbpya)-\mu-O-(Hbbpya)Fe(MeOH)](OTf)_4$ (1) (with Hbbpya = N,N-bis(2,2'-bipyrid-6-yl)amine). This complex was designed based on the results described in chapter 2. The Hbbpya ligand is free of β -hydrogen atoms which can lead to degradation of the ligand under strongly oxidizing conditions^[4] and the aromatic structure of the Hbbpya ligand should provide additional stability towards oxidation compared to the aliphatic cyclam ligand. Furthermore, the Hbbpya ligand is expected to be more electron donating due to its more electron rich structure compared to cyclam. Finally, the amino group which bridges the two bipyridine moieties could provide a useful platform for additional ligand modifications in the future although such modifications have previously been reported to affect the structure of the resulting complex. [5]

To ensure that complex **1** can be studied with a variety of different electrode materials, halide ions are avoided to achieve compatibility of the complex with gold working electrodes.

The complex is active as an electrocatalyst for water oxidation, which is in line with previous reports that have found dinuclear oxygen-bridged iron complexes to be active water oxidation catalysts.^[5-9] However, in case of complex **1** the results show that the water oxidation activity is strongly dependent on the nature of the electrode material, resulting in a significantly lower overpotential on graphitic working electrodes compared to other electrode materials.

3.2 Results and Discussion

3.2.1 Synthesis and Characterization

Complex 1 was synthesized by combining methanolic solutions of iron(II) triflate and Hbbpya under argon (Scheme 3.1). After stirring over night and subsequent evaporation of the solvent, a crude reddish/brownish solid was obtained. To isolate complex 1, the crude product was recrystallized in air by vapor diffusion of Et_2O into a concentrated methanolic solution of the crude material, resulting in dark brown crystals of complex 1. The crystalline material was characterized by single crystal X-ray crystallography, mass spectrometry and elemental analysis. X-ray structure determination unequivocally reveals the dimeric nature of complex 1 (Fig. 3.1). All relevant bond angles and distances of the crystal structure of 1 are summarized in table B.2 (Appendix B).

Scheme 3.1: Synthesis of complex 1

The complex consists of two iron sites bridged by an oxo-ligand. Each iron site bears an Hbbpya ligand following a distorted square planar geometry and an axial methanol ligand. The measured bond angles and bond distances are very similar for both iron sites. All eight Fe–N bond distances fall into a narrow range of 2.11 to 2.14 Å. Both N–Fe–N bond angles of the six-membered chelate rings of 87.0° and 87.1° respectively are close to the ideal 90° of a square planar geometry. The N–Fe–N angles of the five-membered chelate rings are more acute at 78.2° to 78.7° while the open N–Fe–N bond angles are much wider at 114.2° and 114.6°. Both internal Fe–O bond distances between the iron centres and the bridging oxoligand of 1.78 Å are shorter than the external Fe–O bonds distances to the methanol ligands of 2.15 Å. These values are in good agreement with values

previously reported by Thummel et al. for the iron complexes $[(H_2O)Fe(ppq)-\mu-O-(ppq)FeCl]Cl_3$ (2) (with ppq = 2-(pyrid-2'-yl)-8-(1",10"-phenanthrolin-2"-yl)-quinoline) and $[Fe(dpa)Cl_2]Cl$ (3) (with dpa = N,N-di(1,10-phenanthrolin-2-yl)-N-isopentylamine). [5]

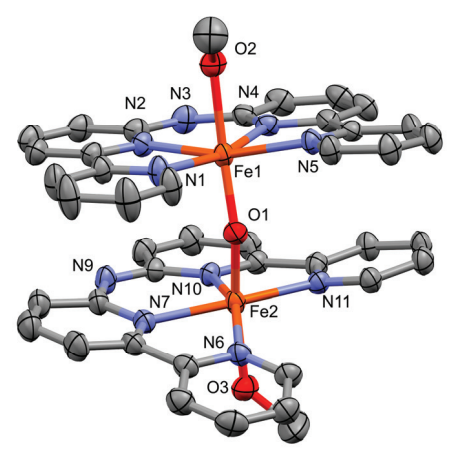


Figure 3.1: Displacement ellipsoid plot (50% probability level) of complex **1** at 110 K. All hydrogen atoms and the four triflate counter-ions have been omitted for clarity.

While the Fe-O-Fe bond angle in the structure of complex 2 was reported to be 171.3°, the Fe–O–Fe bond angle of 155.78° in complex 1 deviates notably from the expected 180°. The atoms of the two Hbbpya ligands are also not aligned directly on top of each other in the crystal structure. Instead each atom of the Hbbpya ligand bound to Fe1 is offset with respect to its counterpart in the Hbbpya ligand bound to Fe2 by a rotation around the Fe1-Fe2 axis of about 44° (Fig. B.1, Appendix B). Furthermore, the two Hbbpya ligands differ in their conformation. While one Hbbpya ligand is fairly planar with an internal torsion angle of only 3.0° (Fig. B.2, Appendix B), one of the two bipyridine moieties of the other Hbbpya ligand is twisted out of plane, resulting in a considerably greater internal torsion angle of 16.4° (Fig. B.2, Appendix B). As a result, the distances between the two Hbbpya ligands vary from a relatively narrow range of 3.37 Å to 3.55 Å for the two bipyridine moieties in face parallel alignment to a much wider spread of 3.52 Å to 4.40 Å for the other two bipyridine moieties (Fig. B.3, Appendix B). These features suggest that the distortions in the structure are compensated for by favourable π - π interactions between the aromatic systems of the two Hbbpya ligands. The observed distances of 3.37 Å to 3.55 Å fall well within the range commonly found for such interactions.[10]

Next to the structural data for the crystalline material, mass spectrometry data confirms that the complex exists exclusively as a dimeric species in aqueous solution (Fig. B.4, Appendix B). UV-vis measurements of the aqueous solution show no change in the absorption spectrum for at least 10 hours, confirming that the dimeric species is stable over time (Fig. B.5, Appendix B)

3.2.2 Electrochemical experiments

3.2.2a General considerations

Although complex ${\bf 1}$ dissolves in water, it hardly dissolves in solutions containing perchlorate anions. As a consequence, sodium sulfate was chosen as the most appropriate electrolyte even though the sulfate ion has been shown to inhibit water oxidation activity slightly compared to perchlorate in some cases. ^[11] In 0.1 M Na₂SO₄ complex ${\bf 1}$ does dissolve up to concentrations of 0.5 mM.

3.2.2b Electrochemistry on gold

Using a gold working electrode, the redox behavior of complex 1 was investigated by performing cyclic voltammetry (CV) experiments across different scan ranges. Figures 3.2a and 3.2b show the respective first and second scan of a CV experiment between 0.0 and 1.2 V vs. a reversible hydrogen electrode (RHE), starting each scan at 0.7 V vs. RHE. In the second scan (Fig. 3.2b), four distinct redox events can be observed, indicated as I, II, III and IV in the figure. I and IV are tentatively assigned to the [Fe"Fe"]/[Fe"Fe"] transition and II and III to the [Fe"Fe"]/[Fe"Fe"] transition. This assignment is supported by the fact that the oxidation event II at 0.9 V is largely absent in the first forward scan (Fig. 3.2a) as long as a starting potential above both reduction events III and IV is chosen. Since the complex is introduced in the [Fe^{III}Fe^{III}] state and the selected resting potential of 0.7 V lies above both reduction events, hardly any [Fe^{II}Fe^{III}] is present to be oxidized in the first scan. Further evidence for this assignment is obtained when the starting potential is set to 0.2 V and the scan range is selected to stay below the onset of second oxidation event between 0.8 and 1.0 V. The corresponding voltammogram between 0.2 and 0.8 V (Fig. 3.2c) only shows transitions I and IV, showing that reduction wave IV is connected to oxidation wave I, and that reduction wave III is connected to oxidation wave II.

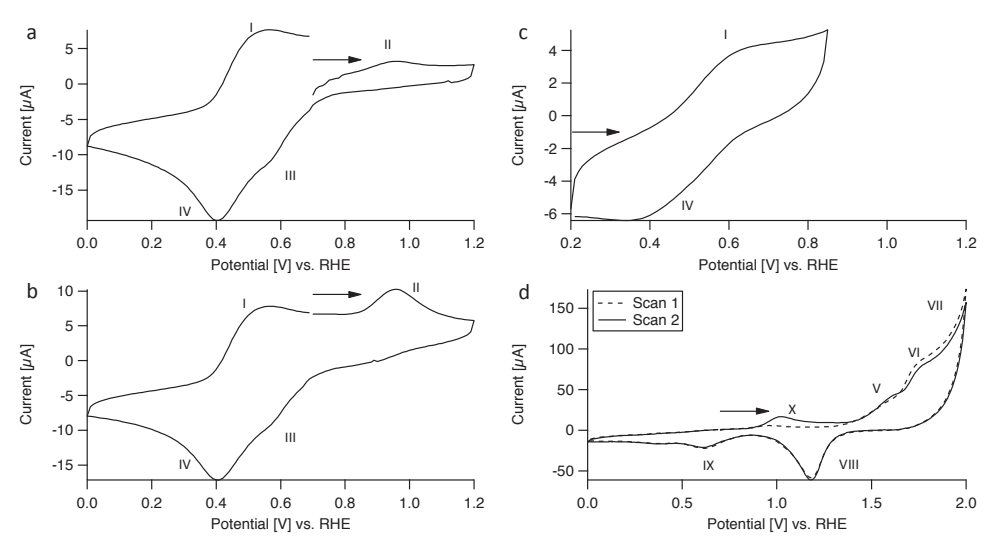


Figure 3.2: Results of CV experiments of 0.5 mM complex **1** in a 0.1 M Na_2SO_4 solution using a gold working electrode scanning at 100 mV/s. Arrows indicate the direction of each cycle. (a) First scan between 0.0 and 1.2 V vs. RHE, starting at 0.7 V vs. RHE. (b) Second scan between 0.0 and 1.2 V vs. RHE, starting at 0.7 V vs. RHE, starting at 0.8 V vs. RHE, starting at 0.2 V vs. RHE. (d) First and second scan between 0.0 and 2.0 V vs. RHE, starting at 0.7 V vs. RHE.

When the scan range is set to 0.0-2.0 V, a shift in the redox behavior is observed. Starting again at 0.7 V, the first forward does not show any new oxidation events below 1.5 V (Fig. 3.2d). Above 1.5 V three oxidation events are observed, labeled V, VI and VII, which can be attributed to gold oxide formation (V and VI) and water oxidation (VII) respectively (vide infra).

In the backward scan, two reduction events can be seen, one at 1.2 V (VIII; gold oxide reduction) and one at 0.6 V (IX). In the second forward scan, one additional oxidation event (X) appears at 1.0 V. Instead of the four transitions I, II, III and IV that were initially observed for the Fe^{II}/Fe^{III} redox events when scanning between 0.0 and 1.2 V, only the two new and broad redox events IX and X can be observed below 1.2 V in subsequent cycles after reaching 2.0 V. This difference indicates that complex 1 undergoes structural changes at high potentials. Scanning from 0.0 to 2.0 V and recording 50 scans between 0.0 and 1.2 V at 100 mV/s immediately afterwards shows that this change in redox behavior reverts over time; waves IX and X disappear while the waves I-IV reappear during prolonged scanning, showing that the change to the structure of complex 1 is reversible (Fig. 3.3).

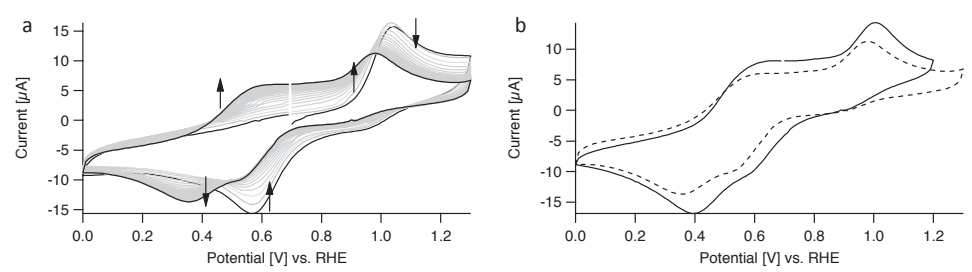


Figure 3.3: Demonstration of the evolution over time of the redox events observed after initially scanning to 2.0 V vs. RHE with a gold working electrode in the presence of 0.5 mM complex 1. The change in time is visualized with CV experiments between 0.0 and 1.3 V vs. RHE at a scan rate of 100 mV/s. All experiments were performed in a 0.1 M Na_2SO_4 solution. (a) 50 cycles between 0.0 and 1.3 V vs. RHE, starting at 0.7 V vs. RHE, recorded immediately after scanning to 2.0 V vs. RHE. The first and the last scan are displayed in black while the intermediate scans are displayed in grey. Arrows indicate the change in the current profile over time. (b) Comparison between the redox events before scanning to 2.0 V vs. RHE (solid line) and scan number 50 after scanning to 2.0 V vs. RHE (dashed line).

Evidence that the irreversible oxidation wave VII belongs to the oxygen evolution reaction was obtained via OLEMS experiments. In OLEMS experiments the m/ztraces of selected gaseous species sampled in solution in close proximity to the surface of the working electrode are recorded during electrochemical experiments. [12] Figure 3.4 shows the second forward scan of an OLEMS experiment, recorded while cycling the potential between 1.3 and 2.0 V at 1 mV/s, with a starting potential of 1.3 V. The bottom panel of figure 3.4 shows the corresponding current trace. Since the gold electrode was already oxidized during the first scan of the OLEMS experiment, the gold oxidation waves V and VI are absent in the second scan, leaving only the oxidation wave VII. The top panel of figure 3.4 shows the mass trace for O₂ recorded during the experiment which shows a clear onset of oxygen evolution at about 1.9 V that correlates well with the oxidative current shown in the bottom panel of figure 3.4. Since previous reports^[13-15] have shown that electrocatalytic water oxidation by metal complexes is often preceded or accompanied by oxidative degradation of ligands, which can result in the formation of CO₂, we also recorded the mass trace of CO₂ via OLEMS (Fig. 3.4, middle). The result shows that, compared to oxygen, no significant amounts of CO₂ are being formed during the experiment.

The gold electrode in itself is in principle capable of oxidizing water at high potentials, however, in previous work no detectable amounts of oxygen were found below 2.0 V for a gold working electrode in the absence of any additional catalyst. [16] While there is still some oxidative current beyond gold oxidation that is visible in blank measurements, OLEMS measurements with a gold working

electrode in a $0.1 \text{ M Na}_2\text{SO}_4$ electrolyte solution in the absence of complex **1** confirm that there is no detectable amount of oxygen being formed below 2.0 V under those conditions (Fig. B.6, Appendix B).

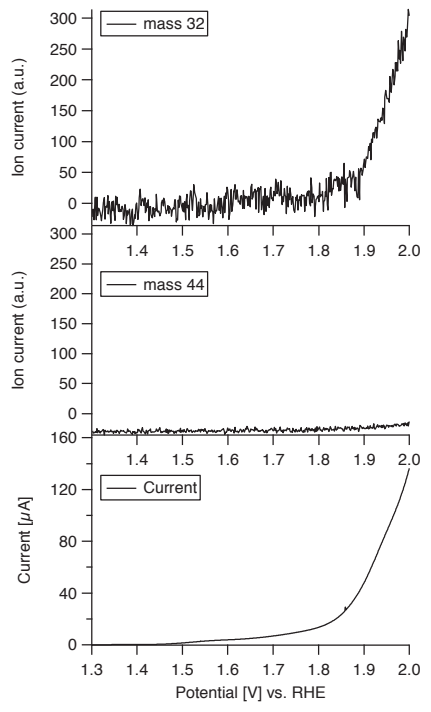


Figure 3.4: Results of an OLEMS measurement of 0.5 mM complex 1 with a gold working electrode in a 0.1 M Na_2SO_4 solution (scan range, 1.3-2.0V vs. RHE, scan rate 1 mV/s, starting at 1.3 V vs. RHE). Shown is the forward scan of a CV experiment with the m/z trace for O_2 (top), the m/z trace for CO_2 (middle) and the corresponding current (bottom).

3.2.2c Electrochemistry on carbon

The electrochemistry that is observed for complex 1 with a pyrolytic graphite (PG) working electrode shows a significant difference from the results obtained for a gold working electrode. For both electrodes, complex 1 initially shows redox waves I-IV (Fig. 3.5a) which disappear when the potential is increased to 2.0 V, resulting in the formation of a new species, giving rise to redox waves IX and X (Fig. 3.5b). Likewise, for both electrode materials the disappearance of waves IX and X accompanied by the reappearance of waves I-IV can be seen over time when the potential is kept below 1.2 V after initially scanning to 2.0 V (Fig. 3.5c-d). However, in contrast to the electrochemistry on gold, an additional and persistent irreversible oxidation wave can be observed on PG with an onset potential of about 1.6 V (Fig. 3.6, bottom).

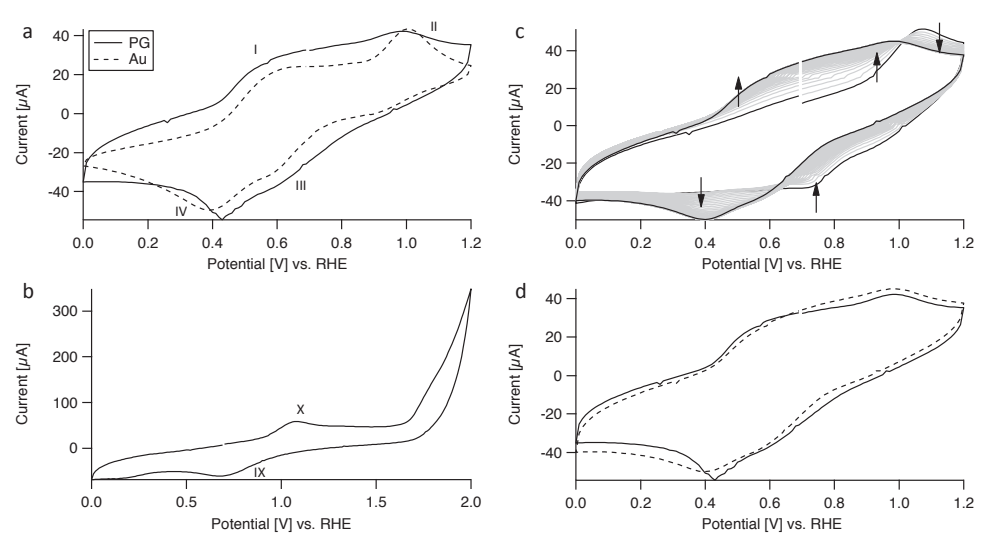


Figure 3.5: Shown are several voltammograms of 0.5 mM complex **1** in a 0.1 M Na_2SO_4 , recorded at 100 mV/s, each with a starting potential of 0.7 V vs. RHE. (a) Results of scanning between 0.0 and 1.2 V vs. RHE on a PG working electrode and a gold working electrode. The current recorded for the gold working electrode was normalized by a factor of 3 for the sake of comparison. Shown is the second scan of each experiment. (b) Results of scanning between 0.0 and 2.0 V vs. RHE on a PG working electrode. (c) 50 cycles between 0.0 and 1.3 V vs. RHE, recorded on a PG working electrode immediately after scanning to 2.0 V vs. RHE. The first and the last scan are displayed in black while the intermediate scans are displayed in grey. Arrows indicate the change in the current profile over time. (d) Comparison between the redox events recorded on a PG working electrode before scanning to 2.0 V vs. RHE (solid line) and scan number 50 after scanning to 2.0 V vs. RHE (dashed line).

While the separation between the two waves above 1.6 V is not very well resolved at higher scan rates (100 mV/s, Fig. 3.5b), it becomes much more pronounced at lower scan rates (10 mV/s and slower, Fig. 3.6, bottom and Fig. 3.7b).

OLEMS measurements for complex 1 with PG were performed under the same conditions as the respective experiments with gold, recording the mass traces for O_2 and CO_2 while cycling the potential between 1.3 and 2.0 V at 1 mV/s with a starting potential of 1.3 V. The recorded current (Fig. 3.6, bottom) shows two oxidation events in the forward scan from around 1.6 V onward. The corresponding O_2 trace (Fig. 3.6, top) shows that oxygen evolution follows the recorded current profile which suggests that both oxidation waves correspond to an oxygen evolution reaction. It appears that the formation of dioxygen is feasible for complex 1 in combination with a PG working electrode starting around 1.6 V whereas with a gold working electrode this is not the case until about 1.9 V. (compare Fig. 3.6, top and bottom with Fig. 3.4, top and bottom).

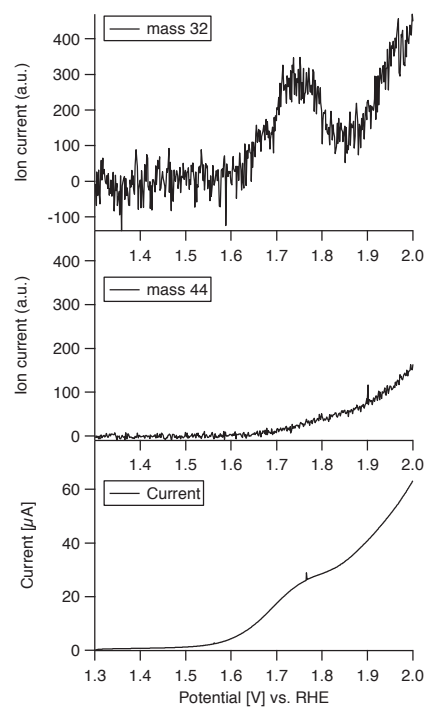


Figure 3.6: Results of an OLEMS measurement for 0.5 mM complex **1** on a PG working electrode in a 0.1 M Na_2SO_4 solution (scan range, 1.3-2.0V vs. RHE, scan rate 1 mV/s, starting at 1.3 V vs. RHE). Shown is the forward scan of a CV experiment with the m/z trace for O_2 (top), m/z trace for CO_2 (middle) and the corresponding current (bottom).

Aside from oxygen evolution, significant amounts of CO_2 are produced simultaneously at oxidative potentials when a PG working electrode is used (Fig. 3.6, middle). While it is difficult to unambiguously assign either the complex or the electrode material as the source of the CO_2 , the results obtained when using a gold working electrode suggest that most of the CO_2 does indeed originate from the oxidation of pyrolytic graphite. This hypothesis is supported by the observation that for a solution containing $Fe(OTf)_2$ instead of complex $\mathbf{1}$, CO_2 formation of the same order of magnitude with roughly the same onset potential is observed (vide infra).

In contrast to gold, a PG working electrode does not produce any detectable amounts of oxygen in the absence of an additional catalyst even at potentials significantly greater than 2.0 V (cf. chapter 5, Fig. 5.2). This shows clearly that the presence of complex 1 is crucial for the formation of dioxygen observed during the experiment.

The apparent difference in reactivity of complex 1 between experiments with a gold working electrode and a PG working electrode prompted us to look further

into the correlation between the properties of the electrode surface and the resulting electrochemistry. Using a glassy carbon (GC) working electrode in combination with complex 1 yields results that are qualitatively identical to those obtained on PG, both with respect to the redox behavior (Fig. 3.7a-b) and the two oxidation waves above 1.6 V (Fig. 3.7b). Voltammograms recorded with a boron doped diamond (BDD) working electrode instead only show a single oxidation event above 1.6 V (Fig. B.7, Appendix B), similar to the results for a gold working electrode, instead of the two distinct waves observed for graphitic electrode materials. The comparison between the results obtained for the four different electrode materials points to different modes of activity for complex 1 on graphitic working electrodes compared to non-graphitic working electrodes.

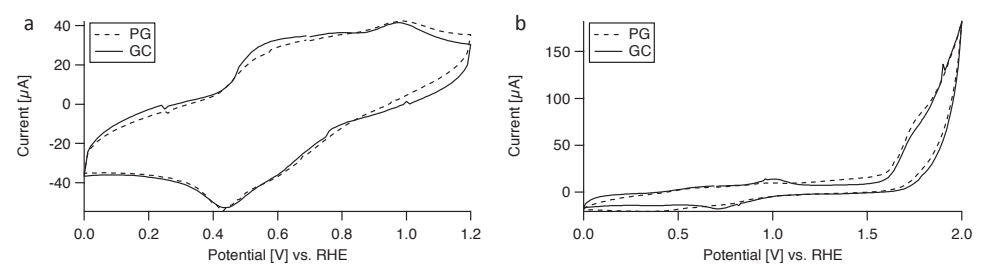


Figure 3.7: Shown are voltammograms of 0.5 mM complex 1 in a 0.1 M Na₂SO₄ solution recorded on different working electrodes. (a) Comparison of the results using a PG and a GC working electrode. Shown is the respective second scan of each experiment, recorded between 0.0 and 1.2 V vs. RHE at 100 mV/s with a starting potential of 0.7 V vs. RHE. The current recorded on GC was normalized by a factor of 4.5 for the sake of comparison. (b) Comparison of the results using a PG and a GC working electrode. Shown is the respective second scan of each experiment, recorded between 0.0 and 2.0 V vs. RHE at 10 mV/s with a starting potential of 0.7 V vs. RHE. The current recorded on GC was normalized by a factor of 4.5 for the sake of comparison.

3.2.3 Homogeneous catalyst vs. heterogeneous surface deposit

Since Fe₂O₃ is known to be a catalyst for water oxidation, [17-20] it is important to establish that no such deposits are being formed on the working electrode, which then may be responsible for (part of) the observed reactivity. To rule out the formation of catalytically active surface deposits, electrochemical quartz crystal microbalance (EQCM) experiments were carried out with a gold working electrode. [21-22] The working electrode in EQCM experiments consists of a thin layer of gold, deposited on a quartz crystal oscillator. Mass changes at the working electrode can be detected by measuring changes in the resonance frequency of the quartz crystal. To avoid damaging the thin gold layer of the EQCM electrode and due to the mass change associated with gold oxide formation and reduction,

the potential was kept above 1.3 V at all times during EQCM experiments to avoid gold oxide reduction. The results show no significant change in the mass of the electrode for the potential window between 1.3 and 2.0 V at 1 mV/s in the presence of complex 1 (Fig. 3.8a).

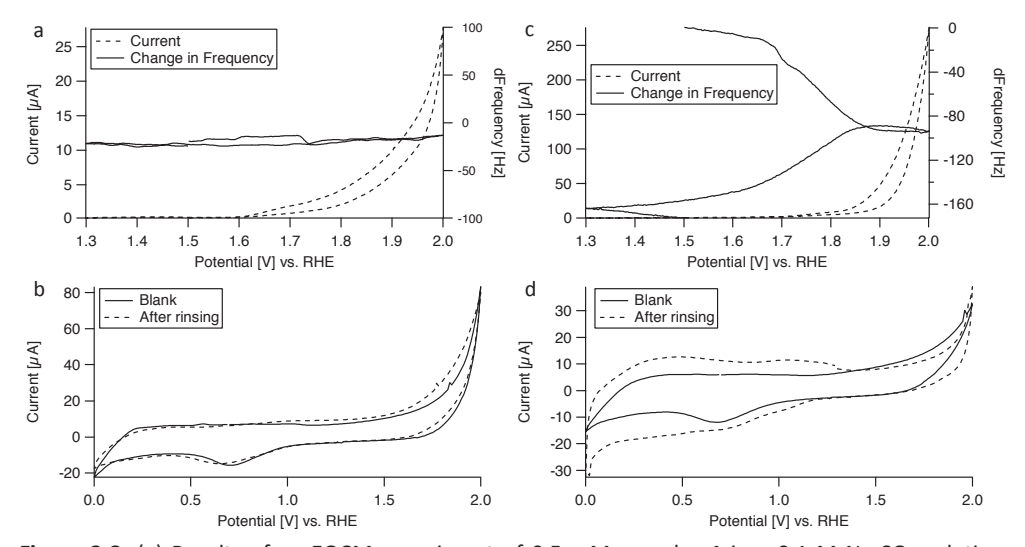


Figure 3.8: (a) Results of an EQCM experiment of $0.5\,$ mM complex 1 in a $0.1\,$ M Na_2SO_4 solution, recorded between 1.3 and $2.0\,$ V vs. RHE with a gold working electrode at 1 mV/s, starting at $1.5\,$ V vs. RHE. (b) Voltammograms of a freshly polished PG working electrode in a blank solution of $0.1\,$ M Na_2SO_4 and the same PG working electrode in a blank $0.1\,$ M Na_2SO_4 solution after cycling 3 times between 1.3 and $2.0\,$ V vs. RHE at 1 mV/s in the presence of $0.5\,$ mM complex 1 in a $0.1\,$ M Na_2SO_4 solution and subsequent rinsing in the electrode. Both voltammograms were recorded between $0.0\,$ and $0.0\,$ V vs. RHE at $0.0\,$ mV/s, starting at $0.7\,$ V vs. RHE. (c) Result of an EQCM experiment of $0.0\,$ mM $0.0\,$ mM $0.0\,$ m $0.0\,$ m 0.0

Since no graphitic EQCM electrodes were available, a PG working electrode was instead cycled 3 times between 1.3 and 2.0 V at a scan rate of 1 mV/s in the presence of complex $\bf 1$, taken out of the electrolyte solution and rinsed. A subsequently recorded voltammogram measured in a 0.1 M Na₂SO₄ electrolyte solution in the absence of complex $\bf 1$ showed no additional current above the background of a blank measurement (Fig. 3.8b). These results show that if any electrode deposition does occur during catalytic water oxidation mediated by complex $\bf 1$ it must be a highly reversible process.

In contrast to the results obtained for complex **1**, EQCM experiments in the presence of 1 mM $Fe(OTf)_2$ show a clear change in the mass of the gold electrode under identical conditions, indicating the formation of a deposit on the electrode surface (Fig. 3.8c). Similarly, cycling a PG working electrode 3 times between 1.3 and 2.0 V at 1 mV/s in the presence of $Fe(OTf)_2$ with subsequent rinsing of the electrode and recording a CV measurement between 0.0 and 2.0 V in a 0.1 M Na_2SO_4 electrolyte solution without $Fe(OTf)_2$ present yields a voltammogram which is different from that of a blank measurement (Fig. 3.8d). OLEMS measurements of $Fe(OTf)_2$ on a PG working electrode reveal water oxidation activity, albeit with a different current profile and higher onset potential for the oxygen evolution reaction compared to complex **1** (Fig. B.8, Appendix B).

The ion current for CO_2 measured with a PG working electrode in the presence of complex $\mathbf{1}$ and $Fe(OTf)_2$ respectively is of the same order of magnitude (compare Fig. 3.6, middle with Fig. B.8, middle, Appendix B) despite $Fe(OTf)_2$ lacking any ligand that could conceivably be oxidized to CO_2 under these conditions, providing further evidence for the assumption that the CO_2 formation observed in OLEMS experiments with complex $\mathbf{1}$ on a PG working electrode originates predominantly from the oxidation of the electrode material rather than oxidation of the ligand.

3.2.4 Mechanistic considerations

For PG, GC and Au working electrodes, we found that the redox behavior of complex 1 in solution changes upon exposure to high potentials. When kept at lower potentials afterwards, it slowly reverts to the original behavior (Fig. 3.3 and Fig 3.5c-d). Since mass spectrometry and UV-vis spectroscopy show that complex 1 exists exclusively as a dimer at the start of the experiment, this reversibility means that the dimeric structure is regenerated at lower potentials. A possible explanation could be that the complex falls apart into two Fe(Hbbpya) monomers upon oxidation to the Fe^{IV} or Fe^V state which re-associate to form complex 1 in the Fe^{III} state.

Evidence for the molecular nature of the catalytically active species was obtained from EQCM experiments on gold in which no mass changes of the electrode were observed in the presence of complex $\mathbf{1}$ under catalytic conditions. From control experiments with $Fe(OTf)_2$ instead of complex $\mathbf{1}$ we can rule out any potential pathways involving de-coordination of the Hbbpya ligand leading to the subsequent formation of the active catalyst in the form of solid deposits on the electrode surface.

For the combination of complex ${\bf 1}$ with graphitic working electrodes, oxygen evolution was observed already at significantly lower potentials compared to complex ${\bf 1}$ in combination with other electrode materials. This suggests that the first oxidation wave above 1.6 V seen on both PG and GC (Fig. 3.7b) might be related to specific interactions between the catalyst and a graphitic electrode surface. The difference in oxygen evolution activity of complex ${\bf 1}$ on a graphitic working electrode compared to a gold working electrode strongly suggests a mechanism other than the involvement of surface oxides which has previously been suggested for a flavin-based water oxidation catalyst. [2] Instead, hydrophobic interactions for example in the form of π - π stacking between the aromatic Hbbpya ligand and an sp² carbon surface might take place. [23-28] The substrate influence of graphitic electrodes has an apparent beneficial influence on the water oxidation capabilities of complex ${\bf 1}$, leading to a significantly earlier onset of oxygen evolution on PG and GC working electrodes compared to BDD and gold working electrodes.

When comparing the voltammogram recorded for a PG working electrode in a blank $0.1 \text{ M Na}_2\text{SO}_4$ solution before and after being cycled 3 times between 1.3 and 2.0 V at 1 mV/s in the presence of complex 1, we found no difference in the recorded current. This means that the interaction between complex 1 and the surface of a graphitic electrode must be highly reversible in nature and does not lead to the formation of a lasting adsorbed state.

3.2.5 Kinetic considerations

To compare the catalytic activity of complex ${\bf 1}$ between a gold working electrode and a graphitic working electrode and also to compare the catalytic activity of complex ${\bf 1}$ with other catalysts reported in literature, it is important to know the rate at which catalysis occurs. We used equation 1 to determine the TOF of complex ${\bf 1}$ at different overpotentials. [29] In this equation, ${\bf v}$ is the scan rate of the experiment, ${\bf i}_p$ is the current of oxidation wave X (cf. Fig. 3.2 and Fig. 3.5) while ${\bf i}_{cat}$ is the catalytic current at the potential for which the TOF is to be determined. Additional details about the calculations are available in appendix B.

$$TOF = 0.4848 \cdot \nu \left(\frac{i_{cat}}{i_p}\right)^2 \tag{1}$$

For the case of complex $\bf 1$ with a PG working electrode we calculated the TOF at 1.75 V. For the comparison with gold we calculated the TOF of complex $\bf 1$ with a gold working electrode at 1.9 and 2.0 V respectively. We refrained from calculating a TOF for complex $\bf 1$ with a PG electrode at potentials higher than 1.75 V since the rate of CO_2 formation becomes non-negligible as is evident from the OLEMS measurement (Fig. 3.6). For the case of a PG working electrode a TOF of 0.4 s⁻¹ was found for complex $\bf 1$ at 1.75 V while for the case of a gold working electrode, TOFs of 0.4 and 1.4 s⁻¹ were found for complex $\bf 1$ at 1.9 and 2.0 V respectively. The comparison shows that complex $\bf 1$ reaches the same TOF at 150 mV less overpotential with a PG working electrode compared to a gold working electrode.

Comparison of the catalytic performance with data from literature is complicated by the fact that the majority of kinetic studies has been carried out in the presence of chemical oxidants rather than electrochemically which leads to a poorly defined overpotential for those cases.

However, the rate determined for complex ${\bf 1}$ with graphitic working electrodes compare favourably to values reported in literature despite the comparatively modest overpotential of 520 mV (1.75 V vs. RHE) as most iron-based catalysts have been reported to exhibit TOFs of the order of $0.1~\text{s}^{-1}$ or lower in water. Typical examples range from $0.012~\text{s}^{-1}$ reported by Akermark et al. to $0.23~\text{s}^{-1}$ for the Fe(bpmcn) system reported by Costas et al. [30-31] Some notable exceptions are the Fe(TAML) catalysts by Collins et al. and the Fe(ppq) catalyst by Thummel et al. for which initial rates of $1.3~\text{s}^{-1}$ and $2.2~\text{s}^{-1}$ respectively were found in the presence of excess CAN. [5, 32]

3.3 Conclusions

Complex 1 was found to be active as an electrocatalyst for the water oxidation reaction. Results obtained from EQCM experiments rule out the possibility of the formation of a solid deposit on the electrode surface as the true catalytic species, highlighting the stability of complex 1 under catalytic conditions and providing evidence for the molecular nature of the catalytically active species.

The results of CV experiments show a clear shift in the observed Fe^{II}/Fe^{III} redox behaviour after exposure of complex 1 to high potentials (2.0 V vs. RHE) which suggests that complex 1 is merely the pre-catalyst and not the true active species. However, in a subsequent CV experiment the original redox behaviour of complex

1 was recovered over time, showing that the change in redox behaviour is reversible and that the dimeric structure of complex **1** is regenerated.

Compared to other iron-based water oxidation electrocatalysts, complex 1 exhibits a remarkably low onset potential of oxygen evolution in combination with a PG working electrode with a recorded overpotential on the scale of only 300-400 mV with respect to the thermodynamic potential of the water oxidation reaction of 1.23 V. Based on a comparison of the catalytic behavior of complex 1 with working electrodes made up of different materials, the onset potential of oxygen evolution observed in the case of graphitic working electrodes is significantly lower compared to experiments with a gold working electrode, demonstrating a strong substrate influence of the electrode material on the catalytic performance.

Additionally, our analysis of the kinetics of the catalytic reaction suggest that complex **1** performs better in combination with a graphitic working electrode compared to a gold working electrode as 150 mV more overpotential are required to achieve the same turnover frequency for complex **1** in case of a gold working electrode compared to a PG working electrode. This means that for any attempts to benchmark water oxidation catalysts electrochemically a possible influence of the electrode material must be considered.

To the best of our knowledge, our findings represent the first evidence that substrate effects of the electrode material can lead to a significant reduction of the overpotential of a homogeneous electrocatalyst for the water oxidation reaction, emphasizing the importance of the electrode material in electrocatalytic applications.

3.4 Experimental

3.4.1 General

tert-Butylamine was purchased from Acros Organics. 2,2'-Bipyridine, mCPBA, 6-bromo-2,2'-bipyridine, (S)-BINAP, iron powder, PhCF₃ and KOtBu were purchased from Sigma Aldrich. p-Toluensulfonic acid anhydride was purchased from VWR. Pd(dba)₂, TFA and MTBE were purchased from Fisher Scientific. All chemicals were used as received and without further purification. The concentration of mCPBA was determined via titration with sodium thiosulfate before use. (S)-BINAP, iron powder, PhCF₃ and KOtBu were stored under argon.

2,2'-Bipyridine mono N-oxide, 6-amino-2,2'-bipyridine and *N,N*-bis(2,2'-bipyrid-6-yl)amine were synthesized according to literature procedures. [33-35] Solvents were degassed according to standard freeze-pump-thaw protocols.

UV-vis spectra were recorded on a Varian Cary 50 Scan spectrophotometer. Mass spectra were measured on a Thermo Scientific MSQ Plus ESI spectrometer. Elemental analyses were performed by Mikroanalytisches Laboratorium Kolbe in Germany.

3.4.2 Electrochemical experiments

All electrochemical measurements with the exception of the EQCM experiments (details below) were performed in custom made single-compartment glass cells, recorded on Ivium potentiostats, operated by IviumSoft software, using a three electrode setup with the working electrode in hanging meniscus configuration. The working electrodes used in the experiments were a pyrolytic graphite (PG) disc, two gold disc electrodes of different sizes, a glassy carbon (GC) rod and a boron doped diamond (BDD) disc. The respective (geometric) surface areas are 0.2 cm² (PG), 0.13 cm² and 0.5 cm² (gold), and 0.07 cm² (GC and BDD). A large surface area gold plate was used as a counter electrode in all experiments. The reference electrode was a reversible hydrogen electrode (RHE) made up of a platinum mesh in H₂-saturated electrolyte at the same pH as the electrolyte solution inside the cell. The cell and the reference electrode were connected via a Luggin capillary.

The PG electrode was prepared before each experiment by polishing the electrode surface with sandpaper. The GC electrode was prepared by polishing the electrode surface with sandpaper first and subsequently with alumina suspensions (1.0 micron followed by 0.3 micron). For both the PG and the GC electrodes, the polishing was followed by removal of excess debris by sonicating the electrode in Milli-Q water for at least 5 minutes.

The gold electrodes were prepared before each experiment by oxidizing the surface at 10 V for 30 s in a $10\%~H_2SO_4$ solution, followed by stripping of the gold oxide layer in a 6 M HCl solution and subsequent electro-polishing of the electrode by scanning for 200 cycles between 0.0 and 1.75 V vs. RHE at 1000 mV/s in a 0.1 M HClO₄ electrolyte solution.

The BDD electrode was prepared before each experiment by sonication for 5 minutes in concentrated HNO_3 followed by sonication for 5 minutes in Milli-Q water.

All glassware used in electrochemical measurements was routinely cleaned of any organic contamination by boiling in a 3:1 mixture of concentrated sulfuric and nitric acid. Prior to each experiment, the glassware was cleaned by threefold rinsing and boiling in Milli-Q water. All electrolyte solutions were prepared from p.a. grade chemicals (Merck Suprapur®) and Milli-Q water (resistivity > 18.2 M Ω). Prior to measurements, the electrolyte solution was purged of air by bubbling with argon (Linde, Ar 6.0) for at least 20 minutes. During the measurements, the cell was constantly kept under argon flow to prevent air from entering.

For the OLEMS measurements, the gasses formed at the working electrode were collected via a hydrophobic tip (KEL-F with a porous Teflon plug) in close proximity to the surface of the working electrode and analyzed in a QMS 200 mass spectrometer. A detailed description of the OLEMS setup is available elsewhere. [12] For the mass spectrometry data recorded during cyclic voltammetry experiments, background correction was done by assuming an exponential decay fit (concerns figures 3.4, 3.6, B.6 and B.8).

EQCM experiments were performed in a 3 mL Teflon cell purchased from Autolab. The top part of the cell was modified to allow for electrochemical measurements under an inert atmosphere. For further details, see figure B.9, Appendix B. The EQCM was controlled by an Autolab potentiostat operated by NOVA 2.0 software. Autolab EQCM electrodes with a surface area of 1.5 cm² consisting of a 200 nm gold layer deposited on a quartz crystal were used as working electrodes. A custom made RHE reference electrode was used which is described elsewhere. [13]

3.4.3 Synthesis of $Fe(OTf)_2 \cdot 5.5H_2O$

Iron powder (1.44 g, 25.8 mmol) was carefully added in portions to 4.5 mL 98% triflic acid (50.0 mmol) in 30 mL water at room temperature while stirring. After all gas evolution ceased, the mixture was heated to 60°C for 1 h while maintaining stirring. The remaining solids were removed by filtration and the water was evaporated under vacuum, yielding a white powder with a slight blue/green hue which was dried under vacuum. Yield: 8.6 g (19.0 mmol, 76%)

The dried product was stored under argon to prevent subsequent changes in the hydration state over time.

Elemental analysis calcd. (%) for $C_2F_6Fe_2O_6S_2\cdot 5.5H_2O$ (453.0 g/mol): C 5.30, H 2.45, N 0.00 Found: C 5.28, H 2.46, N 0.00.

3.4.4 Synthesis of [(MeOH)Fe(Hbbpya)- μ -O-(Hbbpya)Fe(MeOH)](OTf)₄ (1)

N,N-bis(2,2'-bipyrid-6-yl)amine (24 mg, 0.07 mmol) was dissolved in 2 mL degassed methanol. Subsequently Fe(OTf)₂·5.5H₂O (34 mg, 0.07 mmol) dissolved in 2 mL degassed methanol was added, resulting in a deep red solution. The mixture was left to stir over night under N_2 atmosphere at room temperature. After removal of the solvent in vacuum, the obtained crude product was dissolved in a small amount of methanol (~1 mL). Complex 1 was obtained as dark brown crystals through slow vapor diffusion of diethyl ether into the methanolic solution of the crude product in air. The crystals were collected by filtration, washed with diethyl ether followed by washing with a small amount of cold methanol and subsequently dried in air. Yield: 39 mg (0.03 mmol, 73%)

ESI-MS (H_2O): Found: $[Fe^{III}(bbpya)-\mu-O-(bbpya)Fe^{III}]^{2+}$ m/z = 388.6; calcd.: m/z = 388.1

Elemental analysis calcd. (%) for $C_{46}H_{38}F_{12}Fe_2N_{10}O_{15}S_4\cdot 2H_2O$ (1474.0 g/mol): C 37.46, H 2.87, N 9.50; Found: C 37.61, H 2.91, N 9.63.

3.4.5 Sample preparation

Due to slow dissolution of complex $\bf 1$ in 0.1 M Na₂SO₄ electrolyte solution, the complex was initially dissolved in a small amount of Milli-Q water (typically 1-2 mL) and subsequently added to the electrochemical cell containing the electrolyte solution. The concentration of electrolyte in the cell was adjusted to account for the resulting dilution.

For electrochemical experiments with complex **1**, the complex was dissolved in air-saturated Milli-Q water and subsequently added to the electrochemical cell after complete dissolution. The electrolyte was then purged of air again by bubbling with argon for several minutes. To achieve faster dissolution of complex **1** in water, the crystals were powderized before dissolving them in water.

For electrochemical experiments with Fe(OTf)₂, the salt was dissolved in a small amount of electrolyte taken from the electrochemical cell and subsequently added again to the electrochemical cell after complete dissolution. The electrolyte was then purged of air again by bubbling with argon for several minutes.

All experiments in this report were performed at concentrations of 0.5 mM for complex $\bf 1$ and 1 mM for Fe(OTf)₂ unless otherwise specified.

3.5 Supporting Info

The following supplementary information can be found in Appendix B: Details about the structural features in the crystal structure of complex (Fig. B.1-B.3), mass spectrometric data for complex 1 in water (Fig. B.4), UV-vis spectra of complex 1 in aqueous solution (Fig. B.5), results of an OLEMS blank experiment with a gold working electrode (Fig. B.6), a voltammogram of complex 1 recorded with a BDD working electrode (Fig. B.7), results of an OLEMS experiment of Fe(OTf)₂ with a PG working electrode (Fig. B.8), a depiction of the modified cell used in EQCM experiments (Fig. B.9), details about the calculation of turnover frequencies of complex 1 with gold and PG working electrodes as well as crystallographic data of complex 1.

3.6 References

- [1] A. J. Bard; L. R. Faulkner, In *Electrochemical methods: fundamentals and applications*, 2nd ed.; Wiley: 2001; pp 115-117.
- [2] E. Mirzakulova; R. Khatmullin; J. Walpita; T. Corrigan; N. M. Vargas-Barbosa; S. Vyas; S. Oottikkal; S. F. Manzer; C. M. Hadad; K. D. Glusac, *Nat. Chem.* **2012**, *4*, 794-801.
- [3] S. W. Sheehan; J. M. Thomsen; U. Hintermair; R. H. Crabtree; G. W. Brudvig; C. A. Schmuttenmaer, *Nat. Commun.* **2015**, *6*, 6469.
- [4] T. J. Collins, Acc. Chem. Res. **1994**, 27, 279-285.
- [5] L. D. Wickramasinghe; R. Zhou; R. Zong; P. Vo; K. J. Gagnon; R. P. Thummel, *J. Am. Chem. Soc.* **2015**, *137*, 13260-13263.
- [6] M. M. Najafpour; A. N. Moghaddam; D. J. Sedigh; M. Hołyńska, *Catal. Sci. Technol.* **2014**, *4*, 30-33.
- [7] B. Zhang; F. Li; F. Yu; H. Cui; X. Zhou; H. Li; Y. Wang; L. Sun, *Chem. Asian J.* **2014**, *9*, 1515-1518.
- [8] D. Wang; L. Que, Jr., Chem. Commun. 2013, 49, 10682-10684.
- [9] A. R. Parent; T. Nakazono; S. Lin; S. Utsunomiya; K. Sakai, *Dalton Trans.* **2014**, *43*, 12501-12513.
- [10] C. R. Martinez; B. L. Iverson, *Chem. Sci.* **2012**, *3*, 2191-2201.
- [11] O. Diaz-Morales; T. J. Hersbach; D. G. H. Hetterscheid; J. N. Reek; M. T. M. Koper, *J. Am. Chem. Soc.* **2014**, *136*, 10432-10439.
- [12] A. H. Wonders; T. H. M. Housmans; V. Rosca; M. T. M. Koper, *J. Appl. Electrochem.* **2006**, *36*, 1215-1221.
- [13] P. Abril; M. P. del Río; C. Tejel; T. W. G. M. Verhoeven; J. W. H. Niemantsverdriet; C. J. M. van der Ham; K. G. Kottrup; D. G. H. Hetterscheid, *ACS Catal.* **2016**, *6*, 7872-7875.

- [14] U. Hintermair; S. W. Sheehan; A. R. Parent; D. H. Ess; D. T. Richens; P. H. Vaccaro; G. W. Brudvig; R. H. Crabtree, *J. Am. Chem. Soc.* **2013**, *135*, 10837-10851.
- [15] B. Limburg; E. Bouwman; S. Bonnet, Coord. Chem. Rev. 2012, 256, 1451-1467.
- [16] O. Diaz-Morales; F. Calle-Vallejo; C. de Munck; M. T. M. Koper, *Chem. Sci.* **2013**, *4*, 2334-2343.
- [17] G. Chen; L. Chen; S. M. Ng; W. L. Man; T. C. Lau, *Angew. Chem., Int. Ed.* **2013**, *52*, 1789-1791.
- [18] Y. Lin; S. Zhou; S. W. Sheehan; D. Wang, J. Am. Chem. Soc. **2011**, 133, 2398-2401.
- [19] M. T. Mayer; C. Du; D. Wang, J. Am. Chem. Soc. 2012, 134, 12406-12409.
- [20] K. M. H. Young; B. M. Klahr; O. Zandi; T. W. Hamann, *Catal. Sci. Technol.* **2013**, *3*, 1660-1671.
- [21] N. D. Schley; J. D. Blakemore; N. K. Subbaiyan; C. D. Incarvito; F. D'Souza; R. H. Crabtree; G. W. Brudvig, *J. Am. Chem. Soc.* **2011**, *133*, 10473-10481.
- [22] C. J. M. van der Ham; F. Işık; T. W. G. M. Verhoeven; J. W. Niemantsverdriet; D. G. H. Hetterscheid, *Catal. Today* **2017**, *290*, 33-38.
- [23] J. Björk; F. Hanke; C.-A. Palma; P. Samori; M. Cecchini; M. Persson, *J. Phys. Chem. Lett.* **2010**, *1*, 3407-3412.
- [24] A. Rochefort; J. D. Wuest, Langmuir 2009, 25, 210-215.
- [25] S. D. Chakarova-Kack; E. Schroder; B. I. Lundqvist; D. C. Langreth, *Phys. Rev. Lett.* **2006**, *96*, 146107.
- [26] M. A. Morales Vásquez; M. Hamer; N. I. Neuman; A. Y. Tesio; A. Hunt; H. Bogo; E. J. Calvo; F. Doctorovich, *ChemCatChem* **2017**.
- [27] C. Rajesh; C. Majumder; H. Mizuseki; Y. Kawazoe, *J. Chem. Phys.* **2009**, *130*, 124911.
- [28] Z. Wang; H. Lei; R. Cao; M. Zhang, *Electrochim. Acta* **2015**, *171*, 81-88.
- [29] J. M. Saveant; E. Vianello, *Electrochim. Acta* **1965**, *10*, 905-920.
- [30] J. L. Fillol; Z. Codola; I. Garcia-Bosch; L. Gomez; J. J. Pla; M. Costas, *Nat. Chem.* **2011**, *3*, 807-813.
- [31] B. Das; B. L. Lee; E. A. Karlsson; T. Akermark; A. Shatskiy; S. Demeshko; R. Z. Liao; T. M. Laine; M. Haukka; E. Zeglio; A. F. Abdel-Magied; P. E. Siegbahn; F. Meyer; M. D. Karkas; E. V. Johnston; E. Nordlander; B. Akermark, *Dalton Trans.* **2016**, *45*, 13289-13293.
- [32] W. C. Ellis; N. D. McDaniel; S. Bernhard; T. J. Collins, *J. Am. Chem. Soc.* **2010**, *132*, 10990-10991.
- [33] T. Norrby; A. Börje; L. Zhang; B. Åkermark; J. H. Wagenknecht; G. W. Francis; J. Szúnyog; B. Långström, *Acta Chem. Scand.* **1998**, *52*, 77-85.
- [34] J. Yin; B. Xiang; M. A. Huffman; C. E. Raab; I. W. Davies, *J. Org. Chem.* **2007**, 72, 4554-4557.
- [35] S. Zheng; N. R. Reintjens; M. A. Siegler; O. Roubeau; E. Bouwman; A. Rudavskyi; R. W. Havenith; S. Bonnet, *Chem. Eur. J.* **2016**, *22*, 331-339.

Electrochemical versus chemical oxidation – reevaluating the benchmark water oxidation catalyst α -[Fe(bpmcn)(OTf)₂] via electroanalytical methods

The complex α -[Fe(bpmcn)(OTf)₂] (1) (with bpmcn = N,N'-dimethyl-N,N'-bis(2pyridylmethyl)-cyclohexane-1,2-diamine) was first reported in 2011 by Fillol et. al as an active iron-based catalyst for the water oxidation reaction. It has since taken on a status as a benchmark system for iron-based water oxidation catalysis. In this chapter we describe the results of electroanalytical investigations of complex 1. complex **2** – the D₄-analogue in which the benzylic hydrogen atoms in the structure have been replaced with deuterium – and the non-deuterated Fe^{III} analogue complex 3. The reactivity of these complexes for water oxidation under electrochemical conditions is compared to their activity under chemically driven conditions, in particular with respect to the difference in stability between complex **1** and the D_4 analogue **2**, which was observed in the presence of excess Cerium(IV). While the results show that all three complexes are active for water oxidation at potentials ≥1.8 V vs. RHE, their performance is not exceptional compared to other iron-based electrocatalysts. Furthermore, no significant difference was found between complex 1 and 2 in terms of stability during electrocatalysis. Finally, complexes 1 and 2 were studied with different electrode materials and demonstrated a much more complicated behaviour in combination with a gold working electrode compared to a pyrolytic graphite working electrode. The underlying reasons for this behaviour are not yet fully understood.

4.1 Introduction

In 2011 Fillol and co-workers published a much-noticed report on iron-based homogeneous water oxidation catalysts. The catalyst which the best performance in their screening library was α -[Fe(bpmcn)(OTf)₂] (1) (with bpmcn = N,N'-dimethyl-N,N'-bis(2-pyridylmethyl)-cyclohexane-1,2-diamine) which in the presence of excess cerium(IV) ammonium nitrate (CAN) produced O_2 with turnover numbers of about 360 and an initial-rate turnover frequency of 0.23 s⁻¹. When periodate was used instead of CAN, turnover numbers of >1050 were reported albeit at a lower rate of 0.06 s⁻¹. While these results are very promising, the stability of the catalyst still needs to be improved to yield higher TONs in order to make the transition from a proof of concept to an actual application.

In 1994 Collins studied the degradation pathways of metal complexes in high oxidation states, developing a set of rules regarding the ligand structure for the design of transition metal complexes to be used under strongly oxidative conditions. One of the rules he established is that hydrogen atoms in β -position to heteroatom donors should be avoided as β -hydrogen elimination can occur, resulting in degradation of the ligand. The translation of his findings into the design of a new catalyst resulted in development of the tetra-amido macrocyclic ligand system (TAML) which was subsequently successfully used in water oxidation chemistry. The most active Fe-TAML complex that was found in the study (Fig. 4.1) had a remarkably high turnover frequency of 1.3 s⁻¹. However, despite following the rules established previously, the catalytic activity of the Fe-TAML catalyst was short-lived with only 16 turnovers.

Figure 4.1: Structure of the most active Fe-TAML complex reported by Collins et al. $(Y = H_2O)^{[3]}$

Following their initial report, Fillol and co-workers made efforts to identify and eliminate deactivation pathways of complex $\mathbf{1}$ to improve the catalyst lifetime. One of the major weaknesses that was identified in the structure of the complex are the benzylic $-CH_2$ - hydrogen atoms, which is in agreement with the rules

established by Collins. They open up a pathway resulting in the loss of one or both of the pyridyl groups, leading to deactivation of the catalyst. ^[4] By replacing the benzylic protium atoms with deuterium atoms, the authors were able to demonstrate an increase of the turnover number by a factor of 4-5 under the same conditions without affecting the turnover frequency. ^[4] This indicates that the mechanism of the catalytic reaction remains the same while the stability of the catalyst is improved.

Because of these very promising results we decided to investigate complex 1 and analogue D_4 - α -[Fe(bpmcn)(OTf)₂] the deuterated (2) (Fig. 4.2) using electroanalytical techniques to determine whether a similar effect of the deuteration on the catalyst lifetime can be seen in electrocatalytic applications. Since complexes 1 and 2 were found to undergo rapid ligand de-coordination in low pH aqueous media, the electrochemistry of both complexes was studied in NaClO₄ electrolyte solutions. The Fe^{III} analogue α -[Fe(bpmcn)Cl₂]Cl (3) with protium in the backbone and bearing chloride ligands instead of triflate ligands (Fig. 4.2) was found to be substantially more stable under acidic conditions and was thus also used for electrochemical experiments in acidic media.

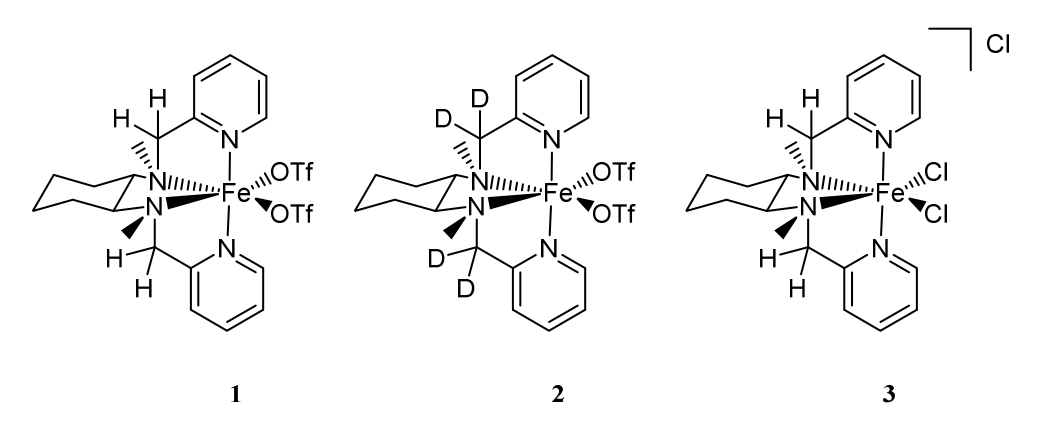


Figure 4.2: Structures of complexes 1, 2 and 3

4.2 Results

4.2.1 Stability of complexes 1-3 in solution under different pH conditions

Considering the harsh conditions of the previously reported experiments involving CAN (pH \leq 1), complexes 1 and 2 were initially studied in 0.1 M HClO₄ electrolyte solutions. Cyclic voltammetry (CV) experiments yielded identical results for both complexes. The voltammograms of both complexes initially look as expected,

showing a reversible Fe^{II}/Fe^{III} redox couple at 0.8 V vs. RHE (Fig. 4.3). However, follow-up voltammograms which were recorded 3-4 hours later show in both cases a current profile which is significantly different from the one that was recorded initially (Fig. 4.4).

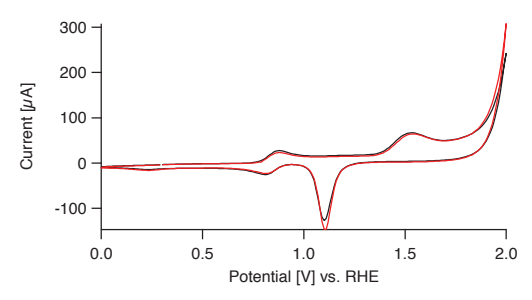


Figure 4.3: Initial voltammograms of 1.1 mM solutions of complexes 1 (red) and 2 (black) in 0.1 M $HCIO_4$. Both voltammograms were recorded with a gold working electrode, scanning between 0.0 and 2.0 V vs. RHE at 100 mV/s, starting at 0.3 V vs. RHE.

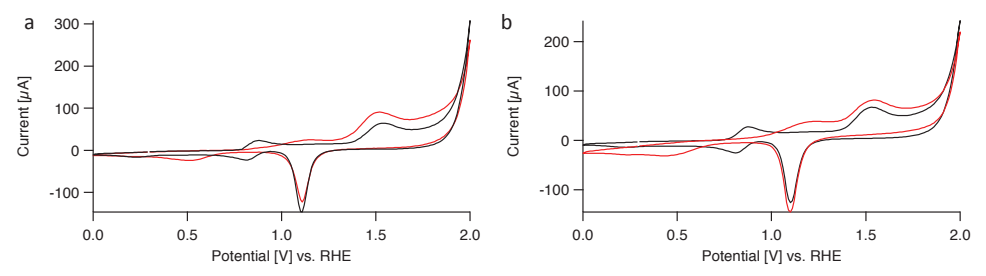


Figure 4.4: Voltammograms of (a) 1.1 mM solutions of complexes $\bf 1$ in 0.1 M HClO₄ at t=0 h (black) and after 3 h (red) and (b) 1.1 mM solutions of complexes $\bf 2$ in 0.1 M HClO₄ at t=0 h (black) and after 3.5 h (red). All voltammograms were recorded with a gold working electrode, scanning between 0.0 and 2.0 V vs. RHE at 100 mV/s, starting at 0.3 V vs. RHE.

The disappearance of the Fe^{II}/Fe^{III} redox couple over time indicates deterioration of the complex in both cases which is in agreement with previous reports which described that complexes $\bf 1$ and $\bf 2$ are unstable in solutions of 0.1 M triflic acid. [5-6] The deterioration of the complexes was also accompanied by the visible build-up of a flocculent white precipitate in the electrochemical cell (Fig. C.1, Appendix C). Accordingly, the UV-vis absorption spectrum of complex $\bf 2$ in 0.1 M HClO₄ (Fig. 4.5) shows changes on the time scale of minutes after the initial dissolution of the complex: the absorption band around 370 nm disappears while the peak at 260 nm increases with time. The decrease of the band at 370 nm has previously been attributed to the disappearance of MLCT transitions as the ligand dissociates from the metal centre while the increase of the peak at 260 nm has been attributed to a π - π * transition in the ligand which is more intense in the free

ligand compared to the coordinated ligand.^[5] In a 0.1 M NaClO₄ solution, the UV-vis absorption spectrum of complex **2** was found to be stable with no visible changes over several hours (Fig. 4.6).

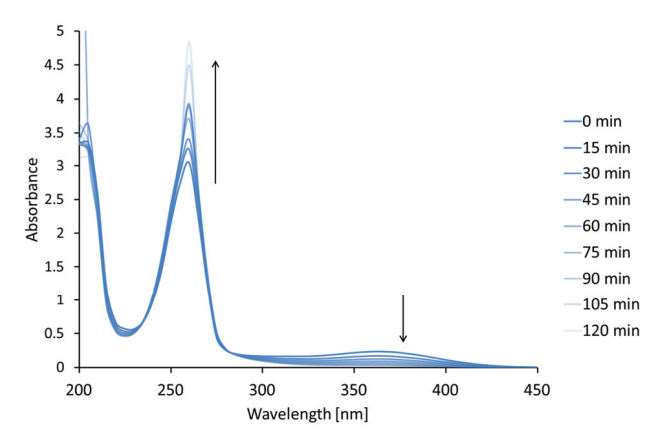


Figure 4.5: Evolution of the UV-vis absorption of complex **2** in a 0.1 M HClO₄ solution over 2 h, recorded in 15 min intervals.

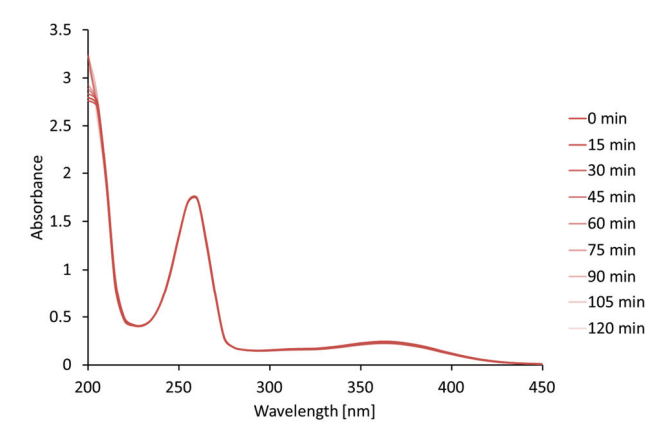


Figure 4.6: Evolution of the UV-vis absorption of complex ${\bf 2}$ in a 0.1 M NaClO $_4$ solution over 2 h, recorded in 15 min intervals.

Based on the combined results of the UV-vis and CV experiments with complexes **1** and **2**, it seems clear that both complexes are unstable in solution at low pH and stable for several hours in an unbuffered electrolyte solution.

Since complex **3** was found to dissolve poorly in solutions containing perchlorate ions, $0.1 \text{ M H}_2\text{SO}_4$ and $0.1 \text{ M Na}_2\text{SO}_4$ were chosen as the appropriate electrolyte media instead even though the sulfate ion has been shown to inhibit catalytic activity slightly compared to the perchlorate ion in some cases. ^[7] In contrast to complexes **1** and **2**, complex **3** was found to be stable under both acidic and

neutral conditions. UV-vis absorption experiments show that complex $\bf 3$ is stable in both 0.1 M H₂SO₄ and 0.1 M Na₂SO₄ for several hours with no change in the observed spectra (Fig. 4.7-4.8). The results indicate that iron in the oxidation state +III binds the bpmcn ligand stronger than iron in the oxidation state +II, resulting in a complex which is more stable in acidic media.

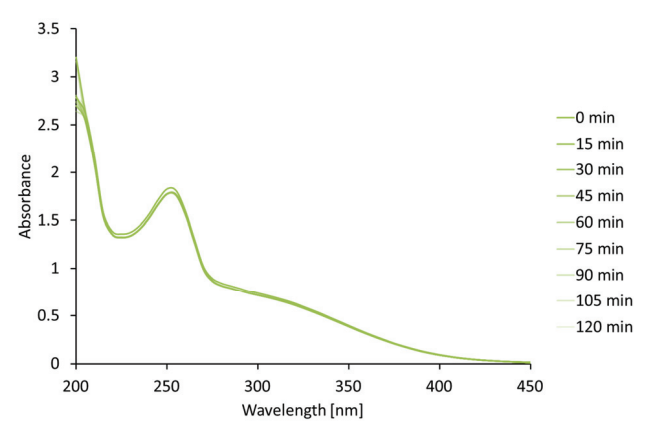


Figure 4.7: Evolution of the UV-vis absorption of complex 3 in a $0.1~M~H_2SO_4$ solution over 2 h, recorded in 15 min intervals.

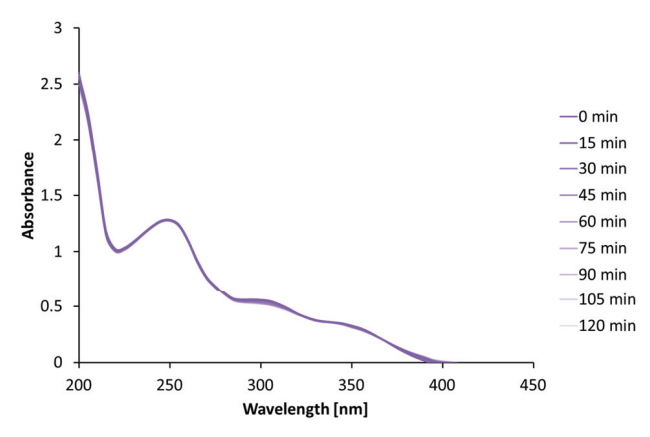


Figure 4.8: Evolution of the UV-vis absorption of complex 3 in a $0.1 \text{ M Na}_2\text{SO}_4$ solution over 2 h, recorded in 15 min intervals.

4.2.2 Electrochemistry of complexes 1 and 2

4.2.2a Cyclic voltammetry

Based on the results described in section 4.2.1, $NaClO_4$ was selected as the appropriate electrolyte for electrochemical experiments with complexes **1** and **2**. To determine any possible influence of the electrode material on the observed electrochemistry, working electrodes made from gold and pyrolytic graphite (PG) were used.

In all cyclic voltammetry experiments, complexes **1** and **2** show virtually identical behaviour. Using a gold working electrode, both complexes show a reversible Fe^{II}/Fe^{III} redox couple at 0.9 V which is followed by two oxidation waves, labeled I and II, between 1.5 and 1.9 V (Fig. 4.9) which are assigned to the formation of gold oxide at the surface of the working electrode (see section 4.2.2b). At about 1.9 V the onset of another oxidative wave is seen which could potentially indicate catalytic current. In the backward scan, a reduction wave at 1.2 V is visible which corresponds to the reduction of the oxidized electrode surface from gold oxide back to gold.

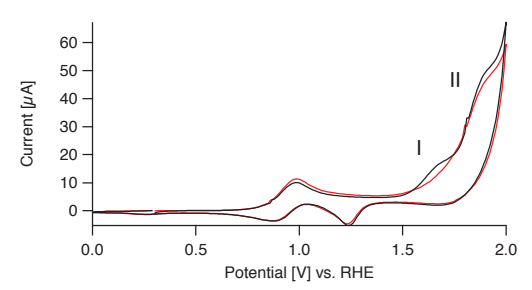


Figure 4.9: Voltammograms of 1.1 mM solutions of complexes 1 (red) and 2 (black) in 0.1 M NaClO₄. Both CVs were recorded with a gold working electrode, scanning between 0.0 and 2.0 V vs. RHE at 10 mV/s, starting at 0.3 V vs. RHE

In the first scan of the CV experiment, the current starting at 1.9 V beyond the gold oxidation waves I and II is small. A significant increase in the peak current at 2.0 V was found in subsequent scans when cycling the potential between 0.0 and 2.0 V at a scan rate of 10 mV/s (Fig. 4.10). Long-term experiments under these conditions show that for complex 1 the maximum current at 2.0 V is reached after 27 scans with most of the increase already taking place during the first few scans (Fig. 4.11a and Table 4.1). While the current at 2.0 V increased significantly over several scans, the current of the redox couple remained largely unaffected (Fig. 4.11b and Table 4.1). This is a clear indication that the complexes remain largely

intact during the experiment, meaning that the increase in peak current is unlikely to be due to the formation of a different homogeneous catalytically active species from complexes 1 and 2.

In CV experiments with a PG working electrode, complexes **1** and **2** show again a reversible Fe^{II}/Fe^{III} redox couple at 0.9 V (Fig. 4.12) as was previously seen with a gold working electrode. Beyond that, only a single irreversible oxidation wave starting at about 1.5 V can be seen in the voltammogram of complexes **1** and **2** recorded with a PG working electrode.

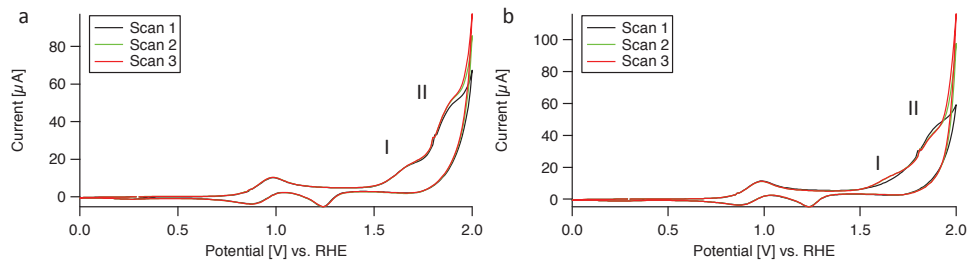


Figure 4.10: Voltammograms of 1.1 mM complex **2** (a) and 1.1 mM complex **1** (b) recorded with a gold working electrode in a 0.1 M NaClO₄ solution. Shown are 3 subsequent scans recorded between 0.0 and 2.0 V vs. RHE at a scan rate of 10 mV/s, starting each scan at 0.3 V vs. RHE.

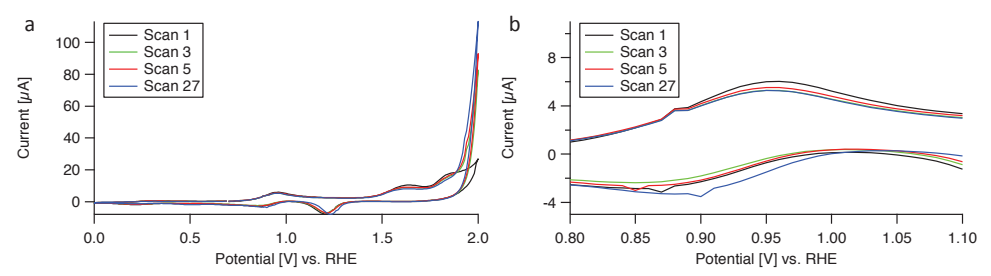


Figure 4.11: Scans 1, 3, 5 and 27 of a CV experiment of 1.1 mM complex 1 in a 0.1 M NaClO₄ solution, scanning between 0.0 and 2.0 V vs. RHE at a scan rate of 10 mV/s, starting at 0.7 V vs. RHE. (a) Full CV between 0.0 and 2.0 V vs. RHE (b) Magnification of the area between 0.8 and 1.1 V vs. RHE to highlight the Fe^{II/IIII} redox couple.

Table 4.1: Values of the current recorded for the Fe^{II/III} transition and the peak at 2.0 V vs. RHE for selected scans during a long-term CV experiment with complex **1**, corresponding to Fig. 4.11.

Scan #	Peak current Fe ^{"/"} [μΑ]	Peak current at 2.0 V [μA]
1	6	27
3	5	83
5	6	93
27	5	113

Conditions: Gold working electrode, 1.1 mM complex 1, 0.1 M NaClO $_4$, scan range: 0.0-2.0 V vs. RHE, scan rate: 10 mV/s

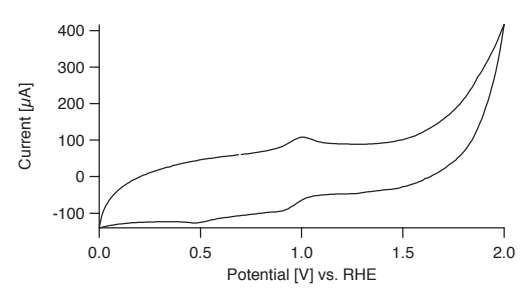


Figure 4.12: Voltammogram of 1.1 mM complex 1 in a 0.1 M NaClO $_4$ solution recorded with a PG working electrode at a scan rate of 100 mV/s between 0.0 and 2.0 V vs. RHE, starting at 0.7 V vs. RHE.

4.2.2b On-line electrochemical mass spectrometry

To assess the water oxidation capabilities of complexes **1** and **2**, on-line electrochemical mass spectrometry (OLEMS) experiments were carried out in combination with cyclic voltammetry. In OLEMS measurements, the m/z traces for selected gaseous products, sampled close to the electrode surface in solution, are recorded during electrochemical measurements.^[8] During all OLEMS experiments, m/z = 32 was recorded to monitor oxygen evolution while m/z = 44 was recorded to monitor any CO_2 formation as a result of potential oxidative decomposition of the ligand under strongly oxidizing conditions.^[9-12] In all OLEMS experiments discussed in this chapter, the potential was cycled between 1.3 and 2.0 V at 1 mV/s for a total of three cycles.

In OLEMS experiments with a PG working electrode, complex 1 demonstrates persistent water oxidation activity across all three scans (Fig. 4.13). In the corresponding current trace (Fig. 4.13, bottom), oxidative current can be seen starting at 1.5 V with a sharp increase in current at about 1.8 V. These features in the current trace are consistent with the results previously seen in the CV experiment, recorded between 0.0 and 2.0 V with a PG working electrode in the presence of complex 1 (Fig. 4.12). The mass traces for O_2 and CO_2 measured during the OLEMS experiment show onsets that correspond well with the onsets in the current trace. O_2 evolution starts at 1.8 V while CO_2 formation starts already at lower potentials around 1.5 V. The formation of CO_2 could indicate decomposition of the complex. However, similar CO_2 formation behaviour with an onset at potentials below the onset of oxygen evolution is routinely detected in OLEMS experiments with a PG working electrode for all metal complexes described in this thesis and even – albeit to a lesser extent – in the absence of any metal complex in solution (cf. chapter 5).

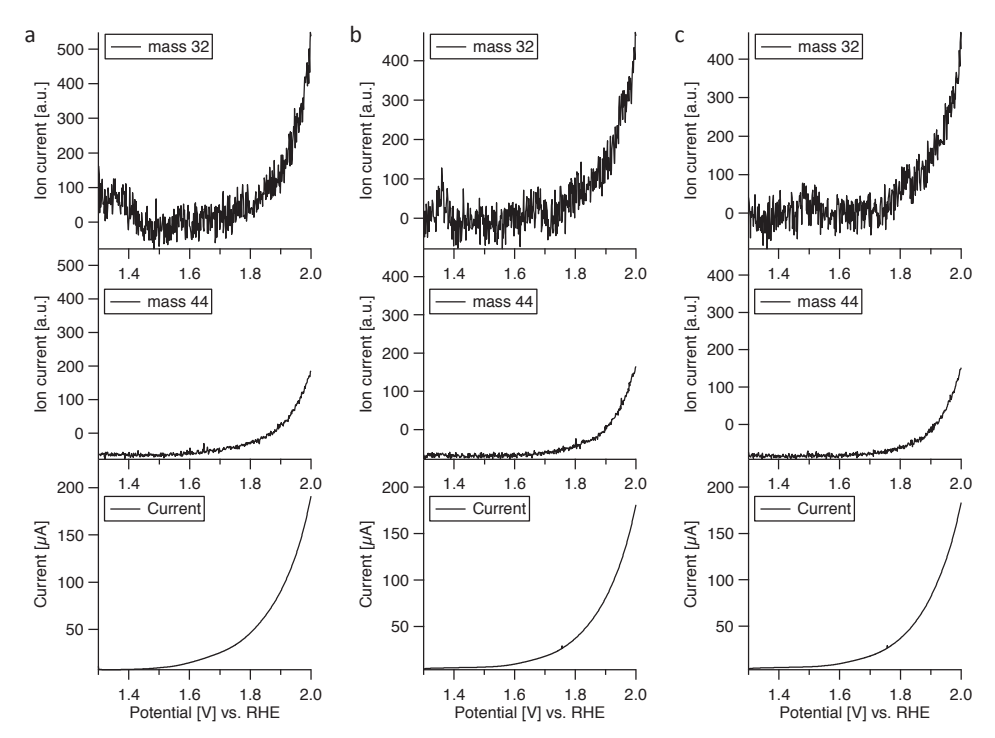


Figure 4.13: OLEMS measurement of 1.1 mM complex 1 in a 0.1 M NaClO $_4$ solution using a PG working electrode, recorded while cycling the potential between 1.3 and 2.0 V vs. RHE, starting at 1.3 V vs. RHE at a scan rate of 1 mV/s. Depicted are the m/z traces of O_2 (top), CO_2 (middle) and the corresponding current (bottom). (a) scan 1 (b) scan 2 (c) scan 3. For the sake of clarity only the forward scan of each experiment is shown.

OLEMS experiments of complexes **1** and **2** in combination with a gold working electrode instead of a PG electrode yield more complicated results. During the second and third scan of each OLEMS experiment with a gold working electrode, both complexes show again stable water oxidation activity as was previously seen in the OLEMS experiment of complex **1** with a PG working electrode. In contrast to that, both complexes show identical initial behaviour during the first scan of the OLEMS experiment with a gold working electrode, which differs substantially from their behaviour during the second and third scan. For the sake of structuring the discussion, the second and third scan of the OLEMS experiments of both complexes are discussed first, followed by a discussion of the first scan.

In the second and third scan of the OLEMS experiments, a sharp increase in the recorded current is visible, starting between 1.8 and 1.9 V. The mass traces for m/z = 32 shows an onset of oxygen evolution which correlates with the oxidative current while the mass traces for m/z = 44 show no signs of CO_2 formation (Fig. 4.14 and Fig. 4.15). The onset of oxygen formation appears to be slightly delayed

in the OLEMS experiments with a gold working electrode compared to the experiments with a PG working electrode. However, the contribution of CO_2 formation to the current in the experiment with a PG electrode makes it more difficult to determine the onset of oxygen evolution for the experiment with PG. The lack of CO_2 formation in the experiment with gold on the other hand indicates that that the CO_2 formation observed for the case of a PG working electrode is mainly due to oxidation of the electrode material itself.

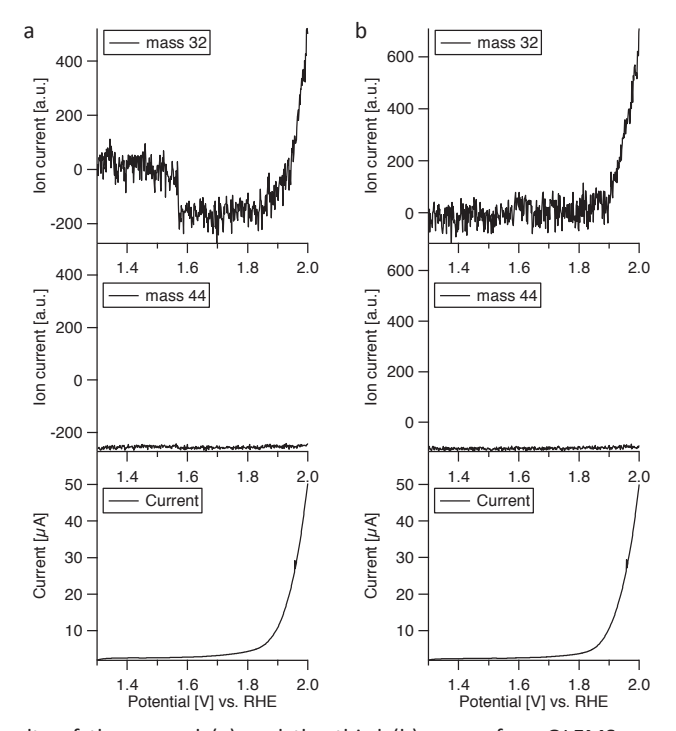


Figure 4.14: Results of the second (a) and the third (b) scan of an OLEMS experiment recorded during potential cycling with complex ${\bf 1}$ using a gold working electrode. Conditions: 1.1 mM complex ${\bf 1}$, 0.1 M NaClO₄, scan range: 1.3-2.0 V vs. RHE, starting at 1.3 V vs. RHE, scan rate 1 mV/s. Depicted are the m/z traces of O₂ (top) CO₂ (middle) and the corresponding current (bottom). For the sake of clarity, only the forward scan of each experiment is shown.

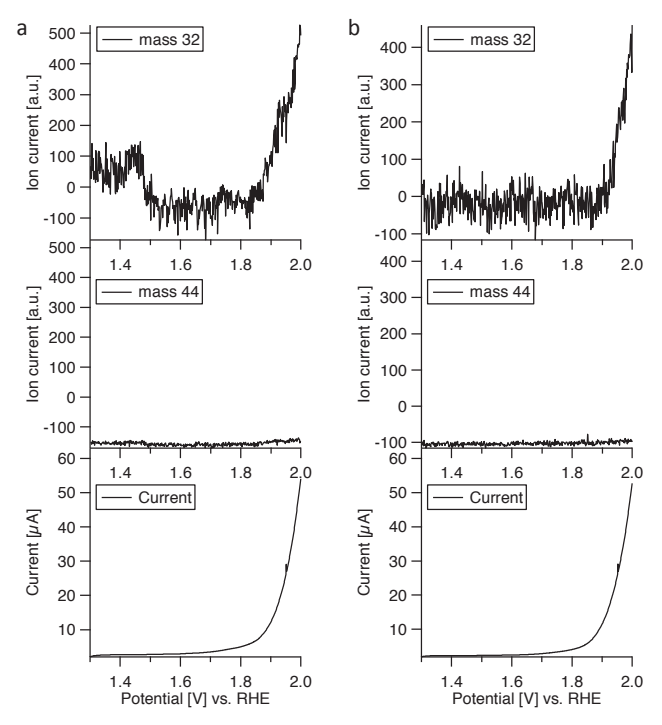


Figure 4.15: Results of the second (a) and the third (b) scan of an OLEMS experiment recorded during potential cycling with complex **2** using a gold working electrode. Conditions: 1.1 mM complex **2**, 0.1 M NaClO₄, scan range: 1.3-2.0 V vs. RHE, starting at 1.3 V vs. RHE, scan rate 1 mV/s. Depicted are the m/z traces of O₂ (top) CO₂ (middle) and the corresponding current (bottom). For the sake of clarity, only the forward scan of each experiment is shown.

In contrast to the results just described for the second and third scan of the OLEMS experiments with a gold working electrode, the results of the first scan of each OLEMS experiment are significantly different. This holds true for the mass traces and the current profile. During the first scan, the mass traces for m/z = 44 show that small quantities of CO_2 are being formed with an onset of 1.8 V while the mass traces for m/z = 32 indicate that oxygen is formed already at potentials as low as 1.6 V (Fig. 4.16, top and middle). The current that was measured during the first scan (Fig. 4.16, bottom) shows the same profile that was observed during previous CV experiments of complexes 1 and 2 with a gold working electrode, discussed in section 4.2.2a (Fig. 4.9-4.11). Starting at about 1.5 V, the two oxidation waves I and II can be seen, followed by a sharp increase in current at 1.9 V. The signal of the O_2 mass trace in figure 4.16 appears to follow the oxidative current which suggests that the current might be related to oxygen evolution. However, it is expected that the oxidation of the gold surface to gold oxide contributes significantly to the recorded current during the first scan as the

surface of the gold working electrode is not yet oxidized to gold oxide at the start of experiment.

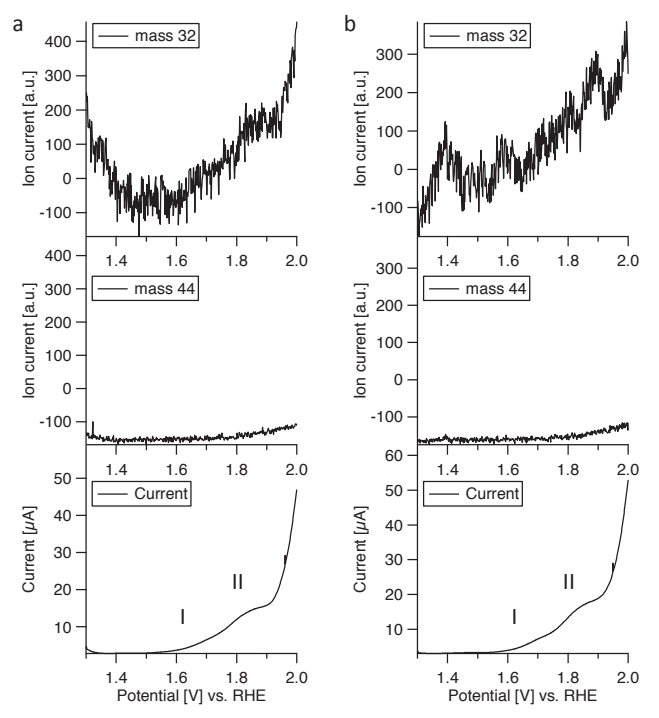


Figure 4.16: Results of the first scans of an OLEMS experiment with (a) complex $\bf 1$ and (b) complex $\bf 2$, recorded during potential cycling with complex $\bf 1$ using a gold working electrode. Conditions: 1.1 mM complex $\bf 1/2$, 0.1 M NaClO₄, scan range: 1.3-2.0 V vs. RHE, starting at 1.3 V vs. RHE, scan rate 1 mV/s. Depicted are the m/z traces of O₂ (top) CO₂ (middle) and the corresponding current (bottom). For the sake of clarity, only the forward scan of each experiment is shown.

To disentangle contributions of the complexes from contributions of gold oxide formation to the current, two back-to-back CV experiments were carried out with complex 2. Both experiments were recorded under the same conditions as the OLEMS experiment described in figures 4.14-4.16 by cycling the potential several times between 1.3 and 2.0 V at 1 mV/s. Between both experiments, the connection between the working electrode and the electrolyte was broken and subsequently re-established after brief mixing of the electrolyte solution to ensure exposure of the electrode to new, unreacted complex for the second experiment. During this entire procedure, the resting potential at the working electrode was kept at 1.3 V.

Since the surface of the gold working electrode is not yet oxidized to gold oxide at the start of the first CV experiment, the current associated with the formation of

gold oxide should contribute to the current profile of the first scan of the first experiment. By keeping the potential at the working electrode greater or equal to 1.3 V throughout the entire procedure, the reduction of the formed gold oxide is prevented. Therefore no current from gold oxide formation should be present in the voltammogram of any of the subsequent scans of the procedure. If the two current waves I and II in the first scan of the OLEMS experiment are caused by the formation of gold oxide, they should therefore only appear in the first scan of the first experiment. Additionally, the current of the first and second scan of the first experiment should differ, due to the contribution of gold oxide to the first scan, while the current of the first and second scan of the second experiment should be identical. If, on the other hand, oxidation reactions of complexes 1 and 2 contribute to the current profile of the first scan of the OLEMS experiment (Fig. 4.16, bottom), it is expected that the current profile will change from the first to the second scan in the second CV experiment as well.

The results of the first CV experiment (Fig. 4.17a) clearly show that, as expected, waves I and II are present in the first scan and absent in the second scan, as was previously seen in the OLEMS experiments. In the second CV experiment, however, waves I and II are absent and the current profiles of the first and second scan are identical (Fig. 4.17b).

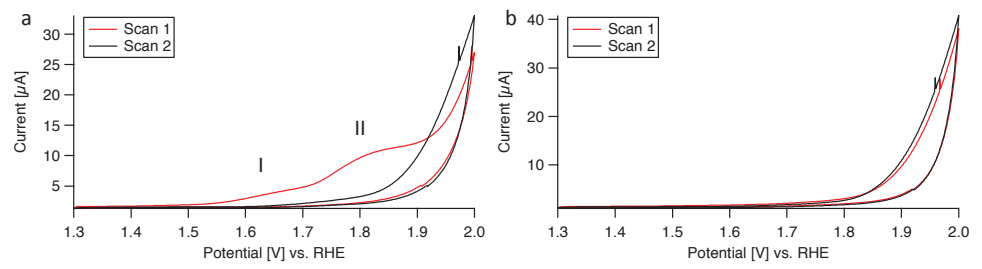


Figure 4.17: Results of two consecutive CV experiments with complex **2**, recorded with a gold working electrode in the presence of 1.1 mM complex **2** in a 0.1 M $NaClO_4$ solution, scanning between 1.3 and 2.0 V vs. RHE at a scan rate of 1 mV/s, starting each scan at 1.3 V vs. RHE. After scanning between 1.3 and 2.0 V at 1 mV/s for three cycles, the meniscus at the electrode/electrolyte interface was broken and subsequently re-formed after homogenization of the electrolyte solution to ensure exposure of the electrode to new, unreacted complex **2**. This was followed by another CV experiment between 1.3 and 2.0 V at 1 mV/s for two cycles. The resting potential at the working electrode was kept at 1.3 V throughout the entire procedure to avoid gold oxide reduction. (a) First and second scan of the first CV experiment. (b) First and second scan of the second CV experiment. For both experiments, the first scan is depicted in red while the second scan is depicted in black.

The absence of waves I and II in both scans of the second CV experiment confirms that the oxidative current is not an inherent property of complexes 1 and 2 but

instead most likely related to the formation of gold oxide at the surface of the electrode.

The amounts of O_2 that are being detected during the OLEMS experiment shown in figure 4.16 are close to the lower detection limit of the system. Therefore, it is difficult to confidently distinguish actual signals from the artefacts which are commonly present in the mass traces of some OLEMS measurements. Some examples of such artefacts are highlighted in figures C.2 and C.3 in appendix C. This raises the question whether the oxygen evolution behaviour that was observed during the first scan of each OLEMS experiment is actually indicative of a real signal or random noise instead. Therefore the OLEMS experiments of complexes 1 and 2 with a gold working electrode were carried out in duplicate with the second experiment taking place on a different day. The results show that although artefacts obscure the real features to some extent, the same qualitative oxygen evolution behaviour does indeed persist across experiments (Fig. 4.18).

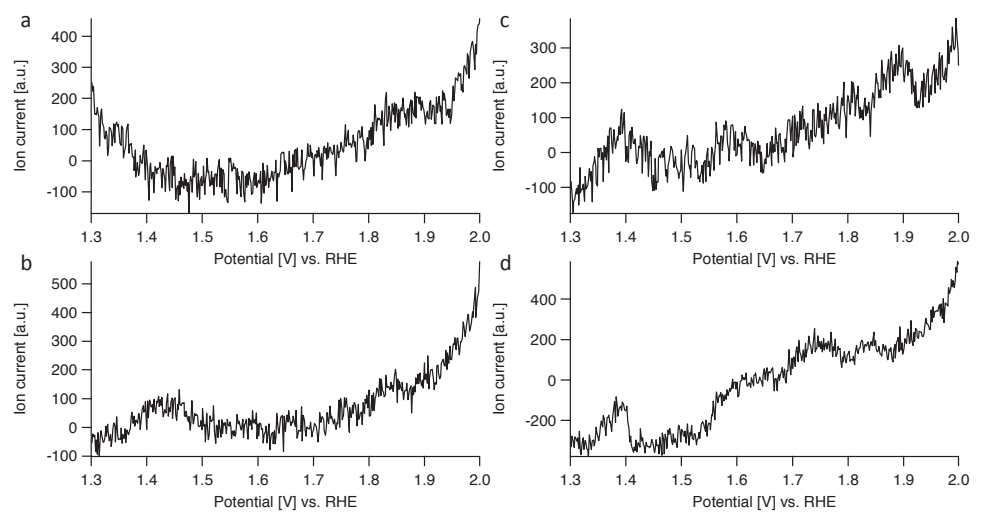


Figure 4.18: Results of several OLEMS experiments of complexes 1 and 2. Depicted are the m/z traces for O_2 of the respective first of each experiment, recorded while cycling the potential between 1.3 and 2.0 V vs. RHE with a gold working electrode in a 0.1 M NaClO₄ solution at a scan rate of 1 mV/s, starting each scan at 1.3 V vs. RHE. (a) 1.1 mM complex 1, first experiment (b) 1.1 mM complex 1, second experiment (c) 1.1 mM complex 2, first experiment (d) 1.1 mM complex 2, second experiment. In all cases only the forward scan of each experiment is shown for the sake of clarity.

4.2.2c Electrochemical quartz crystal microbalance experiments

The results of CV experiments with both complexes 1 and 2, using a gold working electrode, showed an increasing peak current at 2.0 V during repeated potential cycling between 0.0 and 2.0 V. This observation suggests that an activation of the catalyst takes place during repeated potential cycling. One possible explanation might be the formation of a catalytically active heterogeneous species at the surface of the working electrode at high potentials since heterogeneous iron-based materials such as Fe_2O_3 are known to be active water oxidation catalysts. ^[13-16] Therefore the potential formation of catalytically active heterogeneous materials is a constant concern in the field of homogeneous water oxidation catalysis. ^[10]

The fact that the Fe^{II/III} redox couple remains largely unchanged while the peak current at 2.0 V increases during CV experiments already offers some evidence that the increase in current is not related to the decomposition of the complex. Nevertheless, electrochemical quartz crystal microbalance (EQCM) experiments were carried out in order to obtain direct information about the formation of any surface deposits. The working electrode in EQCM experiments consists of a thin layer of gold, deposited on a quartz crystal oscillator. Mass changes at the working electrode can be detected by measuring changes in the resonance frequency of the quartz crystal. To avoid damaging the thin gold layer of the EQCM electrode and due to the mass change associated with gold oxide formation and reduction, the potential was kept above 1.3 V at all times during EQCM experiments to avoid gold oxide reduction.

Figure 4.19 shows the results of an EQCM experiment between 1.3 and 2.0 V at 1 mV/s, recorded with a gold working electrode in the presence of complex 1. During the first scan of the experiment (Fig. 4.19a), an increase in the vibration frequency can be seen, as is evident from a positive Δ (frequency) response. This response translates to an apparent decrease in the mass of the electrode. This seemingly strange observation has previously been attributed to bubble formation at the working electrode. After the initial increase in frequency during the first scan, no further changes in the frequency response take place in subsequent scans (Fig. 4.19b).

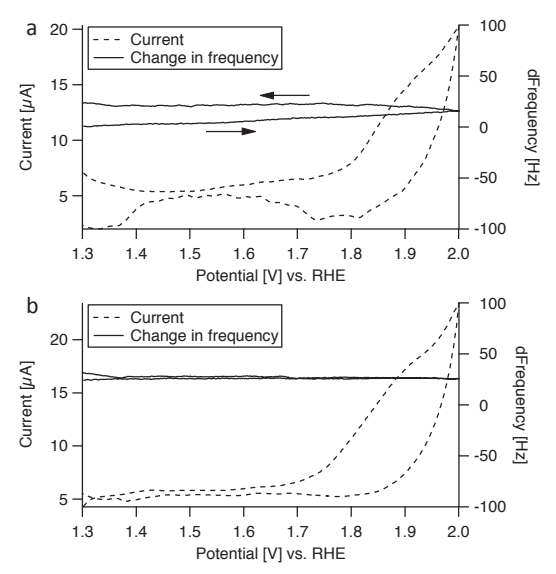


Figure 4.19: Results of EQCM experiments with 1.1 mM complex **1** in a 0.1 M NaClO $_4$ solution with a gold working electrode. Shown are the first scan (a) and the third scan (b) of a CV experiment, cycling the potential between 1.3 and 2.0 V vs. RHE at 1 mV/s, starting each scan at 1.3 V vs. RHE. The horizontal arrows indicate the direction of the scan.

4.2.3 Electrochemistry of complex 3

4.2.3a Cyclic voltammetry

The electrochemical behaviour of complex $\bf 3$ was studied in both 0.1 M Na₂SO₄ and 0.1 M H₂SO₄ electrolyte solutions, using working electrodes made from gold, PG and ITO. However, preliminary experiments with an ITO working electrode gave poor results (Fig. C.3, Appendix C) which is most likely due to its nature as a semi-conductor. As a result, we refrained from in-depth investigations with this electrode material.

Considering the instability of gold oxide in the presence of halide ions (see chapter 2, Fig 2.2), electrochemical experiments of complex **3** in combination with a gold working electrode were limited to potentials below 1.3 V. Due to the lower contribution of the background current of a gold working electrode compared to a PG working electrode, CV experiments with a gold electrode were carried out below 1.3 V with the intention of obtaining a better visualization of the Fe^{II}/Fe^{III} redox couple. Figure 4.20a shows a voltammogram of complex **3** measured between 0.0 and 1.0 V, recorded with a gold working electrode in a 0.1 M $_2$ SO₄ solution. In the forward scan of the CV experiment, there are two oxidation waves visible between 0.6 V and 1.0 V whereas the reductive current in the backward scan appears as a single wave at 0.6 V. A voltammogram between 0.0 and 2.0 V,

recorded with a PG working electrode shows the same Fe^{II}/Fe^{III} redox behaviour, albeit less discernable due to the larger contribution of background current from the PG working electrode (Fig. 4.20b). Beyond that, the voltammogram shows an oxidative wave starting at 1.5 V with a sharp increase in current around 1.8 V.

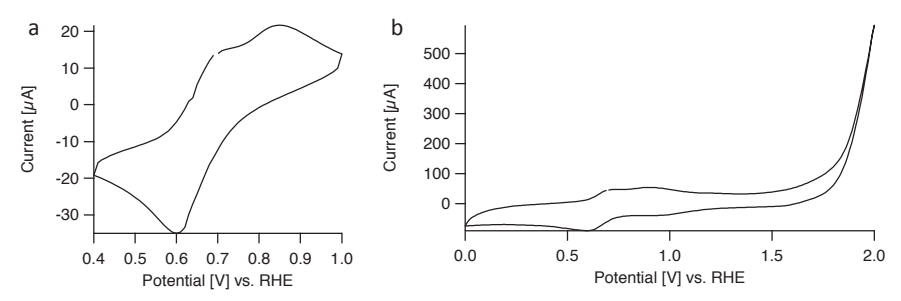


Figure 4.20: Voltammograms of 1.1 mM complex **3** in a 0.1 M $_{2}SO_{4}$ solution. Shown are (a) the range between 0.4 and 1.0 V vs. RHE, starting at 0.7 V vs. RHE, recorded with a gold working electrode and (b) the range between 0.0 and 2.0 V vs. RHE, starting at 0.7 V vs. RHE recorded with a PG working electrode. Both voltammograms were recorded at a scan rate of 100 mV/s.

In a $0.1~M~Na_2SO_4$ electrolyte solution, qualitatively identical behaviour was observed for complex **3**, compared to the results obtained in a $0.1~M~H_2SO_4$ electrolyte solution. In the voltammogram recorded with gold in a $0.1~M~Na_2SO_4$ electrolyte solution, again two oxidation waves appear between 0.7~and~1.1~V in the forward scan. The backward scan again only shows a single reduction wave at 0.7~V~(Fig.~4.21a). When scanning between 0.0~and~2.0~V~at~100~mV/s~with~a~PG~working~electrode,~a~single~broad~redox~event~between~0.7~and~1.1~V~is~resolved~in~both~directions~as~well~as~an~irreversible~oxidative~wave~starting~around~1.6~V(Fig.~4.21b).

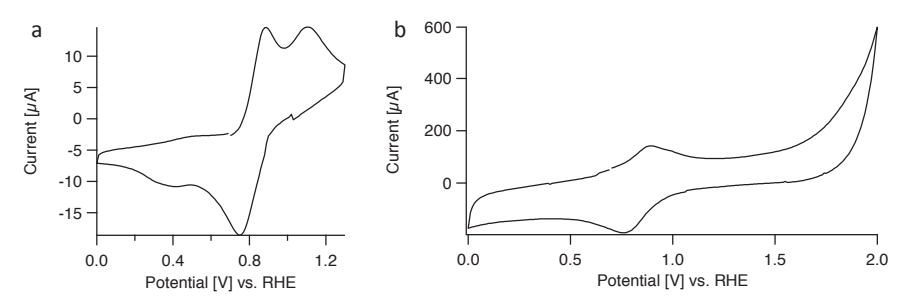


Figure 4.21: Voltammograms of 1.1 mM complex **3** in a 0.1 M Na_2SO_4 solution. Shown are (a) the range between 0.4 and 1.0 V vs. RHE, starting at 0.7 V vs. RHE, recorded with a gold working electrode and (b) the range between 0.0 and 2.0 V vs. RHE, starting at 0.7 V vs. RHE recorded with a PG working electrode. Both voltammograms were recorded at a scan rate of 100 mV/s.

The presence of two oxidation waves in the voltammograms indicates that a mixture of two species is present in solutions of complex **3**. This is in direct contrast to the results obtained for complexes **1** and **2** for which only a single Fe^{||/|||} redox couple was found. Considering the presence of chloride in the sample, one of the two oxidation peaks could be related to interactions of the metal centre with the chloride ions which are more strongly coordinating than triflate ions. However, the addition of several equivalents of sodium chloride to the electrolyte solution containing complex **3** does not result in a change in the corresponding voltammogram (Fig. 4.22).

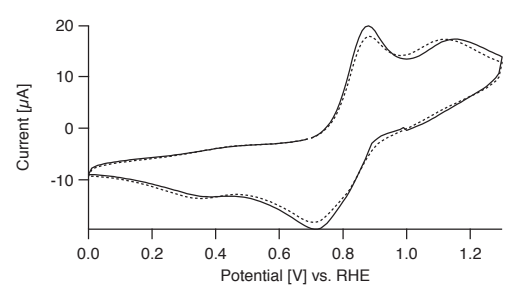


Figure 4.22: Voltammograms of 1.1 mM complex **3** in a 0.1 M Na_2SO_4 solution recorded with a gold working electrode. Shown are the result for 1.1 mM complex **1** (solid line) and 1.1 mM complex **3** + 9 equivalents of NaCl (dotted line). Both voltammograms were recorded between 0.0 and 1.3 V vs. RHE at a scan rate of 100 mV/s, starting at 0.7 V vs. RHE.

4.2.3b On-line electrochemical mass spectrometry

OLEMS experiments of complex **3** were carried out in both 0.1 M Na₂SO₄ and 0.1 M H₂SO₄ electrolyte solutions. The potential range of 1.3 to 2.0 V of the OLEMS experiments does not allow for the combination of complex **3** with a gold working electrode due to the instability of gold oxide in the presence of halide ions. Consequently, OLEMS experiments of complex **3** were performed exclusively with a PG working electrode. The results of the OLEMS experiments of complex **3** in a 0.1 M Na₂SO₄ solution (Fig. 4.23) are qualitatively similar to those obtained from OLEMS experiments of complex **1** in a 0.1 M NaClO₄ solution. In both cases, the current trace shows an oxidation wave, starting at about 1.5 V with a sharp increase in current starting near 1.8 V (Fig. 4.23, bottom). The m/z traces for both experiments show an onset of oxygen evolution around 1.8 V which correlates with the sharp increase in current. The onset of CO₂ formation (Fig. 4.23, middle) lies around 1.5–1.6 V, correlating with the onset of oxidative current in the current trace (4.23, bottom).

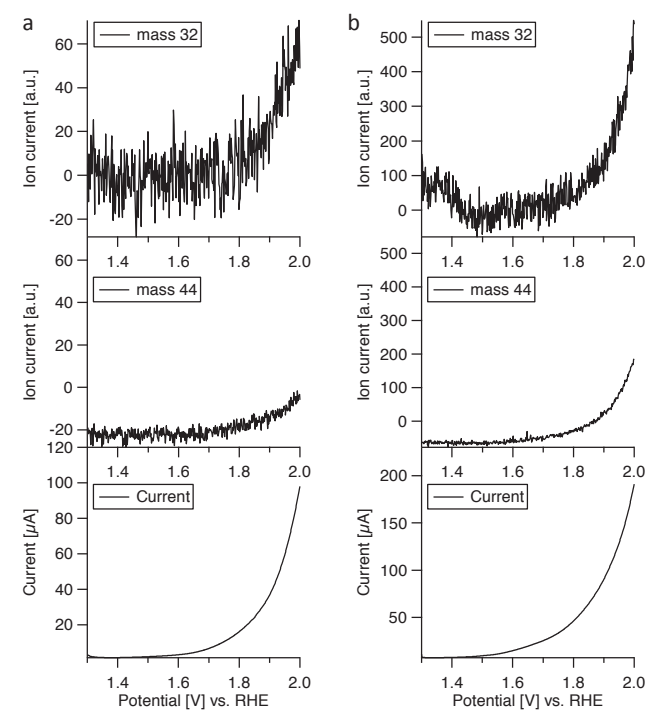


Figure 4.23: OLEMS measurements of (a) 1.1 mM complex **3** in a 0.1 M Na_2SO_4 solution and (b) 1.1 mM complex **1** in a 0.1 M $NaCIO_4$ solution (cf. Fig. 4.13a). Both experiments were recorded with a PG working electrode, cycling the potential between 1.3 and 2.0 V vs. RHE, starting at 1.3 V vs. RHE at a scan rate of 1 mV/s. Depicted are the m/z traces of O_2 (top), CO_2 (middle) and the corresponding current (bottom). For the sake of clarity only the forward scan of each experiment is shown.

The OLEMS experiment of complex $\bf 3$ in 0.1 M H₂SO₄ (Fig. 4.24) shows a behaviour that is qualitatively similar to that observed in 0.1 M Na₂SO₄. From 1.6 V onward, oxidative current can be seen in the current trace (Fig. 4.24, bottom) which correlates with the onset of CO₂ formation (Fig. 4.24, middle). The onset of oxygen evolution lies near 1.8 V (Fig. 4.24, top), correlating with a sharp increase in oxidative current visible in the current trace.

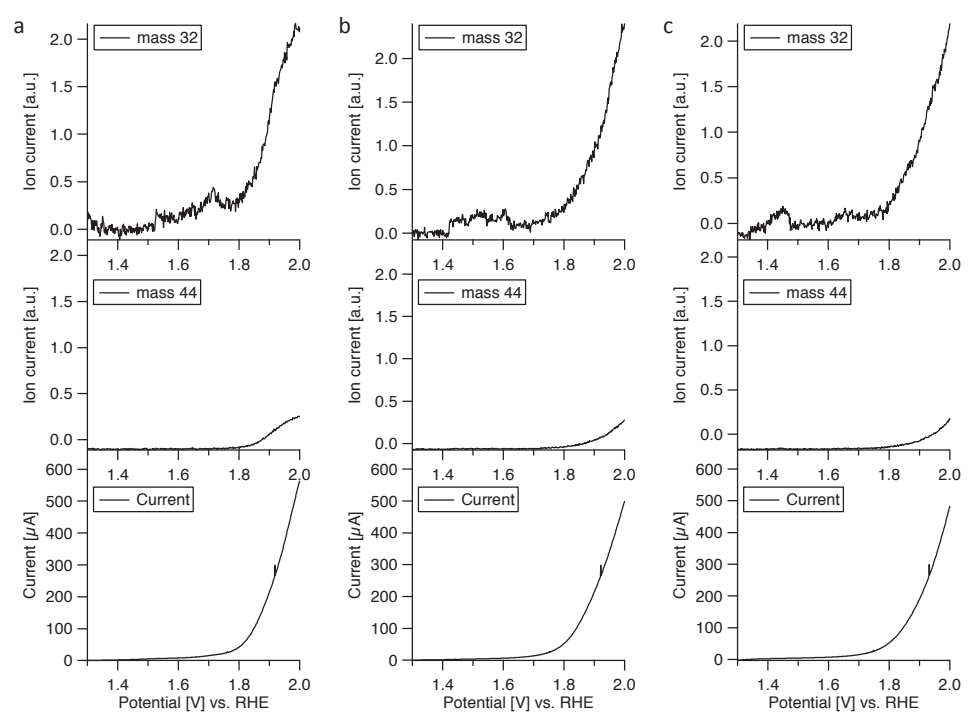


Figure 4.24: OLEMS measurement of 1.1 mM complex 3 in a 0.1 M H_2SO_4 solution using a PG working electrode, recorded while cycling the potential between 1.3 and 2.0 V vs. RHE, starting at 1.3 V vs. RHE at a scan rate of 1 mV/s. Depicted are the m/z traces of O_2 (top), CO_2 (middle) and the corresponding current (bottom). (a) scan 1 (b) scan 2 (c) scan 3. For the sake of clarity only the forward scan of each experiment is shown.

4.3 Discussion

One of the key research questions of this chapter was to investigate whether the significantly higher stability of complex 2 compared to complex 1 in experiments with chemical oxidants can also be observed during electrochemically driven water oxidation. Considering that the difference in turnover numbers between complexes 1 and 2 was found to be of the order of 4-5 in the presence of chemical oxidants, one would expect to find clear evidence for the increased robustness of complex 2 in the electrochemistry of both complexes if similar effects also play a role under electrochemical conditions. Instead, the results of cyclic voltammetry and on-line electrochemical mass spectrometry experiments showed that complexes 1 and 2 behave virtually identically in all experiments.

The electrochemistry of complexes **1** and **2** in combination with a PG working electrode is well behaved in the sense that no major changes were observed over time during electrochemical experiments. In CV experiments a single Fe^{II}/Fe^{III}

redox couple is observed at 0.9 V, followed by an irreversible oxidative wave starting at 1.5 V (Fig. 4.12) which could be assigned to a combination of oxygen evolution and CO_2 formation with an onset around 1.8 V for oxygen evolution and 1.5 V for CO_2 formation (Fig 4.13). Based on the OLEMS experiments with a PG working electrode alone, the source of the CO_2 cannot directly be determined unambiguously. The fact that very little CO_2 formation was observed during OLEMS experiments of complexes 1 and 2 with a gold working electrode, however (Fig. 4.14-4.16), suggests that the CO_2 formed during experiments with a PG electrode originates mainly from oxidation of the electrode material. In summary, the behaviour of complexes 1 and 2 in combination with a PG working electrode is consistent with a stable catalytic system.

When a gold working electrode is used instead of a PG electrode, the resulting electrochemistry of complexes 1 and 2 becomes significantly more complex. CV experiments between 0.0 and 2.0 V at 10 mV/s and OLEMS experiments between 1.3 and 2.0 V at 1 mV/s both showed a dynamic behaviour which evolved between scans for both complexes in combination with a gold working electrode. In the CV experiment between 0.0 and 2.0 V an increase in the peak current can be seen with each scan (Fig 4.10-4.11 and Table 4.1). In contrast, the current recorded during the OLEMS experiments between 1.3 and 2.0 V does not show a significant increase in current at 2.0 V with each scan (Fig 4.14-4.16, bottom). This difference suggests that cycling over the gold oxidation and gold oxide reduction potential is a key factor for the increase in current at 2.0 V during prolonged potential cycling. However, in the OLEMS experiments with a gold working electrode, the current profile of the first scan is clearly different from the current profile of the second and third scan. The current trace of the first scan (4.16, bottom) shows the same two oxidation waves I and II between 1.5 and 1.9 V that were previously seen in CV experiments between 0.0 and 2.0 V (Fig. 4.9-4.10).

It is expected that the formation of gold oxide contributes at least to some extent to the oxidative current in the region between 1.3 and 2.0 V. In the CV experiment between 0.0 and 2.0 V, the gold oxide layer is reduced again in the backward scan of every cycle at potentials below 1.3 V which is why the same contribution from gold oxide formation is expected in every scan. In the OLEMS experiment between 1.3 and 2.0 V, however, the reduction of gold oxide is prevented since the potential never goes below 1.3 V. Therefore, the difference in the current profile between the first and the second scan of the OLEMS experiments is likely due to the formation of gold oxide during the first scan as the electrode was not oxidized

to gold oxide prior to the experiment. This hypothesis was confirmed by recording two back-to-back CV experiments between 1.3 and 2.0 V at 1 mV/s with a gold working electrode in the presence of complex 2. Between both experiments, the electrode was exposed to new, unreacted complex while applying a resting potential of 1.3 V at the working electrode to prevent gold oxide reduction. Comparison of both CV experiments clearly shows that the oxidation waves I and II do not persist across experiments as long as gold oxide reduction is prevented (Fig. 4.17). Therefore the features must be related to gold oxidation processes at the electrode surface.

In the second and third scan of each OLEMS experiment with a gold working electrode, complex ${\bf 1}$ and ${\bf 2}$ both show a persistent behaviour which is comparable to what was observed in an OLEMS experiment with a PG working electrode. The current trace recorded with a gold working electrode shows a single oxidation wave, starting between 1.8 and 1.9 V while the O_2 mass trace shows oxygen evolution which correlates with the oxidative current (Fig. 4.14-4.15). The absence of any significant differences between the results of the second and third scan and the absence of CO_2 formation in both scans are again consistent with a stable catalytic system.

In contrast, the first scan of each OLEMS experiment of complex 1 or 2 with a gold working electrode gave different results for current, O₂ trace and CO₂ trace. While the difference in the current profile between the first scan of the OLEMS experiment and subsequent scans can largely be attributed to gold oxide formation processes at the working electrode, the mass traces of O₂ and CO₂ also show a different profile during the first scan compared to subsequent scans. The O₂ trace shows signs of oxygen evolution already at potentials as low as 1.6 V and the CO₂ trace shows signs of CO₂ formation from 1.8 V onward. These results might suggest that during the first scan a catalytically active species is present, giving rise to oxygen evolution starting at 1.6 V. This species might then undergo oxidative modification from 1.8 V onward, resulting in a different but stable species which is then catalytically active in the second and third scan with an onset of oxygen evolution around 1.9 V. However, as was already shown in the context of figure 4.17, exposing the electrode to new, unreacted complex between experiments does not recover the features of the first scan. While oxidative modification of the catalyst at high potentials could also explain the increasing current at 2.0 V in CV experiments between 0.0 and 2.0 V, this is

contradicted by the fact that the Fe^{II}/Fe^{III} redox couple does not appear to decrease (Fig. 4.11b and Table 4.1).

Another possible explanation for the difference between the first scan and subsequent scans of the OLEMS experiments could be the formation of minute amounts of catalytically active heterogeneous material at the electrode surface. However, EQCM experiments showed no signs of the formation of any deposit on the electrode surface. Instead, an increase in the frequency response at the gold working electrode was measured during the first scan of an EQCM experiment, recorded between 1.3 and 2.0 V at 1 mV/s in the presence of complex 1, with no further change during the subsequent scans (Fig. 4.19). This observed increase in frequency is most likely not due to an actual decrease in the mass of the electrode. In previous reports, such behaviour has been attributed to the formation of bubbles at the surface of the electrode which lower the hydrostatic pressure of the electrolyte on the surface and result in an apparent decrease in mass.^[17]

Based on the combined results of CV, OLEMS and EQCM experiments with complexes 1 and 2, it appears unlikely that the changes between scans which were observed during the electrochemical experiments of both complexes with a gold working electrode are related to the formation of either a heterogeneous species or a modified homogeneous species from either complex. Instead all evidence points to the conclusion that all differences that are observed between scans are related to gold oxide formation and reduction processes at the electrode surface.

Complex **3** which was also studied using a PG working electrode showed the same qualitative oxygen evolution behaviour in an OLEMS experiment in a $0.1 \, \text{M} \, \text{Na}_2 \text{SO}_4$ electrolyte solution that was previously observed for complex **1** in a $0.1 \, \text{M} \, \text{NaClO}_4$ electrolyte solution with a PG electrode. This result shows that — as expected — the oxidation state of the starting material does not influence the observed catalytic activity.

Despite the similarities in the electrochemistry of complexes **1-3**, complex **3** also showed clear differences from both other complexes. While complexes **1** and **2** only showed a single reversible Fe^{II}/Fe^{III} redox couple in a 0.1 M NaClO₄ electrolyte solution, complex **3** shows one reversible redox couple at 0.7 V and an irreversible oxidation wave between 1.0 and 1.2 V in a 0.1 M Na₂SO₄ electrolyte solution. The presence of two oxidation waves clearly indicates that a mixture of species is present in solutions of complex **3**. The addition of chloride to the electrolyte

solution containing complex **3** did not elicit any changes in the voltammogram, indicating that presence of two species is not related to coordination of chloride ions. Another possible explanation could be the *in situ* formation of other species upon dissolution such as a μ -OH bridged dimer.

The results of an OLEMS experiment with complex $\bf 3$ in a 0.1 M Na₂SO₄ electrolyte solution reveal the same behaviour that was also found for the combination of complex $\bf 1$ with a PG working electrode in a 0.1 M NaClO₄ electrolyte solution (Fig. 4.23). An OLEMS experiment of complex $\bf 3$ in a 0.1 M H₂SO₄ electrolyte solution on the other hand gave results which appear to be qualitatively similar but quantitatively different from the results observed in a 0.1 M Na₂SO₄ electrolyte solution. However, these quantitative differences need to be interpreted carefully. The response in the mass traces will inevitably differ between experiments. This is due to the variability in the distance between the OLEMS tip and the working electrode on one hand and the inherent differences between two different OLEMS tips on the other hand. While the current that was recorded in both OLEMS experiments also strongly suggests a quantitative difference between both measurements, this difference in oxidative current is expected to be at least partially due to increased rates of CO₂ formation from the electrode material at acidic pH. $^{[19-20]}$

4.4 Conclusions

The electrochemical behaviour of the α -Fe(bpmcn) complexes, which is described in this chapter, turned out to be substantially more complex than anticipated. All three complexes showed a comparable and persistent onset of oxygen evolution at around 1.8 V in OLEMS experiments with a PG working electrode. In contrast, the results of electrochemical experiments of complexes 1 and 2 with a gold working electrode depend strongly on the exact conditions. Considerable changes over time were observed during prolonged potential cycling between 0.0 and 2.0 V as well as going from the 1st to the 2nd scan of an OLEMS experiment. While all evidence suggests that these differences which evolve over time are related to gold oxide formation processes at the surface of the working electrode, the exact underlying mechanism remains unclear.

Even though catalytic water oxidation activity was found for all complexes examined in this chapter, the recorded onset potential of ~1.8 V is not outstanding compared to the other iron-based homogeneous water oxidation complexes reported in this thesis. This result is in direct contrast to the status of

the system as a benchmark catalyst when driven by chemical oxidants. Furthermore, complex **2** had previously been found to be 4-5 times more stable under Cerium(IV) conditions compared to complex **1** but no such major differences between the two complexes were found in electrochemical experiments. Instead, complexes **1** and **2** were found to behave virtually identically in all experiments, showing that other factors dominate in the electrocatalytical regime compared to catalysis driven by chemical oxidants.

Overall, the findings of this chapter highlight the importance of electrochemical studies for evaluating (potential) water oxidation catalysts as the results obtained in the presence of chemical oxidants cannot be reliably translated to electrochemistry. The results also show that the observed electrochemistry can vary significantly between two different electrode materials in the presence of the same catalyst.

4.5 Experimental

4.5.1 General

Complexes **1-3** were synthesized and characterized in the group of Miquel Costas at the University of Girona. The complexes were used as received.

Complexes **1** and **2** were stored under argon in a glovebox to prevent oxidation in air.

4.5.2 Electrochemical experiments

All electrochemical measurements with the exception of the EQCM experiments (details below) were performed in a custom made single-compartment glass cell on Ivium potentiostats, operated by IviumSoft software, using a three-electrode setup. The working electrodes were a pyrolytic graphite (PG) disc with a (geometric) surface area of $0.20~\rm cm^2$ and a gold disc with a (geometric) surface area of $0.13~\rm cm^2$. For the experiments with an ITO working electrode, a small slice of ITO covered glass (ca. $0.5x1.5~\rm cm$) was used. While the gold and PG working electrodes were used in hanging meniscus configuration, the ITO electrode was partially submerged in the electrolyte solution. A large surface area gold plate was used as a counter electrode. The reference electrode was a reversible hydrogen electrode (RHE) made up of a platinum mesh in H_2 -saturated electrolyte at the same pH as the working solution. The cell and the reference electrode were connected via a Luggin capillary. A fresh PG surface was prepared before each

experiment by polishing the working electrode with sandpaper and subsequent removal of excess debris by sonication in Milli-Q water for at least 5 minutes.

The gold electrode was prepared before each experiment by oxidizing the surface at 10 V for 30 s in a 10% H_2SO_4 solution, followed by stripping of the gold oxide layer in a 6 M HCl solution and subsequent electro-polishing of the electrode by scanning for 200 cycles between 0.0 and 1.75 V vs. RHE at 1000 mV/s in a 0.1 M $HClO_4$ electrolyte solution.

All glassware used in electrochemical measurements was routinely cleaned of any organic contamination by boiling in 3:1 mixture of concentrated sulfuric and nitric acid. Prior to each experiment the glassware was cleaned by threefold rinsing and boiling in Milli-Q water. The electrolyte solutions were prepared from p.a. grade chemicals obtained from Merck (Suprapur®) and Milli-Q water.

Prior to measurements, the electrolyte solution was purged of air by bubbling with argon (Linde, Ar 6.0) for at least 20 minutes. During the measurements, the cell was constantly kept under argon flow to prevent air from entering.

For the OLEMS measurements, the gasses formed at the working electrode were collected via a hydrophobic tip (KEL-F with a porous Teflon plug) in close proximity to the surface of the working electrode and analyzed in a QMS 200 mass spectrometer. A detailed description of the OLEMS setup is available elsewhere. [8] All electrochemical potential cycling in combination with OLEMS was done at a scan rate of 1 mV/s. For the mass spectrometry data recorded via OLEMS during cylic voltammetry measurements, background correction was done by assuming an exponential decay fit (concerns Figures 4.13, 4.14, 4.15, 4.16, 4.18, 4.23 and 4.24).

EQCM experiments were performed in a 3 mL Teflon cell purchased from Autolab. The top part of the cell was modified to allow for electrochemical measurements under an inert atmosphere. For further details, see appendix B (Fig. B.9). The EQCM was controlled by an Autolab potentiostat operated by NOVA 2.0 software. Autolab EQCM electrodes with a surface area of 1.5 cm² consisting of a 200 nm gold layer deposited on a quartz crystal were used as working electrodes. A custom made RHE reference electrode was used which is described elsewhere. [9]

4.5.3 Sample preparation

Samples of complexes 1 and 2 were weighed in an argon atmosphere inside the glovebox and stored in a closed vessel. Prior to the experiment, the complexes were dissolved in a small amount of electrolyte solution (typically 1-2 mL) taken

from the cell which had previously been purged with argon and subsequently added to the electrochemical cell. The electrolyte solution was then purged again by bubbling with argon for several minutes.

Samples of complex **3** were weighed in air and subsequently added to the cell in a manner analogous to that described for complexes **1** and **2**.

For all electrochemical experiments a 1.1 mM concentration of catalyst was used unless stated otherwise.

4.6 Supporting Info

The following supplementary information can be found in Appendix C: A depiction of the flocculent white precipitate formed as a result of the decomposition of complex $\bf 1$ at pH $\bf 1$ inside the electrochemical cell (Fig. C.1), an illustration of the artefacts routinely found in the m/z signals during OLEMS measurements (Fig. C.2 and Fig. C.3) and a voltammogram of complex $\bf 3$ recorded with an ITO working electrode (Fig. C4).

4.7 References

- [1] J. L. Fillol; Z. Codola; I. Garcia-Bosch; L. Gomez; J. J. Pla; M. Costas, *Nat. Chem.* **2011**, *3*, 807-813.
- [2] T. J. Collins, Acc. Chem. Res. 1994, 27, 279-285.
- [3] W. C. Ellis; N. D. McDaniel; S. Bernhard; T. J. Collins, *J. Am. Chem. Soc.* **2010**, *132*, 10990-10991.
- [4] M. Costas; J. L. Fillol, Personal communication, 2017.
- [5] S. L. Esarey; J. C. Holland; B. M. Bartlett, *Inorg. Chem.* **2016**, *55*, 11040-11049.
- [6] D. Hong; S. Mandal; Y. Yamada; Y. M. Lee; W. Nam; A. Llobet; S. Fukuzumi, *Inorg. Chem.* **2013**, *52*, 9522-9531.
- [7] O. Diaz-Morales; T. J. Hersbach; D. G. H. Hetterscheid; J. N. Reek; M. T. M. Koper, *J. Am. Chem. Soc.* **2014**, *136*, 10432-10439.
- [8] A. H. Wonders; T. H. M. Housmans; V. Rosca; M. T. M. Koper, *J. Appl. Electrochem.* **2006**, *36*, 1215-1221.
- [9] P. Abril; M. P. del Río; C. Tejel; T. W. G. M. Verhoeven; J. W. H. Niemantsverdriet; C. J. M. Van der Ham; K. G. Kottrup; D. G. H. Hetterscheid, *ACS Catal.* **2016**, *6*, 7872-7875.
- [10] S. Fukuzumi; D. Hong, Eur. J. Inorg. Chem. 2014, 2014, 645-659.
- [11] U. Hintermair; S. W. Sheehan; A. R. Parent; D. H. Ess; D. T. Richens; P. H. Vaccaro; G. W. Brudvig; R. H. Crabtree, *J. Am. Chem. Soc.* **2013**, *135*, 10837-10851.
- [12] B. Limburg; E. Bouwman; S. Bonnet, Coord. Chem. Rev. 2012, 256, 1451-1467.
- [13] G. Chen; L. Chen; S. M. Ng; W. L. Man; T. C. Lau, *Angew. Chem., Int. Ed.* **2013**, *52*, 1789-1791.

- [14] Y. Lin; S. Zhou; S. W. Sheehan; D. Wang, *J. Am. Chem. Soc.* **2011**, *133*, 2398-2401.
- [15] M. T. Mayer; C. Du; D. Wang, J. Am. Chem. Soc. 2012, 134, 12406-12409.
- [16] K. M. H. Young; B. M. Klahr; O. Zandi; T. W. Hamann, *Catal. Sci. Technol.* **2013**, *3*, 1660.
- [17] N. D. Schley; J. D. Blakemore; N. K. Subbaiyan; C. D. Incarvito; F. D'Souza; R. H. Crabtree; G. W. Brudvig, *J. Am. Chem. Soc.* **2011**, *133*, 10473-10481.
- [18] C. J. M. van der Ham; F. Işık; T. W. G. M. Verhoeven; J. W. Niemantsverdriet; D. G. H. Hetterscheid, *Catal. Today* **2017**, *290*, 33-38.
- [19] K. G. Gallagher; T. F. Fuller, Phys. Chem. Chem. Phys. 2009, 11, 11557-11567.
- [20] Y. Yi; G. Weinberg; M. Prenzel; M. Greiner; S. Heumann; S. Becker; R. Schlögl, *Catal. Today* **2017**, *295*, 32-40.

Interactions between metal complexes and the electrode surface – the influence of dissolved metal complexes on the surface of gold and graphitic carbon electrodes

In this chapter, the influence of interactions between dissolved metal complexes and the surface of working electrodes made from gold and pyrolytic graphite (PG) is investigated with respect to the consequences for the electrode material. For a PG electrode, the presence of iron complexes in solution appears to facilitate the formation of CO_2 from the electrode material already at lower potentials than in blank experiments in the absence of metal complexes.

For a gold electrode, performing cyclic voltammetry in the presence of either $[(MeOH)Fe(Hbbpya)-\mu-O-(Hbbpya)Fe(MeOH)](OTf)_4$ (1) (with Hbbpya = N,N-bis(2,2'-bipyrid-6-yl)amine) or $[Ru(tpy)(bpy)(H_2O)](OTf)_2$ (2) (with bpy = bipyridine and tpy = terpyridine) results in clear changes to the voltammogram of the gold background. These changes were found to be reversible over several scans in a subsequent cyclic voltammetry experiment with a blank electrolyte solution. The nature of these changes is not yet understood and the mechanism of the processes behind them requires further investigation.

For both electrode materials, the effects of the presence of dissolved metal complexes are potentially highly significant, in particular for attempts at benchmarking catalysts. Therefore the interactions between the electrode surface and complexes in solution should be considered carefully in electrocatalytic applications.

5.1 Introduction

Choosing the right electrode material can be a crucial aspect of setting up an electrochemical experiment. In the context of electrocatalytic water oxidation, electrodes made from carbon-based materials such as pyrolytic graphite (PG) and glassy carbon (GC) are particularly attractive because they feature a flat background across a wide potential window. However, the downside of working with carbon-based materials is their propensity for CO₂ formation at higher potentials. Since CO₂ formation is a useful indicator for catalyst decomposition in the case of metal complexes bearing organic ligands, CO₂ formation from the electrode material can obscure such processes.

Another commonly used electrode material besides carbon is gold. Gold does not produce CO₂ and therefore allows to track CO₂ formation from ligand decomposition. However, gold does undergo gold oxide formation and reduction reactions which result in a considerably more complex background voltammogram compared to PG and GC. In particular polycrystalline gold electrodes show a multitude of redox events in cyclic voltammetry (CV) experiments due to the presence of several different structural features on the electrode surface. Furthermore, gold itself catalyzes the water oxidation reaction with an onset at about 2.0 V vs. a reversible hydrogen electrode (RHE). [5-6]

Other non-metallic electrode materials such as indium tin oxide (ITO), fluorine-doped tin oxide (FTO) or boron-doped diamond (BDD) are also inert over wide potential ranges. However, due to their nature as semi-conductors, they exhibit a low density of states at the Fermi level which can influence electron-transfer kinetics between the electrode and the catalyst. As a result, ITO and BDD electrodes proved to be unsuitable for studying the water oxidation catalysts discussed in this thesis (cf. Fig. B.7, Appendix B and Fig. C.4, Appendix C).

The results discussed in chapter 3 and 4 show that interactions between the catalyst and the surface of a particular electrode material can significantly influence the electrochemical behaviour of the catalyst. On the other hand, the interactions between the catalyst and the electrode may also have consequences for the surface of the electrode in return. Evidence for this is also briefly discussed in chapters 3 and 4 of this thesis. The results presented in chapter 3 suggest that most of the considerable CO₂ formation that is observed throughout all OLEMS experiments with PG working electrodes, that are described in this thesis, originates from decomposition of the electrode material. The results presented in chapter 4 show an increase in the peak current at 2.0 V vs. RHE between

subsequent scans during CV experiments of α -[Fe(bpmcn)(OTf)₂] (with bpmcn = N,N'-dimethyl-N,N'-bis(2-pyridylmethyl)-cyclohexane-1,2-diamine) in combination with a gold working electrode. This increase in current was found to be most likely due to changes of the structure of the electrode surface. Other possible explanations such as modifications of the complex in solution or deposition of solids on the electrode surface could be ruled out through control experiments. However, the nature of the changes at the gold surface remains unclear.

To the best of our knowledge, the influence of the presence of metal complexes in solution on the surface of the working electrode has so far been largely overlooked in literature on electrocatalytic water oxidation despite the potentially important implications for the field. Therefore, in this chapter, we explore the effects of the presence of metal complexes in solution on the two electrode materials gold and PG. For the case of a PG working electrode we compare the onset of CO₂ formation in OLEMS experiments, both in the absence and presence of metal complexes in solution. For the case of a gold working electrode we compare voltammograms of the gold background before and after performing cyclic voltammetry in the presence of metal complexes in solution.

5.2 Results and Discussion

5.2.1 Electrochemistry of carbon

Before investigating the behaviour of any electrode material in the presence of metal complexes, it is important to first establish the behaviour of the electrode material by itself, in the absence of any complex in solution.

A review about electrode materials for studying electrocatalysts, published in 2014, described carbon-based materials such as GC and highly ordered pyrolytic graphite (HOPG) as being inert across a large potential range. ^[1] In acidic and neutral electrolyte solutions, the respective usable anodic potential range was reportedly limited by the onset of oxygen evolution around 1.8 V vs. RHE in 0.1 M H_2SO_4 and around 2.0 V vs. RHE in 0.1 M NaOAc.

In contrast to that, we find that no oxygen evolution occurs at a PG working electrode in the absence of any additional catalyst in both 0.1 M $HClO_4$ (Fig. 5.1) and 0.1 M Na_2SO_4 (Fig. 5.2) electrolyte solution even at potentials well above 2.0 V. Instead, only CO_2 formation can be seen in on-line electrochemical mass spectrometry (OLEMS) experiments. Figures 5.1 and 5.2 show the corresponding mass traces of CO_2 and O_2 recorded during chronoamperometry experiments with

a PG working electrode at 1.9, 2.0 and 2.2 V in a 0.1 M $HClO_4$ electrolyte solution and a 0.1 M Na_2SO_4 electrolyte solution respectively. Based on the recorded current and the ion current in the m/z=44 trace, the rate of CO_2 formation appears to be substantially higher in acidic solution compared to neutral unbuffered electrolyte solutions. This finding is in line with the work of Schlögl and co-workers who reported that GC electrodes are oxidized faster in acidic environments than in neutral environments.^[7]

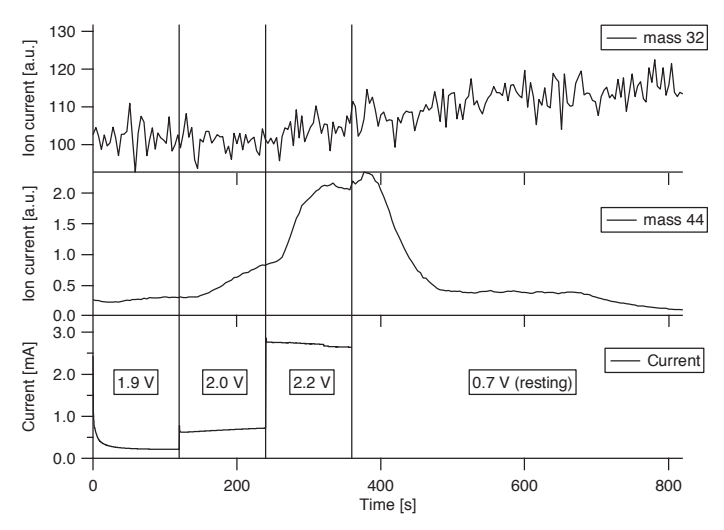


Figure 5.1: Results of an OLEMS measurement of a PG working electrode during chronoamperometry in a 0.1 M $HClO_4$ solution. Shown are the current (bottom), the m/z trace for CO_2 (middle) and m/z trace for O_2 (top) while applying different potentials for 120 seconds each. The potentials that were applied are: 1.9 V vs. RHE (0-120 s), 2.0 V vs. RHE (120-240 s) and 2.2 V vs. RHE (240-360 s). After 360 s the potential was switched to a resting potential of 0.7 V vs. RHE. The vertical lines indicate the points in time when the potential was switched.

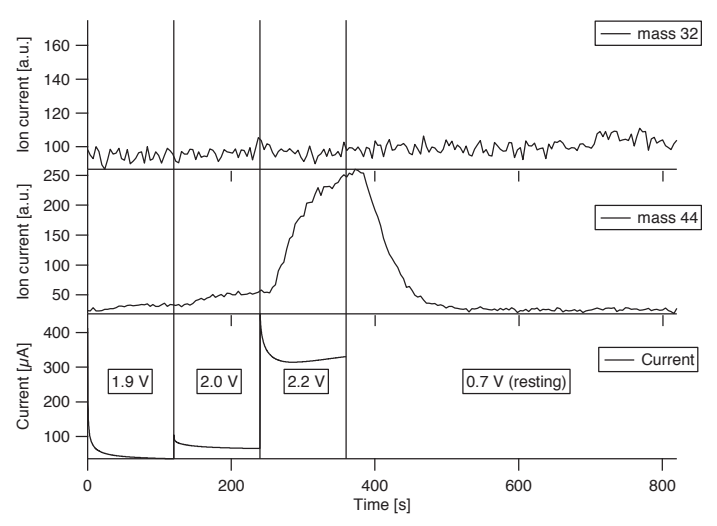


Figure 5.2: Results of an OLEMS measurement of a PG working electrode during chronoamperometry in a $0.1 \text{ M Na}_2\text{SO}_4$ solution. Shown are the current (bottom), the m/z trace for CO_2 (middle) and m/z trace for O_2 (top) while applying different potentials for 120 seconds each. The potentials that were applied are: 1.9 V vs. RHE (0-120 s), 2.0 V vs. RHE (120-240 s) and 2.2 V vs. RHE (240-360 s). After 360 s the potential was switched to a resting potential of 0.7 V vs. RHE. The vertical lines indicate the points in time when the potential was switched.

To determine the onset of CO_2 formation, cyclic voltammetry was performed in combination with OLEMS. Figure 5.3a shows the result of an OLEMS experiment while cycling the potential between 1.3 and 2.0 V at 1 mV/s in a blank 0.1 M Na_2SO_4 electrolyte solution. From the corresponding CO_2 mass trace an onset of CO_2 formation at about 1.9 V can be determined. In comparison to that, an earlier onset of CO_2 formation is observed when a metal complex is present in the electrolyte solution (Fig. 5.3b). In the presence of 1 mM $Fe(OTf)_2$ the OLEMS shows an onset for CO_2 formation at about 1.6 V. Similarly, all OLEMS experiments performed in combination with a PG working electrode in the presence of a metal complex, that are discussed throughout this thesis, show an onset of CO_2 evolution at potentials significantly below 1.9 V. In chapter 2, all three cyclambased complexes showed CO_2 formation during OLEMS experiments in both unbuffered and phosphate-buffered electrolyte media (Fig. 2.6, 2.11, 2.12, chapter 2) with onset potentials of CO_2 formation as low as 1.2 V for [Fe(cyclamacetate)CI] and 1.4 V for $Cis-[Fe(cyclam)CI]CI_2$ (Fig. 2.6, chapter 2).

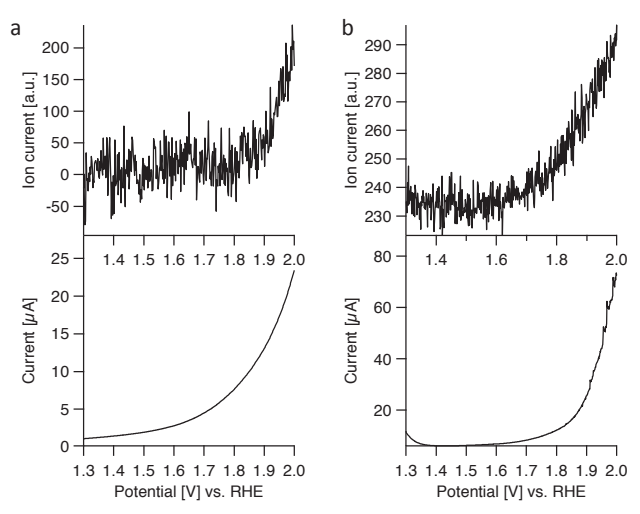


Figure 5.3: (a) Results of an OLEMS measurement with a PG working electrode during cyclic voltammetry in a blank 0.1 M NaClO_4 solution. Shown are the mass trace of m/z = 44 (top) and the current (bottom). (b) Results of an OLEMS measurement with a PG working electrode during cyclic voltammetry in a 0.1 M NaClO_4 solution in the presence of $1 \text{ mM Fe}(\text{OTf})_2$. Shown are the mass trace of m/z = 44 (top) and the current (bottom). For the sake of clarity, only the forward scan of each measurement is depicted.

The Fe(Hbbpya) complex (Hbbpya = N,N-bis(2,2'-bipyrid-6-yl)amine), which is described in chapter 3, showed negligible CO_2 formation with a gold working electrode (Fig. 3.4, chapter 3) but substantial CO_2 formation starting at 1.6 V in combination with a PG working electrode (Fig. 3.6, chapter 3). Similarly, the Fe(bpmcn) complexes (bpmcn = N,N'-dimethyl-N,N'-bis(2-pyridylmethyl)-cyclohexane-1,2-diamine) discussed in chapter 4 also showed CO_2 formation starting at 1.5 V in combination with a PG working electrode (Fig 4.13, chapter 4) while little to no CO_2 formation was observed in combination with a gold working electrode (Fig. 4.14-4.16, chapter 4).

For most metal complexes it is difficult to pinpoint the source of the CO_2 as it might originate from decomposition of the ligand, decomposition of the electrode or both. However, in the case of $Fe(OTf)_2$ any CO_2 that is being observed in OLEMS measurements (Fig. 5.3b) must almost certainly originate from the electrode material as the only other source of carbon, which is present in the system, is the redox inert triflate ion. This demonstrates that high-valent metal oxo-species have the ability to catalyze the oxidation of carbon electrodes. As a result the performance of a water oxidation catalyst in combination with a carbon-based working electrode can be impacted negatively since part of the available catalyst does not complete the catalytic cycle towards oxygen evolution. Instead, part of

the catalyst undergoes side reactions, resulting in a lower faradaic efficiency and lower turnover frequency.

For any complex that is capable of catalyzing the water oxidation reaction, the capability to oxidize other substrates as well is certainly not unexpected as water is one of the most difficult to oxidize substrates. Therefore it seems plausible that the oxidation of substrates such as the carbon electrode itself can occur already at potentials below the onset of water oxidation. Accordingly, for all iron complexes discussed in this thesis, the onset of oxygen evolution was found to lie several hundred millivolts above the onset of CO_2 formation when using a PG working electrode. The only exception is the Fe(Hbbpya) complex described in chapter 3 for which the onsets of O_2 evolution and CO_2 formation coincide around 1.6 V in experiments with a PG working electrode. As a result, routine methods to determine catalyst kinetics such as the foot-of-the-wave (FOTW) analysis cannot always be applied without reservations.

The FOTW method is used to determine a catalyst's maximum turnover frequency by extrapolating from measurements performed near the onset of the catalytic wave. Figure 5.4 shows a schematic representation of an ideal sigmoidal shaped catalytic current wave. The area highlighted in green in figure 5.4 shows the current region in which the current plateaus because the maximum turnover frequency of the catalyst is reached. In this region, the turnover frequency is no longer limited by electron-transfer rates but solely by the kinetics of the rate-limiting step of the catalytic cycle. Therefore, increasing the potential further does not result in higher currents.

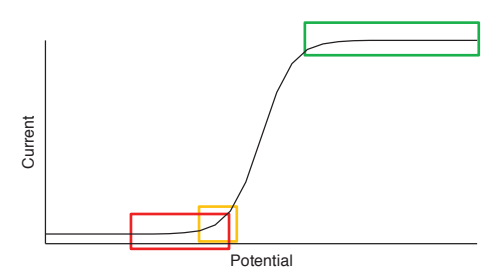


Figure 5.4: Schematic representation of an ideal sigmoidal catalytic current wave on which three different regions are highlighted: region in which current from CO_2 formation may dominate over current from water oxidation (red); region in which foot-of-the-wave analysis is performed (yellow); region in which the reaction rate is no longer limited by electron-transfer rates but by the kinetics of the catalytic reaction (green).

The resulting sigmoidal shape shown in figure 5.4 represents an ideal case in which no other factors limit the turnover frequency of the catalyst. In real electrocatalytical studies, unwanted side-effects such as substrate consumption, catalyst decomposition or product inhibition can become rate limiting and obscure the intrinsic properties of the catalyst. [9]

By using the FOTW method one seeks to calculate the theoretical maximum turnover frequency at the plateau of the sigmoidal current wave (Fig. 5.4 area highlighted in green) while avoiding the aforementioned side-effects present in real systems by focusing on the area around the onset of the catalytic wave where those effects are still negligible (Fig. 5.4, area highlighted in yellow). The results of the OLEMS experiments presented in this thesis show, however, that one also needs to rule out CO_2 formation from the electrode as a side reaction when one is working with carbon-based electrodes as CO_2 formation can contribute significantly to the current near the onset of water oxidation (Fig. 5.4, area highlighted in red).

5.2.2 Electrochemistry of gold

5.2.2a Introduction

In contrast to carbon-based electrodes, working electrodes made from gold are capable of catalyzing the water oxidation reaction even in the absence of an additional catalyst. The onset for water oxidation by a gold electrode without any additional catalyst was determined to lie at about 2 V vs. RHE under both acidic and neutral electrolyte conditions. ^[5-6] This limits the use of gold as an electrode material for studying water oxidation catalysts to potentials below 2 V. Aside from being able to catalyze water oxidation, gold electrodes also show a complex pattern of background redox processes associated with the formation and reduction of gold oxide ^[10-12] which can complicate voltammetry measurements of complexes in solution.

While structural changes at the surface of gold electrodes induced by external factors have been studied in material sciences, to the best of our knowledge, no literature currently discusses the possible consequences for electrocatalysis. Therefore, in this chapter, we discuss the effects of dissolved metal complexes on the surface of a gold working electrode and the possible implications in the context of electrocatalytic water oxidation. The effects are investigated using cyclic voltammetry measurements and comparing the observed redox features of

the background voltammogram of a gold working electrode before and after cyclic voltammetry experiments in the presence of dissolved metal complexes.

5.2.2b Blank experiments in acidic and neutral unbuffered electrolyte media In order to assess the influences of dissolved metal complexes on the surface of a gold working electrode, it is necessary to first determine the baseline background voltammogram of a clean gold working electrode in blank electrolyte solutions in the absence of any metal complex. Background voltammograms of a gold electrode were therefore recorded in both acidic and neutral unbuffered electrolyte solutions.

At pH 1 (0.1 M HClO₄) and in the absence of any metal complex, a gold electrode shows several redox events in a cyclic voltammetry experiment which are related to the formation and the reduction of gold oxide (Fig. 5.5a). This observed profile is in agreement with literature. [10-12] The current profile of the forward scan of the voltammogram consists of an onset of oxidative current at about 1.3 V with a relatively sharp peak that has been attributed to the formation of hydroxylspecies on the surface of the electrode, followed by a broader peak which completes the oxidation of the electrode surface from gold to gold oxide. [10-11] In the backward scan, the reduction of gold oxide takes the shape of a sharp peak at about 1.1 V followed by a shoulder at 1.0 V. The sharp peak has been attributed to the reduction of metal oxo-species at the electrode surface while the shoulder represents the reduction of a sublattice of hydroxyl-species in between adsorbed anions. [10-11] The presence of several peaks for both gold oxide formation and gold oxide reduction is also observed for single crystal electrodes. [13] As such, it is not a feature associated with different faces on the electrode surface but rather an inherent feature of gold as a substrate. [10-11]

While there is a wealth of information about the behaviour of gold electrodes in acidic and alkaline electrolyte solutions, [13-21] comparatively little information is available about the behaviour of gold electrodes in neutral unbuffered electrolyte solutions. [12, 22-23]

CV experiments with a gold working electrode in a neutral unbuffered electrolyte solution of 0.1 M NaClO₄ reveal a different shape of the current profile (Fig. 5.5b). While the formation of gold oxide is again represented by a sharp peak followed by a broader peak, the reduction of gold oxide now consists of two strictly separate peaks about 500 mV apart at 1.2 and 0.7 V respectively. This shape is once again in agreement with previous reports.^[12] The separation between the

two gold oxide reduction peaks has previously been attributed to local pH changes in an unbuffered solution. [13, 18]

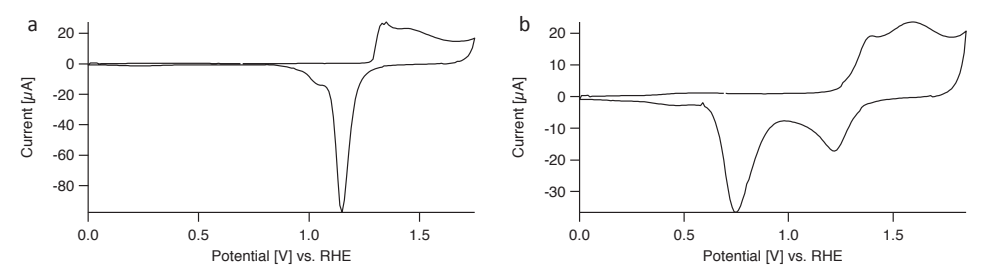


Figure 5.5: (a) Results of a CV measurement with a gold working electrode in a 0.1 M HClO₄ electrolyte solution, recorded between 0.0 and 1.75 V vs. RHE at 100 mV/s, starting at 0.7 V vs. RHE (b) Results of a CV measurement with a gold working electrode in a 0.1 M NaClO₄ electrolyte solution, recorded between 0.0 and 1.85 V vs. RHE at 100 mV/s, starting at 0.7 V vs. RHE.

5.2.2c Metal complex induced changes to the surface of a gold working electrode In chapter 3 of this thesis, CV experiments are described with a gold working electrode in combination with 0.5 $\mathsf{m}\mathsf{M}$ [(MeOH)Fe(Hbbpya)–μ-O– (Hbbpya)Fe(MeOH)](OTf)₄ (1) (with Hbbpya = N,N-bis(2,2'-bipyrid-6-yl)amine) present in the electrolyte solution. In the corresponding voltammograms, recorded in the presence of complex 1, the current in the potential region between 1.3 and 1.9 V, which corresponds to the formation of gold oxide, follows a different profile compared to the blank experiment (compare Fig. 5.5b and Fig. 3.2d, chapter 3). In the presence of complex 1, two broad oxidation waves are observed in the region between 1.3 and 1.9 V. In the backward scan only a single reduction peak at 1.2 V is visible. The results discussed in chapter 3 already demonstrate that this difference in oxidative current in the 1.3 to 1.9 V potential region between the presence and the absence of complex 1 is indeed related to gold oxide formation processes and not redox reactions of complex 1 itself (cf. Fig. 3.4, chapter 3).

This difference between the presence and absence of complex ${\bf 1}$ in solution indicates that complex ${\bf 1}$ interacts with the gold electrode in a way that influences the mechanism of gold oxide formation and gold oxide reduction. Therefore, in this chapter, the influence of metal complexes, that are present in solution, on the processes at the electrode surface is discussed. This is done by comparing the background voltammograms of a gold electrode, recorded in blank Na₂SO₄ electrolyte solutions, before and after CV experiments in the presence of complex ${\bf 1}$. Additionally, identical CV experiments were also performed in the presence of

0.5 mM [Ru(tpy)(bpy)(H_2O)](OTf)₂ (2) (with bpy = bipyridine and tpy = terpyridine) instead of complex 1, to determine whether the observed effects are unique for complex 1 or whether other complexes exhibit a similar influence on the gold electrode. Since both complexes dissolve poorly in perchlorate containing electrolyte solutions, Na_2SO_4 was chosen instead as the appropriate electrolyte for all experiments with either complex.

In CV experiments with a gold working electrode, changes in the resulting voltammogram are observed upon addition of complex 1 to the electrolyte solution (Fig. 5.6). First, the potential is cycled between 1.3 and 2.0 V at 10 mV/s for five cycles with a gold working electrode in a Na₂SO₄ electrolyte solution without any metal complex present. The first scan of the resulting voltammogram shows oxidative current, associated with the formation of gold oxide, which is absent in subsequent scans (Fig. 5.6a). To demonstrate the effects of the presence of complex 1 in solution, the complex was then added to the solution, followed by another CV experiment between 1.3 and 2.0 V while keeping the resting potential at 1.3 V in between both experiments to avoid the reduction of gold oxide. The resulting voltammogram after the addition of complex 1 shows again additional oxidative current during the first scan which is absent in subsequent scans (Fig. 5.6b), despite the fact that the electrode surface had already been fully oxidized to gold oxide during the previous CV experiment shown in figure 5.6a.

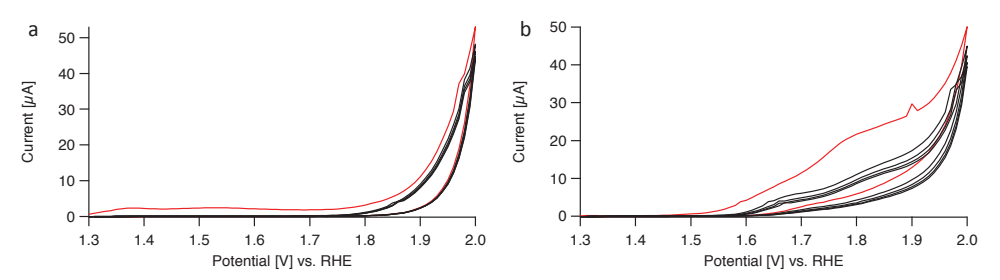


Figure 5.6: (a) Results of a CV measurement with a gold working electrode in a 0.125 M Na_2SO_4 electrolyte solution, recorded between 1.3 and 2.0 V vs. RHE at 10 mV/s, starting at 1.3 V vs. RHE. The first scan is depicted in red, subsequent scans in black. (b) Results of a CV measurement with a gold working electrode in the presence of 0.5 mM complex **1** in a 0.1 M Na_2SO_4 electrolyte solution, recorded between 1.3 and 2.0 V vs. RHE at 10 mV/s, starting at 1.3 V vs. RHE. The first scan is depicted in red, subsequent scans in black. The working electrode was pre-treated before the experiment by oxidation of the electrode surface to gold oxide by cycling five times between 1.3 and 2.0 V vs. RHE at 10 mV/s as is shown in Fig. 5.6a.

After five cycles between 1.3 and 2.0 V at 10 mV/s in the presence of complex 1, the electrode was taken out of the electrolyte solution containing complex 1, rinsed with Milli-Q water and placed in a fresh blank electrolyte solution of Na_2SO_4

while again applying a resting potential of 1.3 V to avoid the reduction of gold oxide. In a subsequent CV experiment, the potential was cycled between 0.0 and 2.0 V for three cycles with a starting potential of 1.3 V (Fig. 5.7a). The resulting voltammogram shows a clear difference between the first scan and the following two scans. In the first scan of the CV experiment, the first gold oxide reduction peak at 1.2 V (hereafter called peak I) is almost entirely absent and the second reduction peak at 0.7 V (hereafter called peak II) is clearly visible. In the second and third scan of the CV experiment, peak I is more prominent again while peak II is no longer visible. After recording these three scans, the electrode was left in contact with the electrolyte solution at a resting potential of 0.7 V for 30 minutes followed by another CV experiment between 1.3 and 2.0 V for 100 cycles, starting each cycle at 0.7 V. During the repeated scanning between 0.0 and 2.0 V, peak II slowly reappears over time (Fig. 5.7b). Additionally, the first shoulder of the gold oxide formation region at about 1.3 V also grows over time during repeated potential cycling.

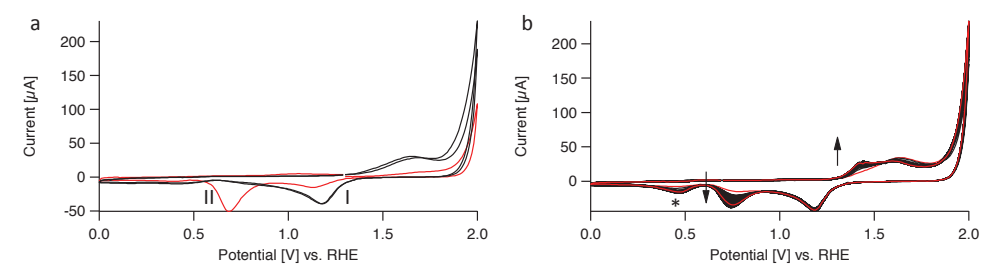


Figure 5.7: (a) Results of a CV measurement with a gold working electrode, recorded between 0.0 and 2.0 V vs. RHE in a 0.1 M Na_2SO_4 electrolyte solution, scanning at 100 mV/s, starting at 1.3 V vs. RHE. The potential was cycled three times between 0.0 and 2.0 V vs. RHE. The first scan is depicted in red, both subsequent scans in black. This CV experiment was performed after cycling the potential five times between 1.3 and 2.0 V vs. RHE at 10 mV/s in the presence of 0.5 mM complex 1 in a 0.1 M Na_2SO_4 electrolyte solution, the results of which is shown in fig. 5.6b, and subsequent rinsing of the working electrode with Milli-Q water. A resting potential of 1.3 V vs. RHE was applied before the start of the experiment to avoid premature gold oxide reduction. (b) Voltammogram of a gold working electrode after resting at 0.7 V vs. RHE for 30 min in a 0.125 M Na_2SO_4 electrolyte solution, following the experiment described under fig. 5.7a. The first and last scan are depicted in red while the intermediate scans are depicted in black. Conditions: 100 scans between 0.0 and 2.0 V vs. RHE at 100 mV/s, starting at 0.7 V vs. RHE. The arrows in the figure indicate changes in the current profile between subsequent scans. The small peak growing out at 0.5 V (indicated in the figure by an *) is due to reduction of small amounts of dioxygen formed at 2.0 V.

The fact that the reappearance of peak II only takes place during the repeated cycling and not during the 30 minute resting-period at 0.7 V means that the changes in the structure of the gold surface, which have been induced by the

presence of complex **1**, remain stable for at least 30 minutes at ambient conditions. This shows that the atoms at the surface of the gold electrode are not sufficiently mobile at room temperature and that cycling over the gold oxidation and gold oxide reduction region is crucial to achieve regeneration of the original surface structure.

To detect any influence of the pH of the electrolyte medium and to eliminate the possible influence of local pH changes at the working electrode, the same experimental procedure was repeated with a HClO₄ electrolyte solution instead of a Na₂SO₄ electrolyte solution for the initial and the final CV experiment in the absence of complex 1. The CV experiment in the presence of complex 1 was performed in a 0.1 M Na₂SO₄ electrolyte solution as before. Accordingly, the gold working electrode was first oxidized in a blank 0.1 M HClO₄ electrolyte solution by cycling the potential five times between 1.3 and 2.0 V at 10 mV/s. The electrode was then rinsed and transferred to a different cell containing 0.5 mM complex 1 in a 0.1 M Na₂SO₄ electrolyte solution. In this solution another a CV measurement was then performed, consisting of five cycles between 1.3 and 2.0 V at 10 mV/s. After subsequent rinsing of the electrode a final CV experiment was recorded, consisting of 100 scans between 0.0 and 2.0 V at 100 mV/s in a 0.1 M HClO₄ electrolyte solution in the absence of complex 1, starting each scan at 1.3 V. Throughout the entire procedure, the resting potential at the working electrode was kept at 1.3 V to avoid the reduction of gold oxide between measurements. The results of the final CV experiment in a 0.1 M HClO₄ electrolyte solution are summarized in figure 5.8.

The initial blank measurement of a gold background in a 0.1 M HClO₄ electrolyte solution before exposure complex **1** (Fig. 5.5a) showed a sharp reduction peak for gold oxide reduction at 1.1 V with a shoulder at 1.0 V. In contrast, in the first scan of the CV experiment depicted in figure 5.8, the first gold oxide reduction peak at 1.1 V is absent while the second peak at 1.0 V is strongly pronounced. In subsequent scans, the first peak is clearly visible again while the second peak is absent at first and slowly grows back over several scans. Additionally, the first shoulder of the gold oxidation current at 1.3 V also grows over time.

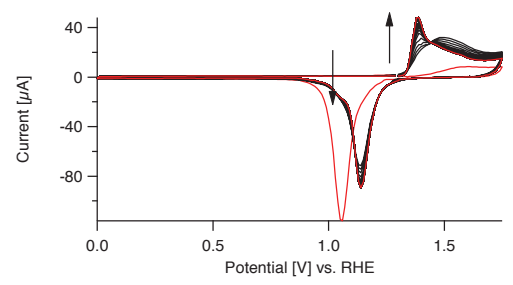


Figure 5.8: Results of a CV measurement with a gold working electrode in a $0.1~M~HClO_4$ electrolyte solution. Conditions: 100 cycles between 0.0 and 1.75 V vs. RHE in a fresh 0.1 M HClO $_4$ electrolyte solution at 100 mV/s, starting at 1.3 V vs. RHE. The electrode was pre-treated by first oxidizing the electrode surface by cycling between 1.3 and 2.0 V vs. RHE for five cycles at 10 mV/s in a 0.1 M HClO $_4$ electrolyte solution, followed by another CV measurement between 1.3 and 2.0 V vs. RHE for five cycles at 10 mV/s in a 0.1 M Na $_2$ SO $_4$ electrolyte solution in the presence of complex 1 and subsequent rinsing with Mili-Q water. The resting potential at the working electrode was kept at 1.3 V vs. RHE throughout the procedure. The arrows in the figure indicate changes in the current profile between subsequent scans.

One possible explanation for these observed changes in the background voltammogram of the gold working electrode, which are apparently triggered by cyclic voltammetry between 1.3 and 2.0 V in the presence of complex 1, could be the formation of surface deposits from complex 1 at high potentials. Those deposits could then be expelled from the surface upon repeated cycling over the gold oxide formation and gold oxide reduction potential region, which would lead to the recovery of the original background voltammogram. However, the EQCM experiments which are described in chapter 3 already rule out the formation of significant surface deposits from complex 1 in 0.1 M Na₂SO₄ electrolyte solution (see Fig 3.8, chapter 3)

A different explanation could be that restructuring of the electrode surface takes place, induced by the presence of complex 1 in solution. This explanation is also in line with results discussed in chapter 4 which already point toward restructuring processes which take place at the electrode surface in the presence of Fe(bpmcn) complexes.

The same experimental procedure that was carried out for complex **1** was repeated for complex **2** to establish whether the observed changes in the voltammogram of the gold background are exclusive for complex **1** or whether other metal complexes exhibit similar effects. Analogous to the experiment with complex **1**, the surface of the working electrode was first oxidized to gold oxide by cycling the potential between **1**.3 and **2**.0 V in a Na₂SO₄ electrolyte solution in the absence of any metal complex (Fig. 5.9a). To prevent gold oxide reduction, the

resting potential was kept at 1.3 V. Subsequently, complex 2 was added to the solution and another CV experiment between 1.3 and 2.0 V was performed for five cycles at 10 mV/s (Fig. 5.9b). Similar to the results obtained for complex 1, the experiment with complex 2 also shows additional oxidative current the first scan of the voltammogram recorded after the addition of complex 2, despite previous complete oxidation of the electrode surface to gold oxide. Also just like in the previous experiment with complex 1, the additional oxidative current is only present in the first scan of the CV experiment after addition of complex 2 and not in subsequent scans. However, the effect of generating additional oxidative current during the first scan after addition of the complex to the electrolyte solution is less pronounced in the case of complex 2 compared to complex 1 (compare Fig. 5.9b and 5.6b).

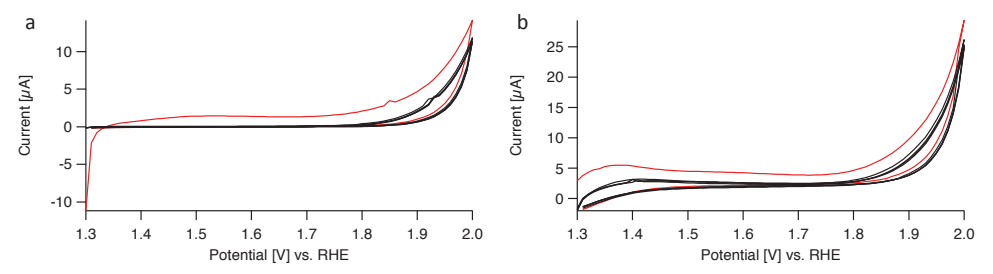


Figure 5.9: (a) Results of a CV measurement with a gold working electrode in a $0.1 \text{ M Na}_2\text{SO}_4$ electrolyte solution, recorded between 1.3 and 2.0 V vs. RHE at 10 mV/s, starting at 1.3 V vs. RHE. The first scan is depicted in red, subsequent scans in black. (b) Results of a CV measurement with a gold working electrode in the presence of 0.5 mM complex 2 in a $0.1 \text{ M Na}_2\text{SO}_4$ electrolyte solution, recorded between 1.3 and 2.0 V vs. RHE at 10 mV/s, starting at 1.3 V vs. RHE. The first scan is depicted in red, subsequent scans in black. The working electrode was pre-treated before the experiment by oxidation of the electrode surface to gold oxide by cycling five times between 1.3 and 2.0 V vs. RHE at 10 mV/s as is shown in Fig. 5.9a.

For the final step of the experiment, the electrode was taken out of the solution containing complex $\mathbf{2}$, rinsed with Milli-Q water and placed in a cell with a fresh electrolyte solution of Na₂SO₄ without complex $\mathbf{2}$ while keeping the resting potential at 1.3 V. A CV experiment between 0.0 and 2.0 V was then recorded for 50 cycles at 100 mV/s, starting each scan at 1.3 V (Fig. 5.10).

The resulting voltammogram shows the same changes to the current profile of the gold background, compared to the initial baseline measurement before exposure to complex **2**, that were previously seen in the experiment with complex **1**. In the first scan, gold oxide reduction peak I is less pronounced compared to the initial measurement before exposure to complex **2** while reduction peak II is clearly present (Fig. 5.10a).

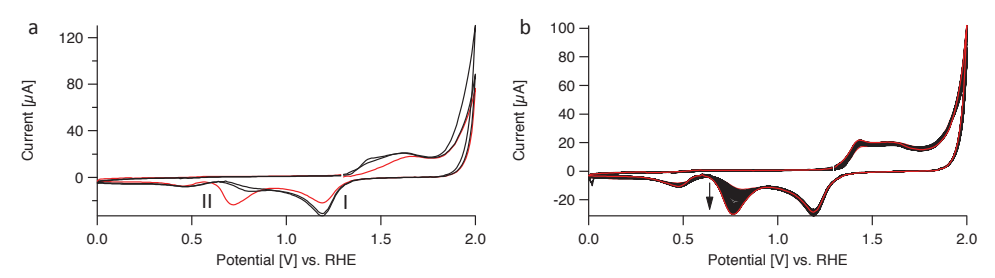


Figure 5.10: Results of a CV measurement with a gold working electrode after cycling five times between 1.3 and 2.0 V vs. RHE at 10 mV/s in the presence of 0.5 mM complex **2** in a 0.1 M Na₂SO₄ electrolyte solution (Fig. 5.9b) and subsequent rinsing of the working electrode. Shown are scans 1-3 (a) and scans 4-50 (b) of the CV experiment recorded between 0.0 and 2.0 V vs. RHE in a 0.1 M Na₂SO₄ electrolyte solution, scanning at 100 mV/s, starting at 1.3 V vs. RHE. Depicted in red are the 1^{st} scan (a) as well as the 4^{th} and 50^{th} scan (b). All remaining scans are depicted in black. The arrows in the figure indicate changes in the current profile between subsequent scans.

During the second and third scan, peak I is more pronounced compared to the first scan and peak II is largely absent. In the subsequent scans peak II can be seen to grow back over time (Fig. 5.10b). However, these observed changes to the voltammogram of the gold background induced by complex 2 in solution appear to be less pronounced compared to the case of complex 1. Gold oxide reduction peak I is still more pronounced in the first scan of the background voltammogram after exposure to complex 2 compared to the case of complex 1 (compare Fig. 5.7a and Fig. 5.10a). Additionally, gold oxide reduction peak II grows back faster over time for the case of complex 2 compared to complex 1 (compare Fig. 5.7b and Fig. 5.10b)

5.3 Conclusions

OLEMS experiments with a PG working electrode show that, contrary to previous reports, no water oxidation takes place at PG working electrodes in the absence of an additional catalyst even at potentials as high as 2.2 V vs. RHE. Instead, only CO_2 formation from the electrode material can be seen with OLEMS, starting at about 1.9 V.

In the presence of metal complexes in solution, the onset of CO_2 formation shifts to more cathodic potentials. This shift of the onset of CO_2 formation shows that high-valent metal oxo-species in solution can facilitate CO_2 formation from carbon electrodes. Depending on where the onset of CO_2 formation lies in comparison to the onset of oxygen evolution, this must be taken into consideration when analyzing the kinetics of electrocatalysts through foot-of-the-wave analysis. Furthermore, the formation of CO_2 from carbon-based electrodes is a clear

drawback compared to other electrode materials for potential sustainable fuel production applications which has to be weighed against potential benefits (cf. chapter 3).

When working with gold working electrodes, the presence of metal complexes in solution seems to induce changes in the structure of the electrode surface. These changes manifest themselves in differences in the current profile of the gold oxide formation and gold oxide reduction processes in background voltammograms of a gold working electrode, measured before and after cycling the potential between 1.3 and 2.0 V in the presence of metal complexes in the electrolyte solution. The comparison of the results obtained with complex 1 (Fig. 5.6-5.7) and complex 2 (Fig. 5.9-5.10) indicates that complex 1 interacts more strongly with the surface of the gold electrode, resulting in more pronounced changes in the background voltammogram being visible in CV experiments.

The exact nature of these changes and the mechanism through which they are induced is not yet clear. To elucidate the processes at the surface of gold working electrodes based on the recorded voltammograms, additional information is needed about the precise processes which give rise to each individual peak on an atomic level. Structural changes at the electrode surface could potentially be visualized by *in situ* spectroscopy or microscopy techniques in combination with electrochemistry.

The results presented in this chapter are in line with the results for the Fe(bpmcn) complexes discussed chapter 4, which also showed evidence for considerable interactions between the complexes and the gold electrode. On one hand, a different oxygen evolution behaviour was observed during the first scan of an OLEMS experiment compared to subsequent scans. On the other hand, the peak current at 2.0 V was found to increase between subsequent scans in CV experiments between 0.0 and 2.0 V.

In order for restructuring of the electrode surface to be induced by dissolved complexes, there must be considerable electronic interaction between the electrode surface and the complex in solution. This means that the interactions between complex and electrode go beyond simple outer sphere electron transfer mechanisms. Despite the potentially important implications for the field, at present, the interactions between metal complexes in solution and the surface of the working electrode have received little to no attention in literature on homogeneous water oxidation catalysis.

In summary, following the results discussed in chapters 3 and 4, the findings presented in this chapter further solidify the concerns that were already expressed throughout this thesis regarding the benchmarking of catalytic systems under electrochemical conditions. The results obtained for both PG and gold working electrodes show that interactions between the complexes in solution and the electrode surface significantly complicate the observed electrochemistry.

The formation of CO_2 from carbon-based electrodes is important for both benchmarking efforts and potential applications in sustainable fuel production. The interactions between dissolved metal complexes and gold working electrodes on the other hand appear to influence the structure of the electrode surface which in turn may affect for example electron transfer rates between the electrode and the catalyst. Therefore the potential influence of any interactions between dissolved complexes and the electrode surface could potentially be of critical importance and needs to be considered carefully when assessing the performance of a homogeneous electrocatalyst.

5.4 Experimental

5.4.1 General

The synthesis and characterization of complex **1** are described in chapter 3 of this thesis.

[Ru(tpy)(bpy)(H₂O)](OTf)₂ (**2**) was synthesized from [RuCl(tpy)(bpy)]Cl according to a modified literature procedure (see below for details).^[24]

 $[RuCl_3(tpy)]$ and [RuCl(tpy)(bpy)]Cl were synthesized according to literature procedures. [24]

5.4.2 Electrochemical experiments

All electrochemical measurements were performed in custom made single-compartment glass cells, recorded on Ivium potentiostats, operated by IviumSoft software, using a three electrode setup with the working electrode in hanging meniscus configuration. The working electrodes used in the experiments were a pyrolytic graphite (PG) disc and a gold disc electrode. The respective (geometric) surface areas are 0.2 cm² (PG) and 0.13 cm² (gold). A large surface area gold plate was used as a counter electrode in all experiments. The reference electrode was a reversible hydrogen electrode (RHE) made up of a platinum mesh in H₂-saturated

electrolyte at the same pH as the electrolyte solution inside the cell. The cell and the reference electrode were connected via a Luggin capillary.

The PG electrode was prepared before each experiment by polishing the electrode surface with sandpaper. The polishing of the PG electrode was followed by removal of excess debris by sonicating the electrode in Milli-Q water for at least five minutes.

The gold electrode was prepared before each experiment by oxidizing the surface at 10 V for 30 s in a 10% H_2SO_4 solution, followed by stripping of the gold oxide layer in a 6 M HCl solution and subsequent electro-polishing of the electrode by scanning for 200 cycles between 0.0 and 1.75 V vs. RHE at 1000 mV/s in a 0.1 M $HClO_4$ electrolyte solution.

All glassware used in electrochemical measurements was routinely cleaned of any organic contamination by soaking in potassium permanganate solution over night. Prior to each experiment, the glassware was cleaned by threefold rinsing and boiling in Milli-Q water. All electrolyte solutions were prepared from p.a. grade chemicals (Merck Suprapur®) and Milli-Q water (resistivity $\geq 18.2~\text{M}\Omega$). Prior to measurements, the electrolyte solution was purged of air by bubbling with argon (Linde, Ar 6.0) for at least 20 minutes. During the measurements, the cell was constantly kept under argon flow to prevent air from entering.

For the OLEMS measurements, the gasses formed at the working electrode were collected via a hydrophobic tip (KEL-F with a porous Teflon plug) in close proximity to the surface of the working electrode and analyzed in a QMS 200 mass spectrometer. A detailed description of the OLEMS setup is available elsewhere. [25] For the mass spectrometry data recorded during cyclic voltammetry experiments, background correction was done by assuming an exponential decay fit (concerns figure 5.3).

5.4.3 Synthesis of $[Ru(tpy)(bpy)(H_20)](OTf)_2$ (2)

[RuCl(tpy)(bpy)]Cl (200 mg, 0.36 mmol) was dissolved in 25 mL of a mixture of 75% acetone and 25% water. AgOTf (183 mg, 0.72 mmol) was added and the mixture was refluxed for 1 h. The mixture was allowed to cool down to room temperature before being filtered over celite to remove all of the formed AgCl. After evaporation of the solvent in vacuum, the obtained crude material was recrystallized from a minimal amount of acetone and water mixture (75:25) in the fridge. Yield: 122 mg (0.15 mmol, 42%)

ESI-MS (H_2O) calcd. for $C_{25}H_{19}N_5Ru$ [M]²⁺ 245.5; Found: [M]²⁺ 245.3, [M+ H_2O]²⁺ 254.2

Elemental analysis calcd. (%) for $C_{27}H_{21}F_6N_5O_7RuS_2$ (806.67 g/mol): C 40.20, H 2.62, N 8.68 Found: C 40.43, H 2.79, N 8.73.

¹H NMR (400 MHz, D₂O) δ [ppm] = 9.50 (d, J = 5.7 Hz, 1H), 8.64 (d, J = 8.2 Hz, 1H), 8.55 (d, J = 8.1 Hz, 2H), 8.42 (d, J = 8.1 Hz, 2H), 8.29 (m, 2H), 8.18 (t, J = 8.1 Hz, 1H), 7.99 (ddd, J = 7.3, 5.6, 1.3 Hz, 1H), 7.93 (ddd, J = 7.9, 1.5 Hz, 2H), 7.77 (d, J = 5.7 Hz, 2H), 7.64 (ddd, J = 7.9, 1.5 Hz, 1H), 7.34-7.24 (m, 3H), 6.89 (ddd, J = 7.4, 5.8, 1.3 Hz, 1H).

5.4.4 Sample preparation

Due to slow dissolution of complex ${\bf 1}$ in 0.1 M Na₂SO₄ electrolyte solution, the complex was initially dissolved in a small amount of Milli-Q water (typically 1-2 mL) and subsequently added to the electrochemical cell containing the electrolyte solution. The concentration of electrolyte in the cell was adjusted to account for the resulting dilution. To achieve faster dissolution of complex ${\bf 1}$ in water the crystals were powderized before dissolving them in water.

For electrochemical experiments with complex **1**, the complex was dissolved in air-saturated Milli-Q water and subsequently added to the electrochemical cell after complete dissolution. The electrolyte was then purged again of air by bubbling with argon for several minutes.

For electrochemical experiments with complex **2**, the complex was sonicated in a few mL of the electrolyte solution to achieve complete dissolution and subsequently added to the electrochemical cell. The electrolyte was then purged again of air by bubbling with argon for several minutes.

All experiments with complex **1** and **2** were performed at a concentration of 0.5 mM unless otherwise specified.

5.5 References

- [1] J. D. Benck; B. A. Pinaud; Y. Gorlin; T. F. Jaramillo, PLoS One 2014, 9, e107942.
- [2] A. M. Ullman; Y. Liu; M. Huynh; D. K. Bediako; H. Wang; B. L. Anderson; D. C. Powers; J. J. Breen; H. D. Abruna; D. G. Nocera, *J. Am. Chem. Soc.* **2014**, *136*, 17681-17688.
- [3] S. Fukuzumi; D. Hong, Eur. J. Inorg. Chem. **2014**, 2014, 645-659.
- [4] B. Limburg; E. Bouwman; S. Bonnet, Coord. Chem. Rev. 2012, 256, 1451-1467.
- [5] O. Diaz-Morales; F. Calle-Vallejo; C. de Munck; M. T. M. Koper, *Chem. Sci.* **2013**, *4*, 2334.

- [6] K. G. Kottrup, This Thesis, Chapter 3.
- [7] Y. Yi; G. Weinberg; M. Prenzel; M. Greiner; S. Heumann; S. Becker; R. Schlögl, *Catal. Today* **2017**, *295*, 32-40.
- [8] R. Matheu; M. Z. Ertem; J. Benet-Buchholz; E. Coronado; V. S. Batista; X. Sala; A. Llobet, *J. Am. Chem. Soc.* **2015**, *137*, 10786-10795.
- [9] C. Costentin; S. Drouet; M. Robert; J. M. Saveant, *J. Am. Chem. Soc.* **2012**, *134*, 11235-11242.
- [10] H. Angerstein-Kozlowska; B. E. Conway; A. Hamelin; L. Stoicoviciu, *Electrochim. Acta* **1986**, *31*, 1051-1061.
- [11] H. Angerstein-Kozlowska; B. E. Conway; A. Hamelin; L. Stoicoviciu, *J. Electroanal. Chem. Interfacial Electrochem.* **1987**, *228*, 429-453.
- [12] Z. Borkowska; A. Tymosiak-Zielinska; G. Shul, *Electrochim. Acta* **2004**, *49*, 1209-1220.
- [13] A. Hamelin, J. Electroanal. Chem. 1996, 407, 1-11.
- [14] A. Hamelin; A. M. Martins, J. Electroanal. Chem. 1996, 407, 13-21.
- [15] B. B. Blizanac; C. A. Lucas; M. E. Gallagher; M. Arenz; P. N. Ross; N. M. Marković, *J. Phys. Chem. B* **2004**, *108*, 625-634.
- [16] L. D. Burke; P. F. Nugent, Gold Bull. 1997, 30, 43-53.
- [17] L. D. Burke; P. F. Nugent, Gold Bull. 1998, 31, 39-50.
- [18] A. Hamelin; M. J. Sottomayor; F. Silva; S.-C. Chang; M. J. Weaver, J. Electroanal. Chem. Interfacial Electrochem. 1990, 295, 291-300.
- [19] B. Lertanantawong; A. P. O'Mullane; W. Surareungchai; M. Somasundrum; L. Declan Burke; A. M. Bond, *Langmuir* **2008**, *24*, 2856-2868.
- [20] M. J. Nicol, *Gold Bull.* **1980**, *13*, 46-55.
- [21] M. J. Nicol, Gold Bull. 2013, 13, 105-111.
- [22] A. Hamelin; L. Stoicoviciu, *J. Electroanal. Chem. Interfacial Electrochem.* **1987**, 234, 93-105.
- [23] A. Hamelin; L. Stoicoviciu, *J. Electroanal. Chem. Interfacial Electrochem.* **1987**, 236, 267-281.
- [24] K. J. Takeuchi; M. S. Thompson; D. W. Pipes; T. J. Meyer, *Inorg. Chem.* **1984**, *23*, 1845-1851.
- [25] A. H. Wonders; T. H. M. Housmans; V. Rosca; M. T. M. Koper, *J. Appl. Electrochem.* **2006**, *36*, 1215-1221.

Summary, conclusion and outlook

6

6.1 Summary

6.1.1 Introduction

There are several drawbacks that are associated with the use of fossil fuels in energy production. Their low rate of formation makes their use unsustainable since they are consumed much faster than they are regenerated. This also means that burning fossil fuels leads to a build-up of CO₂ in the atmosphere which drives climate change. It is therefore imperative that a transition is made in the near future from fossil fuels to sustainable energy sources. In order to achieve power generation based solely on sustainable sources on a global scale, utilization of solar energy is essential since other sustainable energy sources like wind cannot provide sufficient power for the entire planet.

While the conversion of solar energy into electricity via photovoltaics is already possible, the transportation and storage of the collected energy remains problematic. Batteries are costly and have a low energy density compared to chemical fuels^[4] and not all technologies can be easily adapted from fuel to electricity. Therefore new technologies are required, for the conversion of solar energy into a chemical fuel, in order to achieve widespread utilization of solar energy as the primary source of energy.

Nature is able to generate biomass from CO₂, sunlight and water through photosynthesis with O₂ being the only by-product. However, the reactions involved in photosynthesis are highly complex. Therefore, artificial solar-to-fuel conversion schemes necessarily have to be simpler processes like the splitting of water into dihydrogen and dioxygen. In order to achieve water splitting, efficient and robust catalysts are required for both the hydrogen evolution reaction and the oxygen evolution reaction. Between the hydrogen evolution reaction and the oxygen evolution reaction, the latter, also commonly referred to as water oxidation, is substantially more difficult to catalyze. The water oxidation reaction involves the rearrangement of four electrons and four protons which results in a kinetically very challenging reaction.^[5] As a result, catalyzing the water oxidation reaction has been a research topic of great interest for over a decade now and a wide range of different catalysts, both homogeneous and heterogeneous, has been developed.^[6-7]

In chapter 1 of this thesis an overview is provided over the progress in homogeneous water oxidation catalysis with emphasis on iron-based water oxidation catalysts in particular. Additionally, the use of chemical oxidants in large excess — currently the standard methodology for studying potential water oxidation catalysts — is discussed critically in comparison with electrochemistry as an alternative methodology.

6.1.2 Structure-activity relationships of iron-based electrocatalysts for the water oxidation reaction

In this thesis, iron-based water oxidation catalysts are described, based on the three different ligand platforms cyclam, bpmcn and Hbbpya (with bpmcn = N,N'-dimethyl-N,N'-bis(2-pyridylmethyl)-cyclohexane-1,2-diamine; Hbbpya = N,N-bis(2,2'-bipyrid-6-yl)amine and cyclam = 1,4,8,11-tetraazacyclotetradecane) (Fig. 6.1).

Figure 6.1: Structures of the three ligand platforms used in the iron-based water oxidation catalysts described in this thesis: 1,4,8,11-tetraazacyclotetradecane (cyclam, left), *N*,*N*′-dimethyl-*N*,*N*′-bis(2-pyridylmethyl)-cyclohexane-1,2-diamine (bpmcn, middle) *N*,*N*-bis(2,2′-bipyrid-6-yl)amine (Hbbpya, right).

In chapter 2, three complexes based on the macrocyclic cyclam ligand are described (Fig. 6.2). The complexes *cis*-[Fe(cyclam)Cl₂]Cl and *trans*-[Fe(cyclam)Cl₂] are both based on the same ligand and differ only in their coordination-geometry.

cis-[Fe(cyclam)Cl]Cl₂ [Fe(cyclamacetate)Cl] trans-[Fe(cyclam)Cl₂]

Figure 6.2: Structures of the three cyclam-based complexes discussed in chapter 2.

The complex [Fe(cyclamacetate)Cl] features a modified cyclam ligand which has an additional acetate group that can coordinate in axial position on the iron

centre, resulting in a pentadentate ligand. The results of CV experiments in 0.1 M NaClO₄ electrolyte solution showed that the Fe^{II/III} redox couples of *cis*-[Fe(cyclam)Cl₂]Cl and [Fe(cyclamacetate)Cl] lie at considerably more cathodic potentials than the Fe^{II/III} redox couple of *trans*-[Fe(cyclam)Cl₂]. On-line electrochemical mass spectrometry (OLEMS) measurements of all three complexes showed that *cis*-[Fe(cyclam)Cl₂]Cl and [Fe(cyclamacetate)Cl] are capable of catalyzing water oxidation with an onset potential of oxygen evolution at about 1.8 V. *Trans*-[Fe(cyclam)Cl₂] on the other hand was found to be catalytically inactive at potentials up to 2.0 V. This comparison shows that the electronic structure of a complex is crucial for enabling catalytic activity at lower overpotentials. Having an Fe^{II/III} redox couple at a lower potential is indicative of a structure in which more electron density is donated from the ligand to the metal centre which should help to stabilize the high oxidation states which are required to achieve water oxidation.

The results of the OLEMS experiments presented in chapter 2 also show that considerable amounts of CO_2 are being formed for all three complexes with an onset of CO_2 formation below that of the onset of O_2 evolution. This observation could indicate a weakness of cyclam as a ligand platform for reactions under strongly oxidizing conditions.

6.1.3 The role of the electrode surface in electrocatalytic homogeneous water oxidation

Due to the use of a carbon-based working electrode in the experiments described in chapter 2, it is difficult to unambiguously determine the electrode or the cyclam ligand as the source of the CO₂ formation. The presence of chloride ions in the structures of all three cyclam-based complexes prohibits the use of other electrode materials such as gold since the gold oxide layer formed at the surface of the electrode at high potentials is unstable in the presence of halide ions. This leads to a large oxidative background current which makes interpretation of the voltammograms difficult (see Fig. 2.2, chapter 2). These limitations have been addressed in the follow-up work described in chapter 3.

In chapter 3 the synthesis and characterization of a new dinuclear iron complex based on the ligand Hbbpya is described. The complex was designed based upon the results described in chapter 2. The polypyridyl-type ligand Hbbpya is expected to be more robust towards oxidation than the aliphatic cyclam ligand. Additionally, the compatibility of the complex with different electrode materials

was ensured by avoiding the use of halide ions. The electrochemical experiments described in chapter 3 with the complex [(MeOH)Fe(Hbbpya) $-\mu$ -O-(Hbbpya)Fe(MeOH)](OTf) $_4$ revealed two main results: I) when using a pyrolytic graphite (PG) working electrode, substantial amounts of CO $_2$ are detected in OLEMS experiments while little to no CO $_2$ formation is observed in OLEMS experiments with a gold working electrode and II) using a working electrode made up of graphitic carbon results in a substantially lower overpotential for oxygen evolution catalyzed by the Fe(Hbbpya) complex compared to working electrodes made up of gold or non-graphitic carbon.

 ${\rm CO_2}$ formation has already been described in literature to occur in experiments with carbon-based electrodes under the harsh conditions required for electrocatalytic water oxidation. However, the first direct evidence for the carbon electrode being the source of the ${\rm CO_2}$ is provided by the difference in ${\rm CO_2}$ formation between a PG working electrode and a gold working electrode in the OLEMS experiments described in chapter 3.

The difference in oxygen evolution behaviour of the Fe(Hbbpya) complex between a PG working electrode and a gold working electrode suggests different mechanisms of the oxygen evolution reaction by the complex for graphitic and non-graphitic electrode materials. π - π -stacking interactions between the complex and the surface of an sp² carbon electrode could be a possible explanation for this phenomenon because of the presence of an extended aromatic system in the Hbbpya ligand. To the best of our knowledge, this is the first evidence for a clear substrate influence of the electrode material in electrocatalytic water oxidation.

The results described in chapter 4 showed two indications for the involvement of the surface of a gold working electrode in the resulting electrochemistry of the complexes H_4 - α -[Fe(bpmcn)(OTf)₂] and D_4 - α -[Fe(bpmcn)(OTf)₂]: I) The peak current at 2.0 V increased between scans in CV experiments in which the potential was cycled repeatedly over the gold oxide formation and reduction area and II) the first scan was markedly different from subsequent scans in an OLEMS experiment between 1.3 and 2.0 V in terms of the current profile as well as O_2 and CO_2 mass traces. While the underlying mechanism for these observations could not yet be determined conclusively, the evidence points to a connection to gold oxide formation processes at the electrode surface. Other explanations such as the formation of surface deposits under high potential conditions could be ruled out through control experiments with an electrochemical quartz crystal microbalance (EQCM) in combination with cyclic voltammetry.

6.1.4 Challenges in benchmarking of homogeneous electrocatalysts for the water oxidation reaction

The results described in section 6.1.3 regarding the influence of the electrode surface on the results of electrochemical water oxidation catalysis are not only of fundamental interest for the understanding of the processes involved in electrocatalytic water oxidation on a molecular level and the design of improved water oxidation systems. Beyond that, the results also have very important implications for attempts at benchmarking water oxidation catalysts with regards to future applications in water splitting.

The formation of CO_2 from carbon-based working electrodes is an undesired side reaction. Not only does this represent a challenge for applications in sustainable energy production, it also means that potential formation of CO_2 must be accounted for when investigating the kinetics of catalysis with carbon-based working electrodes. Additionally, the formation of CO_2 from the electrode material implies that the surface of a carbon-based working electrode changes constantly under oxidative electrocatalytic conditions.

The dynamic behaviour observed in experiments with a gold working electrode described in chapter 4 also represents a significant obstacle for obtaining reliable benchmark values when gold is used as an electrode material. Therefore, the interplay between complexes in solution and the electrode surface was explored further as is described in chapter 5.

The results of a series of CV experiments show that both PG and gold working electrodes behave differently in the presence and in the absence of metal complexes in the electrolyte solution. A PG working electrode showed an onset of CO₂ formation at a lower potential in the presence of metal complexes compared to blank experiments. This means that metal complexes which are capable of catalyzing the water oxidation reaction also catalyze the oxidation of carbon-based electrodes to CO₂. In the case of a gold working electrode, the presence of metal complexes in solution resulted in changes to the gold oxide formation and reduction pattern in the voltammogram of the gold background. Even though the nature of those changes and the mechanism through which they are induced remains unclear, these results show that the presence of metal complexes in solution influences the surface structure of a gold working electrode. This leads us to conclude that there must be substantial electronic interaction between the complexes and the electrode surface which goes beyond simple outer sphere electron transfer.

While the results of chapter 3 show that the choice of electrode material can significantly influence the electrochemical behaviour of a given complex, the results of chapters 4 and 5 show that dynamic processes at the surface of a working electrode can lead to changes over time in electrochemical experiments. These results demonstrate the importance of considering the electrode material as part of the electrocatalytic system.

The results of the work presented in this thesis show that coordination complexes

6.2 General conclusions

based on iron can be made to work as electrocatalysts for the water oxidation reaction. We found that in order to achieve robust and efficient water oxidation electrocatalysis based on iron, it is important to not only find a stable ligand platform but to also control the electronic structure of the complex (chapter 2). Considering that benchmarking of catalysts is an important part of the development of new catalysts, the interactions between homogeneous electrocatalysts and the surface of the working electrode need to be considered carefully, which so far has been largely ignored in literature. The interactions between the electrocatalyst and the surface of the working electrode can have important consequences, both for the catalytic behaviour of the catalyst (chapters 3 and 4) and for the electrode material itself (chapter 5). As a result, useful comparisons between different electrocatalysts can only be made when the same electrode material is used in each case. Additionally, electrocatalysts should be studied with several different electrode materials whenever possible to assess to which extent the electrode surface might be involved in catalysis. While some catalysts may experience a beneficial influence from a certain electrode material such as graphitic carbon (chapter 3) the same is not necessarily true for other

In order to obtain an estimation of the relative catalytic activities of the catalysts reported in this thesis, in table 6.1 we compare the $(I_{cat}/I_p)^2$ values (cf. Appendix B) of the complexes cis-[Fe(cyclam)Cl₂]Cl (chapter 2), [(MeOH)Fe(Hbbpya)– μ -O–(Hbbpya)Fe(MeOH)](OTf)₄ (chapter 3) and H₄- α -[Fe(bpmcn)(OTf)₂] (chapter 4). Keeping in mind the aforementioned challenges in determining reliable benchmark values, the data is derived from CV experiments with graphitic working electrodes for each catalyst. This allows us to use O₂ to CO₂ ratios from OLEMS measurements as an indicator of the relative amount of current caused by oxygen evolution for each complex. Since the O₂ to CO₂ ratios fall within the same

catalysts in combination with the same electrode material (chapter 4).

order of magnitude for all three complexes, the $(I_{cat}/I_p)^2$ values suggest that the Fe(Hbbpya) complex is the most active electrocatalyst described in this thesis. Considering that the ratio of O_2 to CO_2 only represents a rough estimation of the faradaic efficiency, we refrain from assigning definitive catalytic turnover frequencies to any of the $(I_{cat}/I_p)^2$ values.

In terms of catalytic overpotential the Fe(Hbbpya) complex reported in chapter 3 clearly stands out as having the lowest onset potential of water oxidation with respect to the thermodynamic standard potential for the water oxidation reaction of 1.23 V vs. RHE. The complexes cis-[Fe(cyclam)Cl₂]Cl and α -[Fe(bpmcn)(OTf)₂] showed onsets of water oxidation around 1.8 V (Fig. 2.6, chapter 2 and Fig. 4.13, chapter 4) while the Fe(Hbbpya) complex showed oxygen evolution at potentials as low as 1.6 V (Fig. 3.6, chapter 3).

Table 6.1: Benchmark values for selected water oxidation catalysts described in this thesis[†]

Catalyst	E [V]	$(I_{cat}/I_p)^2$	O ₂ /CO ₂ Ion current*
cis-[Fe(cyclamCl₂]Cl	2.0	3×10 ^{2 [a]}	2.8±0.8
H_4 - α -[Fe(bpmcn)(OTf) ₂]	2.0	1×10 ^{2 [b]}	2.0±0.2
[((MeOH)Fe(Hbbpya)) ₂ –µ-O](OTf) ₄	2.0	7×10 ^{2 [c]}	2.5±0.4
$[((MeOH)Fe(Hbbpya))_2-\mu-O](OTf)_4$	1.75	1×10 ^{2 [c]}	8.7±1.4

^a based on data from figure 2.4b, chapter 2; ^b based on data from a CV experiment with 1.1 mM α -[Fe(bpmcn)(OTf)₂] in a 0.1 M NaClO₄ electrolyte solution recorded between 0.0 and 2.0 V vs. RHE with a GC working electrode at 10 mV/s; ^c based on data from figure 3.5b, chapter 3.

6.3 Outlook & Perspectives

Based on the results obtained over the last few years, it is now established that iron complexes can function as electrocatalysts for the water oxidation reaction. ^[9-11] To further improve the efficiency of homogeneous iron-based water oxidation electrocatalysts, targeted variations of the electronic properties of ligands are needed to control the redox potential of the crucial high oxidation state

[†]All $(I_{cat}/I_p)^2$ values were determined from the 2^{nd} scan of a CV experiment of each respective catalyst, measured between 0.0 and 2.0 V vs. RHE at a scan rate of 10 mV/s. Electrochemical experiments with $[((MeOH)Fe(Hbbpya))_2-\mu-O](OTf)_4$ were performed at half the catalyst concentration of the experiments with cis-[Fe(cyclam)Cl₂]Cl and H_4 - α -[Fe(bpmcn)(OTf)₂] to ensure the same concentration of iron centres in each case.

^{*}The values for the ratios of m/z = 32 to m/z = 44 ion currents at 2.0 V vs. RHE were determined by taking the average over all available datasets for each catalyst. The value of the ratio of m/z = 32 to m/z = 44 ion currents for $[((MeOH)Fe(Hbbpya))_2-\mu-O](OTf)_4$ at 1.75 V vs. RHE was determined by averaging the ion currents over the range of 1.70–1.80 V vs. RHE for each available dataset and then taking the average over all datasets. The errors represent the largest deviation from the average that was measured. Background correction was performed by assuming an exponential decay fit for all ion current traces.

intermediates in order to achieve low overpotential catalysis. A similar approach has already been successfully employed for long established ruthenium-based catalysts. [12] Accordingly, a systematic experimental study of differently substituted ligands guided by theoretical calculations could be helpful for finding low overpotential iron-based electrocatalysts.

The incorporation of additional functional groups could further improve the catalytic activity, once the energy barrier for reaching the highest oxidation state intermediates is sufficiently low. When the O–O bond formation step is rate determining, facilitating this step could lead to an improved catalytic performance. In a water nucleophilic attack mechanism, the O–O bond formation involves a high-energy intermediate in the form of [M–O–OH₂]. Proton shuttles can lower the energy barrier associated with the O–O bond formation step by abstracting a proton from the incoming water molecule, thus avoiding the formation of this energetically unfavourable intermediate (Fig. 6.3). The proton shuttle in this case can be an external base such as phosphate or acetate buffer which is present in excess, a pending basic group in the second coordination sphere of the metal centre or a neighbouring ligand at the metal centre.

Figure 6.3: Schematic representation of a general water nucleophilic attack mechanism involving a proton acceptor B (with M = metal, L = ligand)

The experiments described in chapters 3-5 of this thesis provide evidence for considerable interactions between dissolved complexes and the surface of the working electrode in electrocatalytic applications. Further research is still required in order obtain a better understanding of the mutual influence between the surface of the electrode material and the electrochemistry of complexes in solution. The combination electrochemical measurements with online spectroscopic measurements would be desirable to obtain a better understanding of the extent of electronic interactions between the Fe(Hbbpya) catalyst and the surface of graphitic electrodes. Graphene-based carbon electrodes could potentially prove to be suitable substrates for combining for example cyclic voltammetry and UV-vis spectroscopy.

In the case of gold working electrodes, surface-enhanced Raman spectroscopy (SERS) in combination with ¹⁸O isotopically labeled water could be used to gain insight into the fate of the oxide layer on the electrode surface at potentials above 1.3 V vs. RHE in the presence of metal complexes in solution. Additionally, surface characterization techniques such as *in situ* and *ex situ* microscopy will be required to understand the apparent restructuring processes that take place at the surface of gold electrodes in the presence of metal complexes

6.4 References

- [1] N. S. Lewis; D. G. Nocera, *Proc. Natl. Acad. Sci. U. S. A.* **2006**, *103*, 15729-15735.
- [2] J. Chow; R. J. Kopp; P. R. Portney, *Science* **2003**, *302*, 1528-1531.
- [3] N. S. Lewis, Science 2007, 315, 798-801.
- [4] D. G. Nocera, ChemSusChem **2009**, 2, 387-390.
- [5] M. T. M. Koper, Chem. Sci. 2013, 4, 2710.
- [6] J. D. Blakemore; R. H. Crabtree; G. W. Brudvig, *Chem. Rev.* **2015**, *115*, 12974-13005.
- [7] J. Li; R. Guttinger; R. More; F. Song; W. Wan; G. R. Patzke, *Chem. Soc. Rev.* **2017**, *46*, 6124-6147.
- [8] A. M. Ullman; Y. Liu; M. Huynh; D. K. Bediako; H. Wang; B. L. Anderson; D. C. Powers; J. J. Breen; H. D. Abruna; D. G. Nocera, *J. Am. Chem. Soc.* **2014**, *136*, 17681-17688.
- [9] E. L. Demeter; S. L. Hilburg; N. R. Washburn; T. J. Collins; J. R. Kitchin, *J. Am. Chem. Soc.* **2014**, *136*, 5603-5606.
- [10] K. G. Kottrup; D. G. H. Hetterscheid, *Chem. Commun.* **2016**, *52*, 2643-2646.
- [11] P. Tan; H. K. Kwong; T. C. Lau, Chem. Commun. 2015, 51, 12189-12192.
- [12] P. Garrido-Barros; C. Gimbert-Surinach; R. Matheu; X. Sala; A. Llobet, *Chem. Soc. Rev.* **2017**, *46*, 6088-6098.
- [13] Z. Chen; J. J. Concepcion; X. Hu; W. Yang; P. G. Hoertz; T. J. Meyer, *Proc. Natl. Acad. Sci. U. S. A.* **2010**, *107*, 7225-7229.
- [14] I. Siewert, Chem. Eur. J. 2015, 21, 15078-15091.
- [15] D. K. Dogutan; R. McGuire, Jr.; D. G. Nocera, J. Am. Chem. Soc. **2011**, 133, 9178-9180.
- [16] J. L. Fillol; Z. Codola; I. Garcia-Bosch; L. Gomez; J. J. Pla; M. Costas, *Nat. Chem.* **2011**, *3*, 807-813.

Appendix A

Supplementary information for Chapter 2

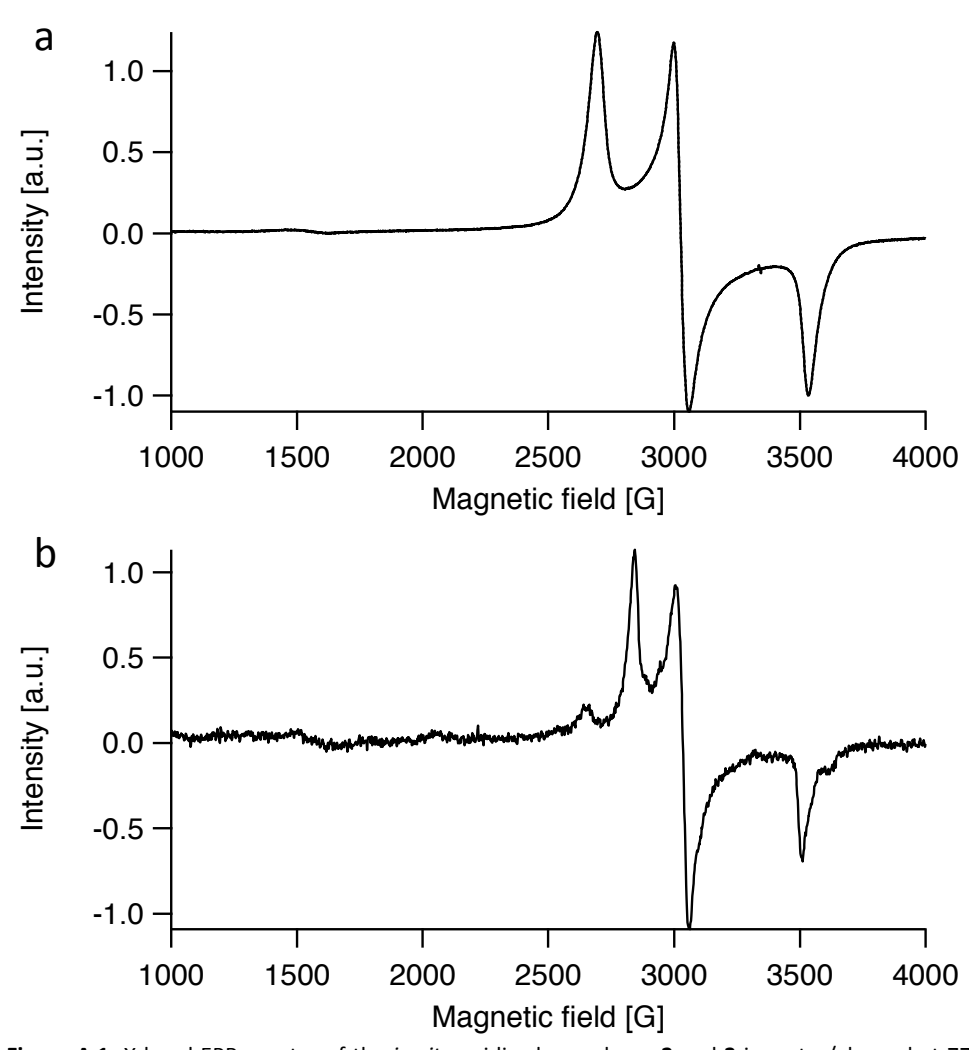


Figure A.1: X-band EPR spectra of the *in situ* oxidized complexes **2** and **3** in water/glycerol at 77 K. (a) Oxidized complex **2**; $\nu = 9.348$ GHz; g-values: 2.48, 2.21, 1.89 (b) Oxidized complex **3**; $\nu = 9.354$ GHz; g-values: 2.39, 2.24, 1.93

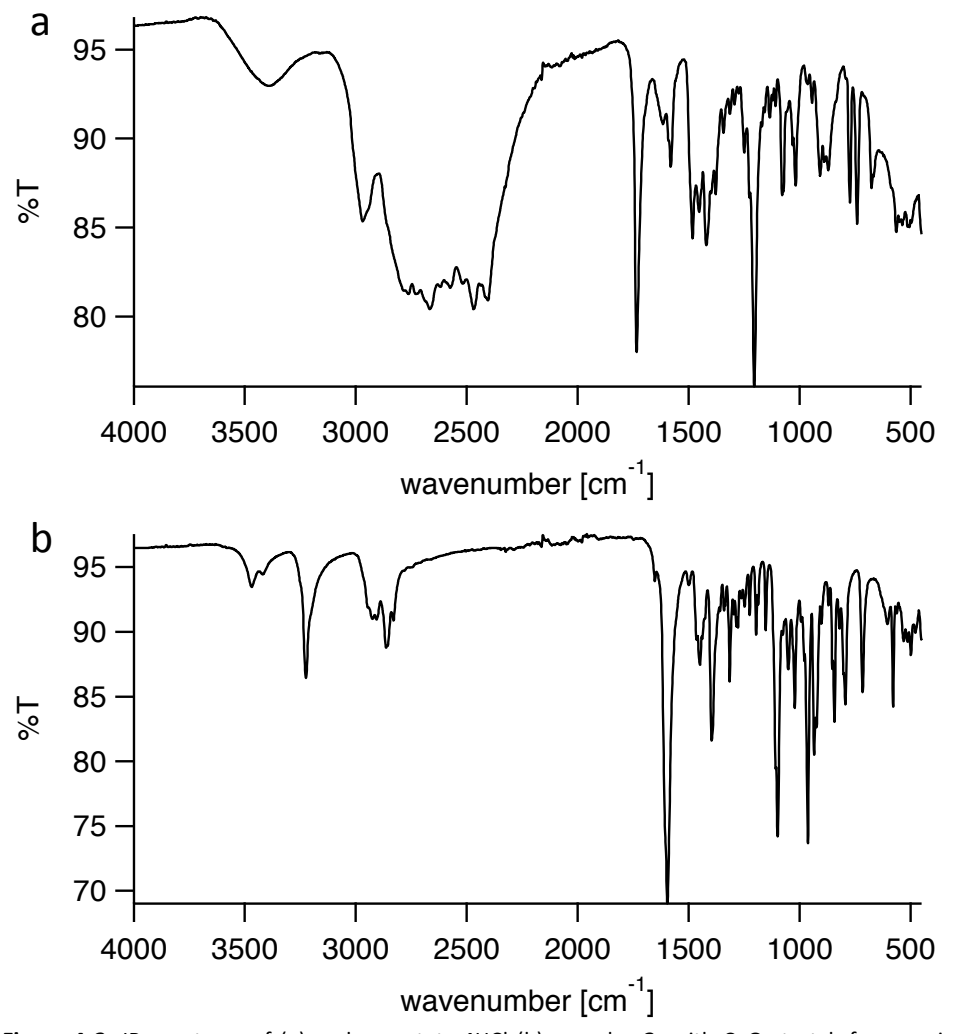


Figure A.2: IR spectrum of (a) cyclamacetate \cdot 4HCl (b) complex **2**; with C=O stretch frequencies of (a) 1734 cm⁻¹ and (b) 1595 cm⁻¹.

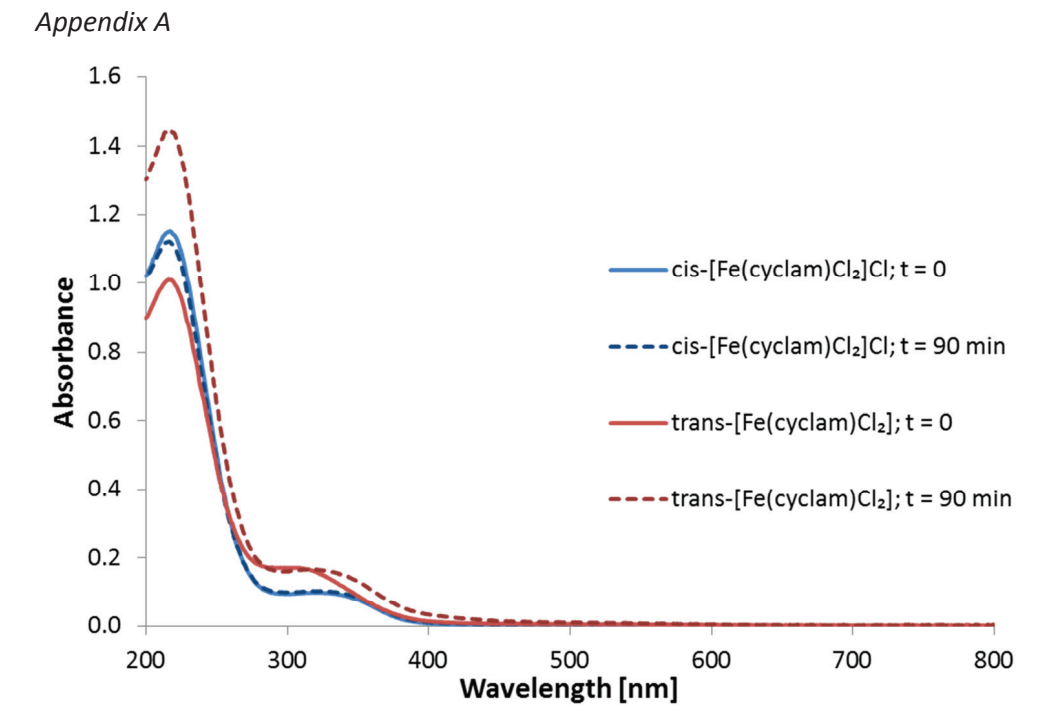


Figure A.3: UV-vis spectra of complexes 1 and 3 over time (t = 0 min \rightarrow t = 90 min). Complex 1 is stable over the observed time span, whereas complex 3 changes noticeably within the first hour, likely due to oxidation from Fe^{II} to Fe^{III}. Both complexes give clearly different absorption spectra and show no signs of cis-trans-isomerization on the timescale of our experiments. Both complexes were used in identical concentrations of 0.11 mM.



Figure A.4: Solid material deposited onto the PG electrode surface during OLEMS measurement of complex **3** in 0.1 M phosphate buffer (pH 7.5)

Appendix B

Supplementary information for Chapter 3

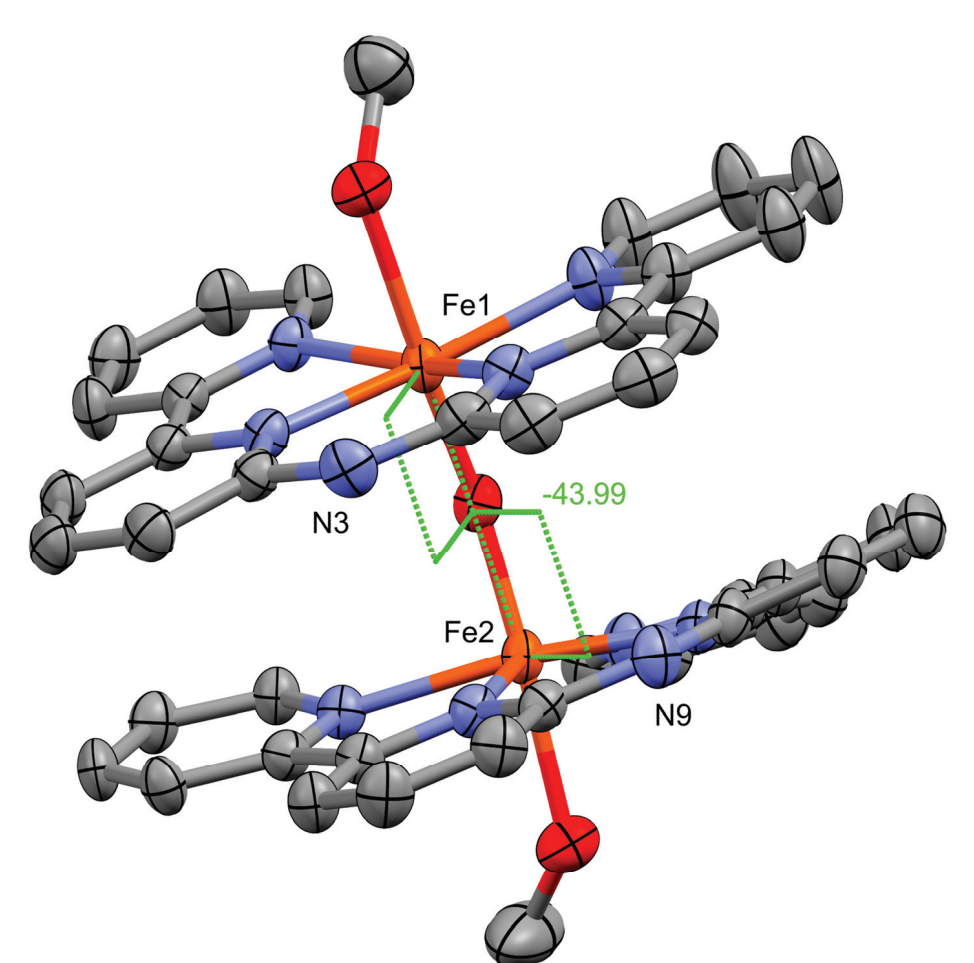


Figure B.1: Illustration of the offset between the two Hbbpya ligands in the crystal structure of [1]. Indicated is the torsion angle measured along N3-Fe1-Fe2-N9. Ellipsoids are shown with 50% probability. All hydrogen atoms and the four triflate counter-ions have been omitted for clarity.

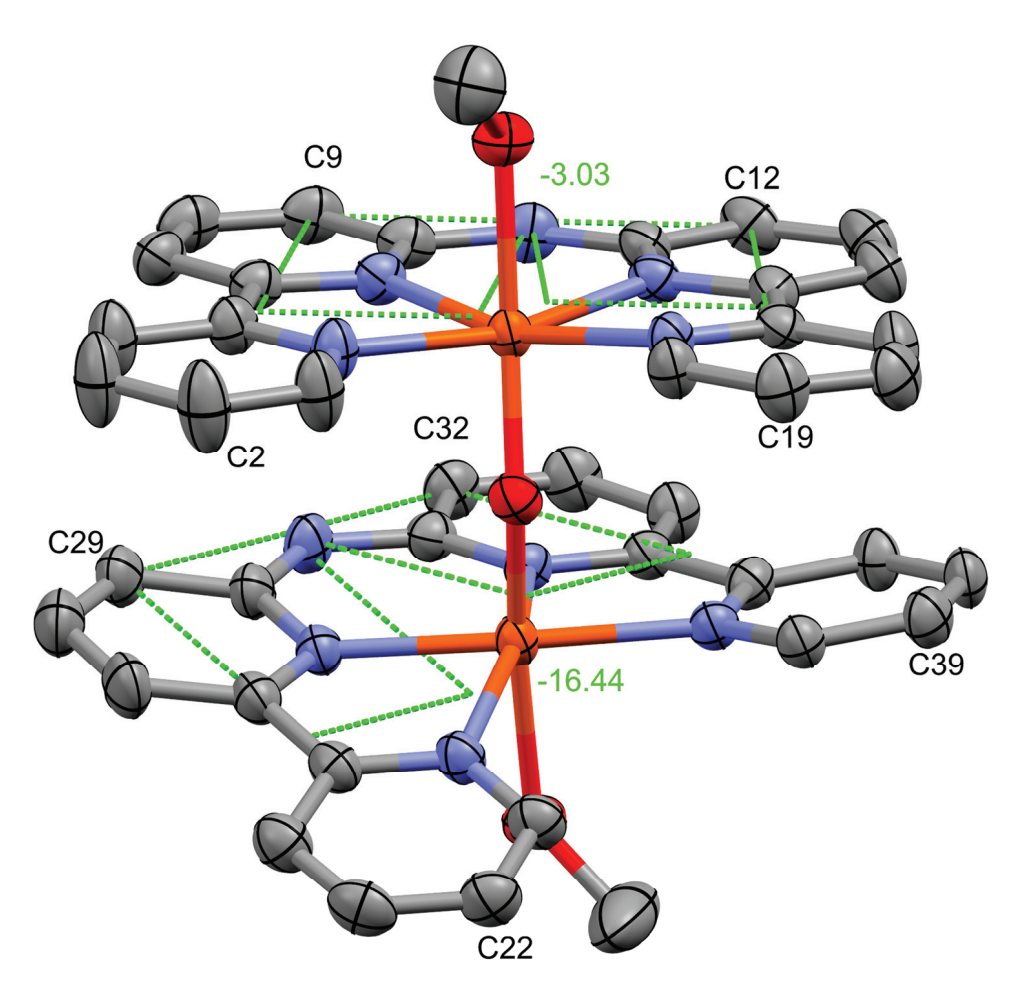


Figure B.2: Internal torsion angles of the two Hbbpya ligands in the crystal structure of [1]. The angles were calculated along C2-C9-C12-C19 and C22-C29-C32-C39 respectively which represent the respective 4 and 4' position carbon atoms of each bipyridine unit. Ellipsoids are shown with 50% probability. All hydrogen atoms and the four triflate counter-ions have been omitted for clarity.

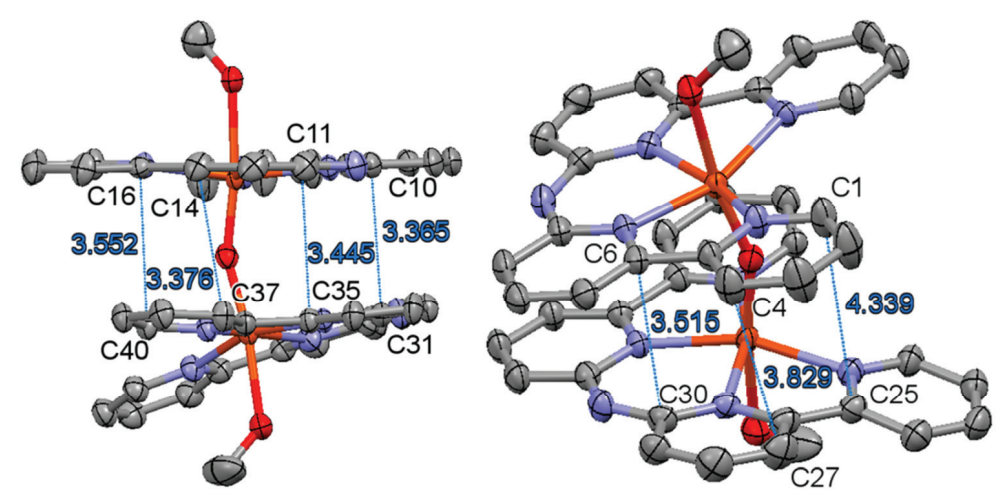


Figure B.3: Distances between the two Hbbpya ligands in the crystal structure of [1], measured between selected carbon atoms of the Hbbpya ligand. The pairs of carbon atoms in the measurements are: C1-C25, C4-C27, C6-C30, C10-C32, C11-C35, C14-C37 and C16-C40. Ellipsoids are shown with 50% probability. All hydrogen atoms and the four triflate counter-ions have been omitted for clarity.

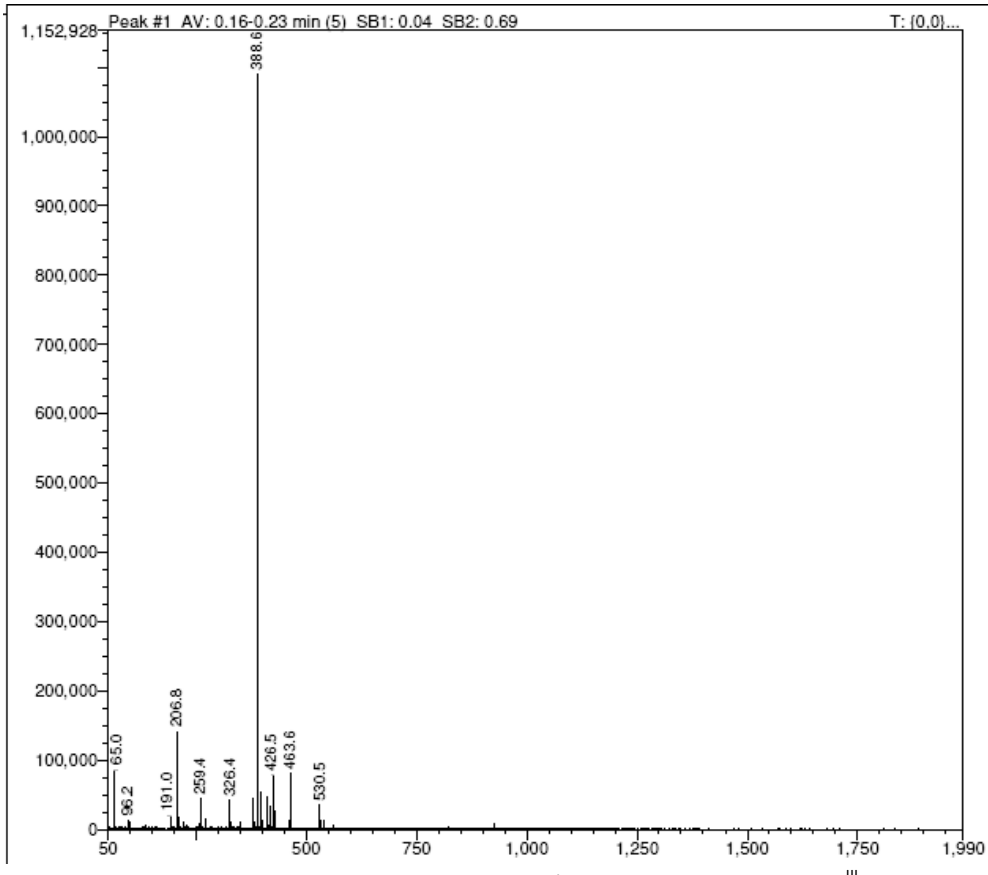


Figure B.4: ESI-MS spectrum of complex **1** in water. m/z = 388.6 corresponds to $[Fe^{III}(bbpya)-\mu-O-Fe^{III}(bbpya)]^{2+}$; calcd.: m/z = 388.1

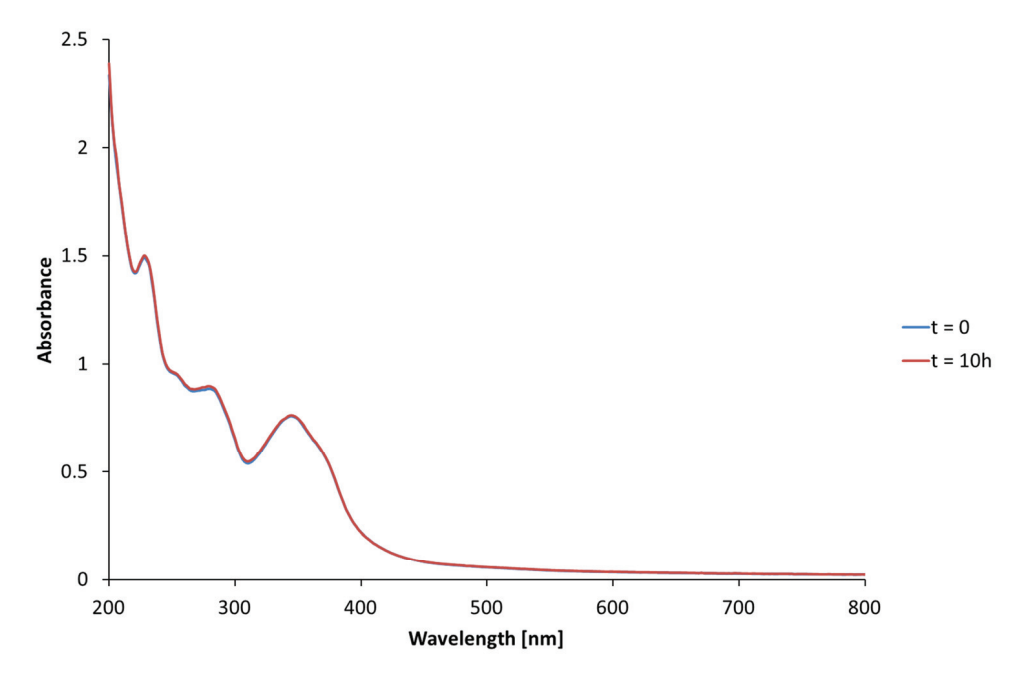


Figure B.5: UV-vis spectra of complex 1 in water at t = 0 (blue line) and t = 10 h (red line)

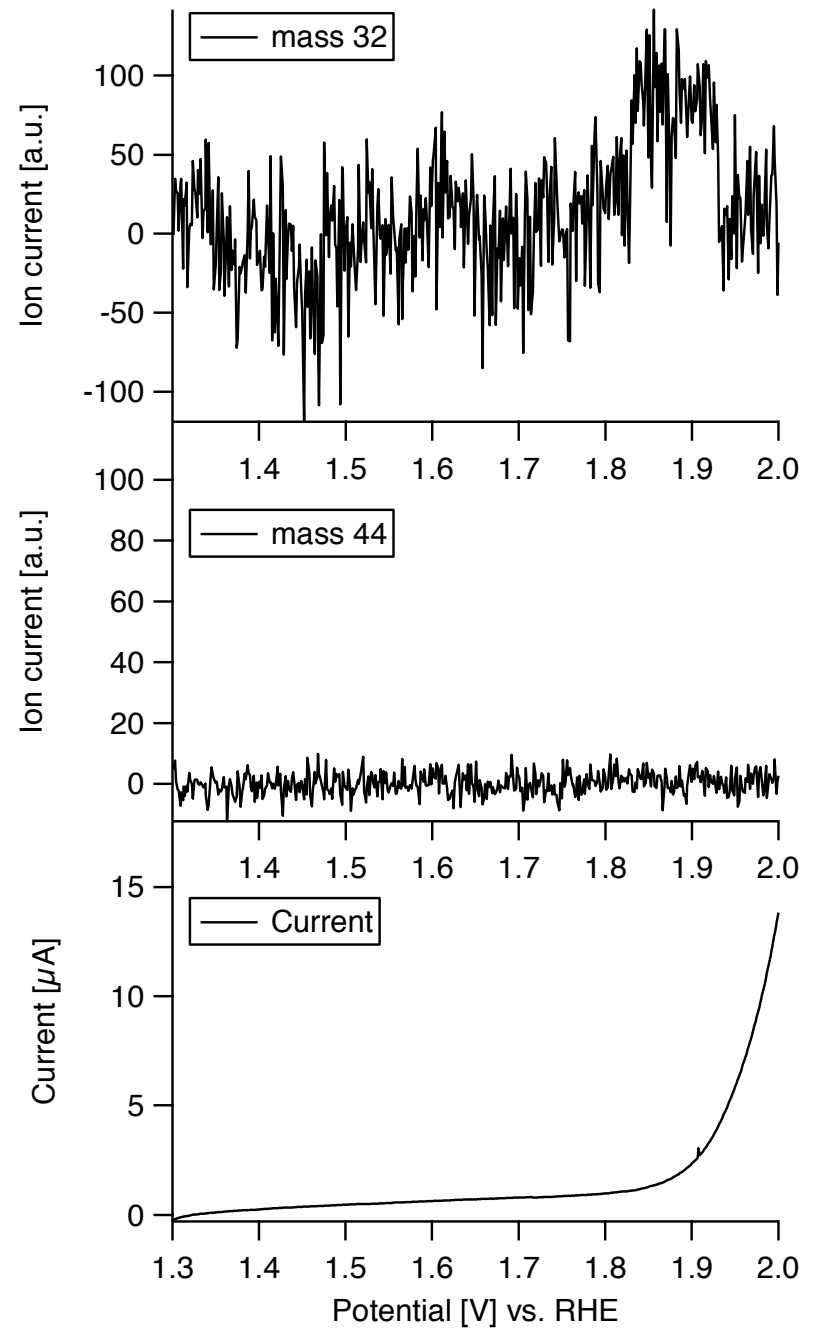
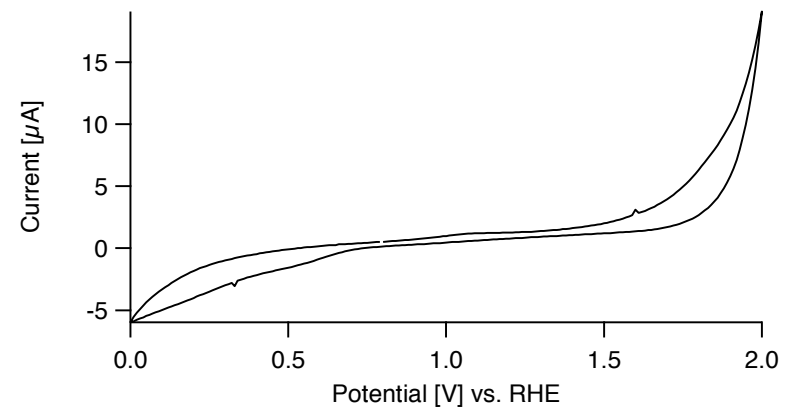


Figure B.6: Results of an OLEMS measurement of a gold working electrode in a $0.1 \text{ M Na}_2\text{SO}_4$ solution in the absence of complex **1** (scan range, 1.3-2.0V vs. RHE, scan rate 1 mV/s, starting at 1.3 V vs. RHE). Shown is the forward scan of a CV experiment with the m/z trace for O_2 (top), the m/z trace for O_2 (middle) and the corresponding current (bottom).



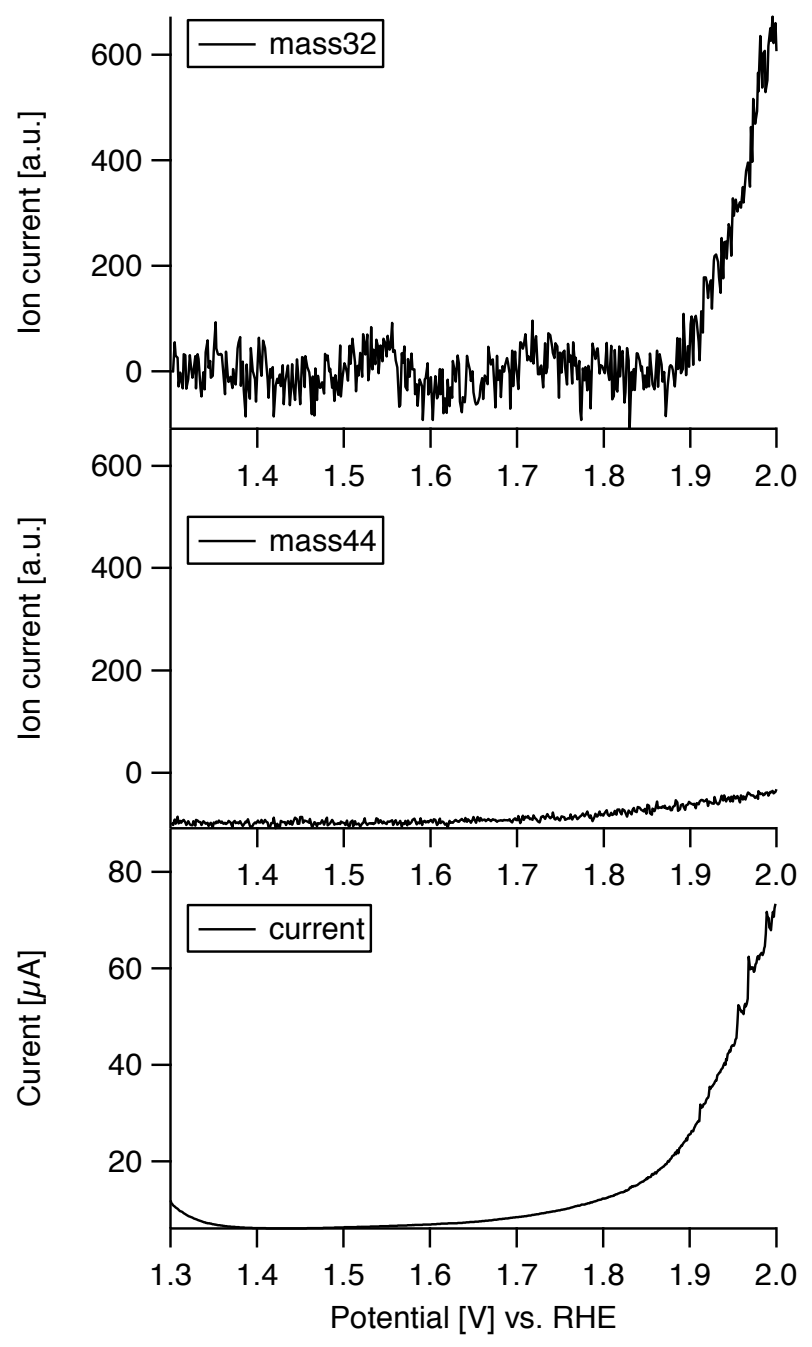


Figure B.8: Results of OLEMS measurement of 1 mM Fe(OTf)₂ on a PG working electrode in a 0.1 M Na₂SO₄ solution (scan range, 1.3-2.0V vs. RHE, scan rate 1 mV/s, starting at 1.3 V vs. RHE). Shown is the forward scan of a CV experiment with the m/z trace for O₂ (top), m/z trace for CO₂ (middle) and the corresponding current (bottom).



Figure B.9: Modified EQCM cell: the top part of the cell was made taller to allow for degassing of the electrolyte solution by bubbling argon. Additionally, a small hole was added to serve as a gas inlet to keep the cell under argon flow during experiments, preventing air from entering.

B.2 Calculation of turnover frequencies

The formula for the calculation of the turnover frequencies in the text of chapter 3 is derived from equation 1 below. With R being the universal gas constant, T being the temperature in Kelvin, F being the Faraday constant and ν being the scan rate in V/s, for a four-electron process (n = 4) such as water oxidation at a room temperature of 293 K this simplifies to equation 2 where the TOF is the same as k_{obs} .

$$\frac{i_{cat}}{i_p} = \frac{n}{0.4463} \sqrt{\frac{RTk_{obs}}{F\nu}} \tag{1}$$

$$TOF = 0.4848 \cdot \nu \left(\frac{i_{cat}}{i_p}\right)^2 \qquad (2)$$

To calculate the turnover frequency, we used the current of oxidation wave X (cf. Fig. 3.2 and Fig. 3.5, chapter 3) for i_p to calculate the TOF for i_{cat} at different potentials. Background correction was performed to account for the contribution of non-catalytic current to i_{cat}. For the case of complex 1 with a PG working electrode we calculated icat by subtracting the current of a blank measurement with the same electrode in the absence of complex 1 from the current measured in the presence of complex 1. For the case of a gold working electrode, however, the contribution of background processes is clearly overlapping with the onset of oxygen evolution, leading to a significant overestimation of i_{cat} at 1.9 and 2.0 V (cf. Fig. 3.2, chapter 3). To eliminate contributions from background processes from i_{cat}, the potential was cycled 5 times between 1.3 and 2.0 V at a scan rate of 10 mV/s with a gold working electrode in the presence of complex 1. By keeping the potential above 1.3 V, gold oxide reduction is prevented which means that gold oxidation only contributes to the first scan of the experiment. Thus, to determine icat at 1.9 and 2.0 V, the current of the second scan of the CV experiment between 1.3 and 2.0 V with a gold working electrode in the presence of complex 1 was considered, from which the current of the second scan of an analogous blank experiment with the same gold working electrode in the absence of complex 1 was subtracted.

В

B.3 Single crystal X-ray crystallography (complex 1)

All reflection intensities were measured at 110(2) K using a SuperNova diffractometer (equipped with Atlas detector) with Cu $K\alpha$ radiation (λ = 1.54178 Å) under the program CrysAlisPro. The same program was used to refine the cell dimensions and for data reduction. The structure was solved with the program SHELXS-2014/7 and was refined on F^2 with SHELXL-2014/7. Analytical numeric absorption correction using a multifaceted crystal model was applied using CrysAlisPro. The temperature of the data collection was controlled using the system Cryojet (manufactured by Oxford Instruments). The H atoms were placed at calculated positions (unless otherwise specified) using the instructions AFIX 43 or AFIX 137 with isotropic displacement parameters having values 1.2 or 1.5 Ueq of the attached C or N atoms. The H atoms attached to O2 and O3 (coordinated MeOH molecules) were found from difference Fourier maps, and their coordinates were refined freely. The structure is mostly ordered.

Additional Notes:

- 1. One of the four crystallographically independent triflate counter-ions in the asymmetric unit is found to be disordered over two orientations, and the occupancy factor of the major component of the disorder refines to 0.788(4).
- 2. The crystal that was mounted on the diffractometer was twinned. The twin relationship corresponds to a twofold axis along the reciprocal vector -0.7007a* + 0.7134b* -0.0020c*. The BASF scale factor refines to 0.2164(12). All necessary details about the twin data reduction have been embedded in the .cif file.

Table B.1: Crystallographic data of complex ${\bf 1}$

T	
Identification code	1
Crystal data	
Chemical formula	$C_{42}H_{38}Fe_2N_{10}O_3\cdot 4(CF_3O_3S)$
$M_{\rm r}$	1438.80
Space group	Triclinic, P-1
Temperature (K)	110
a, b, c (Å)	11.9405 (5), 12.2853 (4), 20.3054 (6)
α, β, γ (°)	103.183 (3), 102.560 (3), 98.477 (3)
V (Å ³)	2769.26 (18)
Z	2
Radiation type	Cu <i>Κ</i> α
μ (mm ⁻¹)	6.67
Crystal size (mm)	$0.21 \times 0.17 \times 0.10$
Data callegation	
Data collection	
Diffractometer	SuperNova, Dual, Cu at zero, Atlas
Absorption correction	Analytical <i>CrysAlis PRO</i> 1.171.38.41 Analytical numeric absorption correction using a multifaceted crystal model based on expressions derived by R.C. Clark & J.S. Reid. ^[2, 4] Empirical absorption correction using spherical harmonics, implemented in SCALE3 ABSPACK scaling algorithm.
T_{\min} , T_{\max}	0.400, 0.650
No. of measured, independent and observed $[I > 2\sigma(I)]$ reflections	35916, 12230, 8520
R _{int}	0.056
$(\sin \theta/\lambda)_{\text{max}}$ (Å ⁻¹)	0.616

Appendix B

Refinement	
$R[F^2 > 2\sigma(F^2)], wR(F^2), S$	0.054, 0.140, 0.92
No. of reflections	12230
No. of parameters	878
No. of restraints	267
H-atom treatment	H atoms treated by a mixture of independent and constrained refinement
$\Delta \rho_{\text{max}}$, $\Delta \rho_{\text{min}}$ (e Å ⁻³)	0.89, -0.68

Table B.2: Relevant bond distances and angles for complex ${\bf 1}$

Distan	ces (Å)	
Fe1-N1	2.117(4)	
Fe1-N2	2.124(4)	
Fe1-N4	2.116(4)	
Fe1-N5	2.140(4)	
Fe1-O1	1.782(3)	
Fe1-O2	2.147(3)	
Fe2-N6	2.133(4)	
Fe2-N7	2.114(4)	
Fe2-N10	2.125(4)	
Fe2-N11	2.112(4)	
Fe2-O1	1.778(3)	
Fe2-O3	2.147(3)	
C1-C25	4.339(7)	
C4-C27	3.829(8)	
C6-C30	3.515(6)	
C10-C31	3.365(6)	
C11-C35	3.445(6)	
C14-C37	3.376(6)	
C16-C40	3.552(6)	
Bond angles (°)		
N1-Fe1-N2	78.15(15)	
N2-Fe1-N4	87.12(15)	
N4-Fe1-N5	78.74(15)	
N1-Fe1-N5	114.25(15)	
N6-Fe2-N7	78.46(15)	
N7-Fe2-N10	86.96(15)	
N10-Fe2-N11	78.42(14)	
N6-Fe2-N11	114.57(15)	
Fe1-O1-Fe2	155.78(18)	
Torsion angles (°)		
C19-C12-C9-C2	-16.4(1)	
C39-C32-C29-C22	-3.0(1)	
N3-Fe1-Fe2-N9	-44.0(1)	

E

B.4 References

- [1] J. M. Saveant; E. Vianello, *Electrochim. Acta* **1965**, *10*, 905-920.
- [2] O. D. Rigaku *CrysAlisPro*, version 1.171.38.41; Rigaku Oxford Diffraction: Oxford, UK, 2015.
- [3] G. M. Sheldrick, Acta Crystallogr., Sect. C: Struct. Chem. 2015, 71, 3-8.
- [4] R. C. Clark; J. S. Reid, Acta Crystallogr., Sect. A: Found. Adv. 1995, 51, 887-897.

Appendix C

Supplementary information for Chapter 4



Figure C.1: Formation of solid precipitate inside the electrochemical cell during electrochemical measurements of complex $\bf 2$ in $\bf 0.1~M~HClO_4$

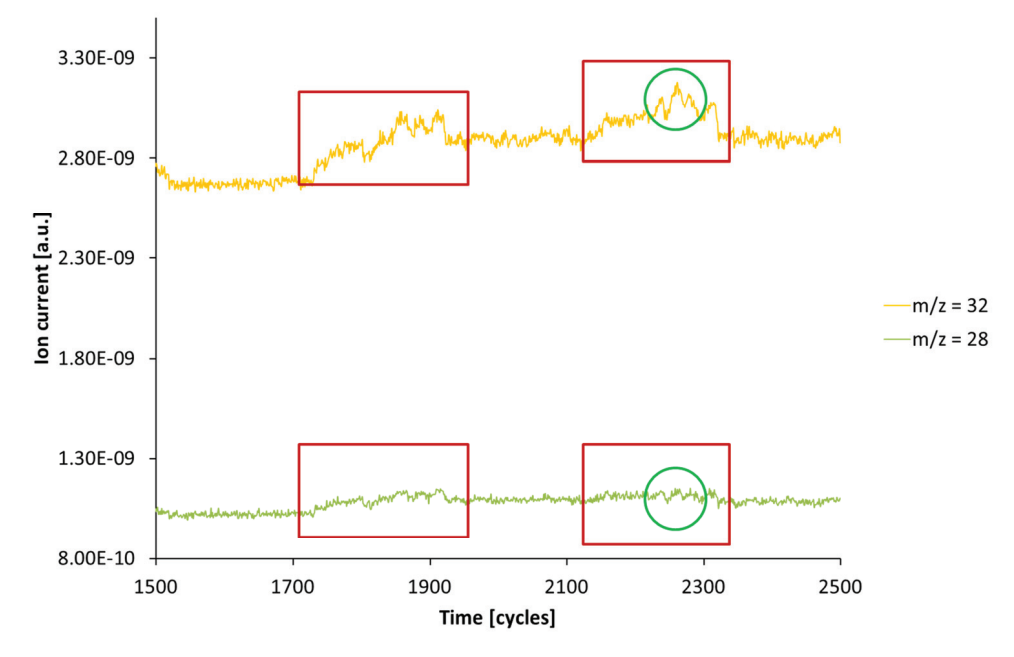


Figure C.2: Examples of the artefacts present in OLEMS measurements. The yellow trace represents the response for m/z = 32, the green trace represents the response for m/z = 28. The red boxes indicate noise which can be seen in both mass traces and therefore does not correspond to actual oxygen evolution while the green circles show real oxygen signals caused by complex **2** which are therefore absent in the trace of m/z = 28.

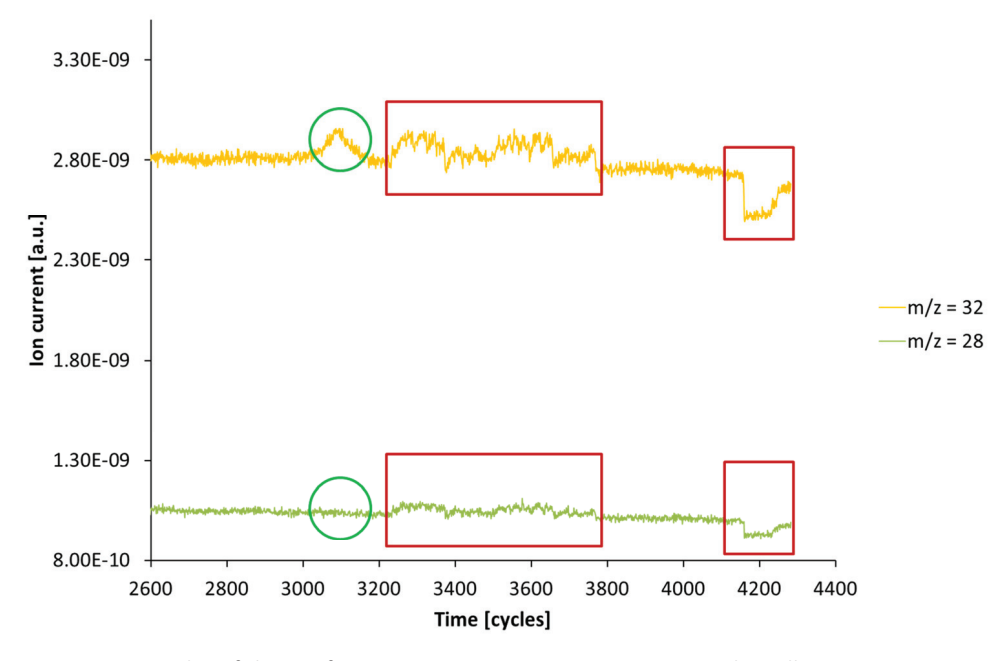


Figure C.3: Examples of the artefacts present in OLEMS measurements. The yellow trace represents the response for m/z = 32, the green trace represents the response for m/z = 28. The red boxes indicate noise which can be seen in both mass traces and therefore does not correspond to actual oxygen evolution while the green circles show real oxygen signals caused by complex **2** which are therefore absent in the trace of m/z = 28.

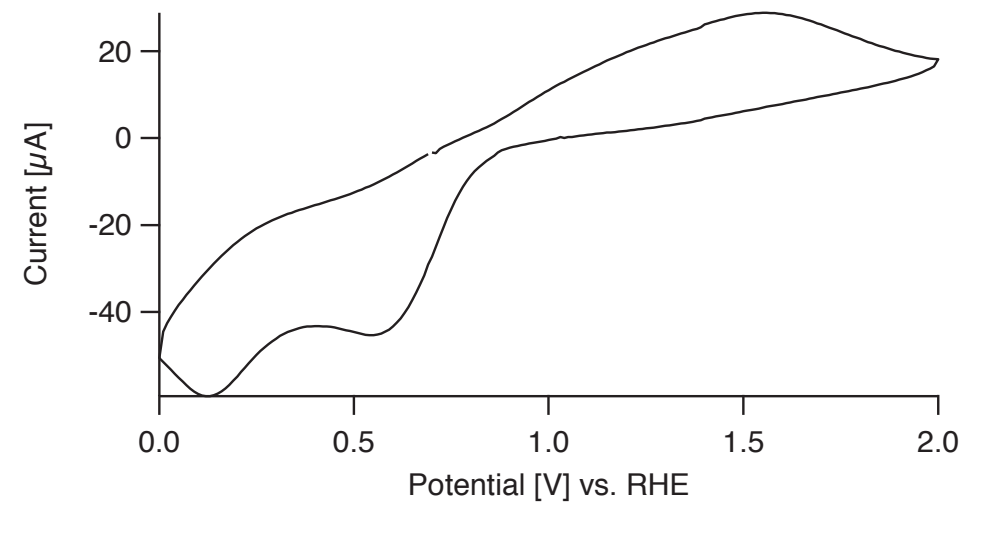


Figure C.4: Voltammogram of 1.1 mM complex 3 in a 0.1 M Na_2SO_4 electrolyte solution, recorded between 0.0 and 2.0 V vs. RHE at 100 mV/s with an ITO working electrode, starting at 0.7 V vs. RHE.

Inleiding

Een van de fundamentele uitdagingen voor de wetenschap in de 21^e eeuw is het vinden van nieuwe en duurzame manieren om energie te produceren. Op dit moment is energieproductie nog steeds grotendeels afhankelijk van het niet duurzame verbranden van fossiele brandstoffen. Niet alleen zijn de reserves van fossiele brandstoffen beperkt, maar door het verbranden van fossiele brandstoffen komt CO₂ vrij in de atmosfeer wat bijdraagt aan de wereldwijde klimaatverandering. Hoewel er verschillende duurzame alternatieven voor fossiele brandstoffen zijn, zoals wind- en geothermische energie, is zonne-energie de enige bron van duurzame energie die in voldoende mate beschikbaar is om op een wereldwijde schaal energie te leveren.^[1]

Om te allen tijde de beschikbaarheid van energie uit zonlicht te garanderen is het belangrijk om zonne-energie niet alleen op te vangen maar deze energie daarnaast ook op te slaan. Terwijl de omzetting van zonne-energie naar elektriciteit technisch al mogelijk is, hebben opslagmedia voor elektriciteit, zoals batterijen, energiedichtheden die orders van grootte lager liggen dan de energiedichtheden van conventionele chemische brandstoffen. ^[2] Om zonlicht efficiënt te kunnen opslaan als een chemische brandstof, zijn nieuwe technologieën nodig die de omzetting van zonne-energie naar een chemische brandstof mogelijk maken.

Een van de meest veelbelovende manieren om dit doel te bereiken is de splitsing van water in waterstofgas en zuurstofgas. Het waterstofgas dat in een dergelijk proces wordt gegenereerd kan vervolgens rechtstreeks worden gebruikt als brandstof in brandstofceltoepassingen, dan wel worden gebruikt in bijvoorbeeld de reductie van CO₂ naar een meer conventionele, koolstof-gebaseerde brandstof. De productie van zuurstof als het enige bijproduct zou een dergelijk proces zeer milieuvriendelijk maken.

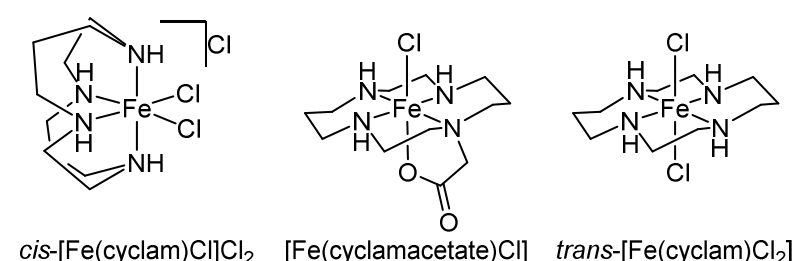
In vergelijking met de productie van waterstofgas uit water is de productie van zuurstofgas uit water – ook bekend als wateroxidatie – duidelijk het meer complexe proces. Ondanks veel vooruitgang op dit gebied na decennia van onderzoek, is de ontwikkeling van een geschikte katalysator voor de wateroxidatiereactie nog steeds een grote uitdaging. De beste katalysatoren die tot nu toe in de literatuur zijn gerapporteerd, zijn gebaseerd op zeer schaarse en

dure materialen zoals iridium en ruthenium, wat deze katalysatoren ongeschikt maakt voor toepassingen op een grote schaal.^[3]

Daarnaast wordt in een groot deel van het onderzoek op het gebied van wateroxidatie gebruik gemaakt van chemische oxidatoren om nieuwe katalysatoren te testen, hoewel de resultaten die zijn verkregen in de aanwezigheid van zulk chemische oxidatoren niet betrouwbaar kunnen worden vertaald naar echte toepassingen. Het onderwerp van het in dit proefschrift beschreven onderzoek is daarom de ontwikkeling van nieuwe, op ijzer gebaseerde katalysatoren voor de zuurstofevolutiereactie en het bestuderen van hun katalytische eigenschappen onder relevante omstandigheden met behulp van een brede selectie aan elektrochemische methoden in plaats van chemische oxidatoren.

Hoofdstuk 2

In hoofdstuk 2 beschrijven wij de studie van de elektrocatalytische activiteit in de wateroxidatiereactie voor drie verschillende ijzercomplexen op basis van het macrocyclische tetraaza-type ligand cyclam (Fig. S.1) met behulp van online elektrochemische massaspectrometrie (OLEMS). Het gebruik van OLEMS in combinatie met klassieke elektro-analytische technieken maakt het mogelijk onderscheid te maken tussen concurrerende reacties zoals wateroxidatie en de vorming van koolstofdioxide door oxidatieve ontledingsreacties van de gebruikte liganden bij hoge elektrochemische potentialen.



Figuur S.1: Structuren van de drie complexen cis-[Fe(cyclam)Cl₂]Cl, [Fe(cyclamacetaat)Cl] en trans-[Fe(cyclam)Cl₂]

Het complex *cis*-[Fe(cyclam)Cl₂]Cl blijkt een active wateroxidatiekatalysator te zijn. Dit resultaat komt overeen met resultaten uit de literatuur die voorspellen dat ijzercomplexen gebaseerd op neutrale aminoliganden en met twee vrije coördinatieplekken in *cis*-configuratie katalytisch actief zijn voor wateroxidatie.^[5] Het complex [Fe(cyclamacetaat)Cl], dat een extra 5^e donorligand heeft in de vorm

van een acetaatgroep in axiale positie, is ook een actieve katalysator voor de wateroxidatiereactie. [Fe(cyclamacetaat)Cl] is dus een zeldzaam voorbeeld van een elektrokatalysator voor de wateroxidatiereactie met slechts een enkele vrije coördinatieplek die actief is in een waterig medium. Het complex *trans*-[Fe(cyclam)Cl₂], waarvoor geen katalytische activiteit werd voorspeld, toont inderdaad nauwelijks katalytische activiteit. Cyclische voltammetrie-experimenten tonen aan dat voor de twee katalytisch actieve complexen, *cis*-[Fe(cyclam)Cl₂]Cl en [Fe(cyclamacetaat)Cl], de Fe^{II}/Fe^{III} redoxovergangen bij een lagere potentiaal liggen dan voor het inactieve complex *trans*-[Fe(cyclam)Cl₂]. Dit resultaat suggereert dat een sterke correlatie bestaat tussen de elektronische structuur van het ijzercentrum en de waargenomen wateroxidatieactiviteit.

De vorming van CO₂, die zichtbaar is in alle OLEMS-experimenten, roept vragen op over de stabiliteit van de complexen onder sterk oxiderende omstandigheden. Het gebruik van een op koolstof gebaseerde werkelektrode maakt het echter moeilijk om het complex of het elektrodemateriaal eenduidig als de bron van het gevormde CO₂ aan te wijzen. Het gebruik van andere elektrodematerialen zoals goud of platina is in deze studie niet mogelijk door de aanwezigheid van chlorideionen in elk van de gebruikte complexen. Deze problemen worden behandeld in het vervolgproject beschreven in hoofdstuk 3.

Hoofdstuk 3

Op basis van de resultaten uit hoofdstuk 2 hebben wij een 2^e generatie ijzerbevattende wateroxidatiekatalysator ontworpen en gesynthetiseerd, gebaseerd op het ligand *N,N*-bis(2,2'-bipyrid-6-yl)amine (Hbbpya).

De aromatische structuur van het Hbbpya ligand zou een betere bescherming tegen oxidatieve ontleding moeten bieden vergeleken met de alifatische structuur van het cyclam ligand. Verder bevat het ligand geen β-waterstofatomen waarvan bekend is dat ze gevoelig zijn voor ontledingsreacties onder sterk oxiderende omstandigheden. [6] Van de aromatische ligandstructuur wordt verwacht dat deze meer elektronendichtheid doneert dan cyclam, en met de centrale aminogroep een mogelijkheid biedt om additionele functionele groepen te verankeren. Omdat het resulterende ijzercomplex geen halides bevat is de katalysator compatibel met een brede selectie aan elektrodematerialen. Dit biedt ons de mogelijkheid om de mogelijke invloed van het elektrodemateriaal op de resulterende elektrochemie te bestuderen. bepaling De van de structuur door middel

röntgenkristalstructuuranalyse toont aan dat het resulterende complex $[(MeOH)Fe(Hbbpya)-\mu-O-(Hbbpya)Fe(MeOH)](OTf)_4$ een dimeer is (Fig. S.2).

Figuur S.2: Structuur van het complex [(MeOH)Fe(Hbbpya)–μ-O–(Hbbpya)Fe(MeOH)](OTf)₄

Met behulp van online elektrochemische massaspectrometrie (OLEMS) kon de katalytische activiteit van het complex voor elektrokatalytische wateroxidatie worden aangetoond. Verrassend genoeg vertoont het complex een significant lagere katalytische overpotentiaal in combinatie met een werkelektrode gebaseerd op grafiet dan voor andere elektrodematerialen. Dit resultaat wijst op specifieke interacties tussen het complex en sp² koolstofoppervlakken, bijvoorbeeld in de vorm van π - π interacties tussen het Hbbpya ligand in het complex en het oppervlak van een elektrode bestaand uit pyrolytisch grafiet of glassy carbon. Cyclische voltammetrie-experimenten tonen aan dat het complex omkeerbare structurele veranderingen ondergaat bij hoge potentialen: de oorspronkelijke structuur van het complex wordt vervolgens geregenereerd bij terugkeer naar een lagere potentiaal. Dit zou het resultaat kunnen zijn van een dissociatie van het complex bij hoge potentialen, gevolgd door een herdimerisatie bij terugkeer naar lagere potentialen. De resultaten van elektrochemische kwartskristal-microbalansexperimenten sluiten uit dat de katalyse verloopt via de depositie van katalytisch-actief materiaal op het elektrodeoppervlak.

Hoofdstuk 4

Het complex α -[Fe(bpmcn)(OTf)₂] (bpmcn = N,N'-dimethyl-N,N'-bis(2-pyridylmethyl)-cyclohexaan-1,2-diamine) werd voor het eerst gerapporteerd in 2011 door Fillol et. al als een zeer actieve, ijzerbevattende katalysator voor de wateroxidatiereactie. [5] Sindsdien geldt het systeem als een standaard voor op ijzer gebaseerde wateroxidatiekatalysatoren. De katalytische activiteit van het

complex is tot nu toe echter alleen bestudeerd met behulp van chemische oxidatoren. Daaropvolgende rapporten hebben aangetoond dat het complex in aanwezigheid van de chemische oxidator cerium(IV) een Fe–O–Ce tussenproduct vormt.^[4] Dit resultaat roept vragen op over het mechanisme van wateroxidatie en of het complex ook actief is in afwezigheid van chemische oxidatoren.

In hoofdstuk 4 beschrijven wij de resultaten van elektro-analytisch onderzoek van twee isotopologen van hetzelfde complex – één met protium, het andere met deuterium op de methyleenbruggen in het ligand. Verder vergelijken wij deze twee α -[Fe(bpmcn)](OTf)₂ isotopologen met het niet-gedeutereerde Fe^{III} analoog α -[Fe(bpmcn)Cl₂]Cl (Fig. S.3)

Figuur S.3: Structuren van de drie complexen beschreven in hoofdstuk 4

De reactiviteit van deze complexen voor wateroxidatie onder elektrochemische omstandigheden wordt vergeleken met hun activiteit onder chemisch-gedreven omstandigheden, in het bijzonder met betrekking tot het verschil in stabiliteit tussen de H_4 en de D_4 analoog van α -[Fe(bpmcn)(OTf)₂]. In aanwezigheid van een overmaat cerium(IV) vertoonden de twee isotopologen een verschil in turnover nummer van een factor 4-5.

Hoewel de resultaten aantonen dat alle drie complexen bij potentialen $\geq 1.8 \, \text{V}$ actieve wateroxidatiekatalysatoren zijn is hun prestatie niet uitzonderlijk hoog in vergelijking met de andere ijzerbevattende elektrokatalysatoren die in dit proefschrift worden beschreven. Verder werd er geen significant verschil in stabiliteit tijdens elektrokatalyse gevonden tussen de H_4 en de D_4 analoog van α -[Fe(bpmcn)(OTf) $_2$]. Ten slotte werden de twee α -[Fe(bpmcn)(OTf) $_2$] isotopologen bestudeerd met verschillende elektrodematerialen en vertoonden ze een veel gecompliceerder gedrag in combinatie met een werkelektrode van goud dan met een werkelektrode van pyrolytisch grafiet. De redenen voor dit gedrag zijn nog onduidelijk en vereisen verdere studie.

Hoofdstuk 5

De resultaten die worden beschreven in de hoofdstukken 3 en 4 geven aan dat interacties tussen het oppervlak van de werkelektrode en een homogene katalysator in oplossing sterke invloed kunnen hebben op de resulterende elektrochemie van de katalysator. In hoofdstuk 5 wordt de studie naar de invloed van de interacties tussen metaalcomplexen in oplossing en het oppervlak van werkelektroden van goud en pyrolytisch grafiet (PG) bekeken met betrekking tot de gevolgen voor het elektrodemateriaal. In het geval van een PG-elektrode lijkt de aanwezigheid van ijzercomplexen in oplossing de ontwikkeling van CO₂ uit het elektrodemateriaal al bij een lager potentiaal mogelijk te maken in vergelijking met controle-experimenten in afwezigheid van metaalcomplexen.

In het geval van een goudelektrode leiden cyclische voltammetrie-experimenten in de aanwezigheid van $[(MeOH)Fe(Hbbpya)-\mu-O-(Hbbpya)Fe(MeOH)](OTf)_4$ of $[Ru(tpy)(bpy)(H_2O)](OTf)_2$ (Hbbpya = N,N-bis(2,2'-bipyrid-6-yl)amine, bpy = bipyridine en tpy = terpyridine) tot significante veranderingen in de elektrochemie van goud. Na meerdere scans in een cyclisch voltammetrie-experiment met een blanco elektrolytoplossing herstelt het goudoppervlak zich en gedraagt de goudelektrode zich weer als voorheen. De aard van deze verandering is nog niet duidelijk en de mechanismen erachter vereisen verder onderzoek.

Voor beide elektrodematerialen zijn de effecten die worden veroorzaakt door de aanwezigheid van metaalcomplexen in oplossing potentieel zeer significant, vooral met betrekking tot pogingen om verschillende katalysatoren goed met elkaar te kunnen vergelijken.

Referenties

- [1] N. S. Lewis; D. G. Nocera, *Proc. Natl. Acad. Sci. U. S. A.* **2006**, *103*, 15729-15735.
- [2] D. G. Nocera, ChemSusChem 2009, 2, 387-390.
- [3] J. D. Blakemore; R. H. Crabtree; G. W. Brudvig, *Chem. Rev.* **2015**, *115*, 12974-13005.
- [4] Z. Codola; L. Gomez; S. T. Kleespies; L. Que, Jr.; M. Costas; J. Lloret-Fillol, *Nat. Commun.* **2015**, *6*, 5865.
- [5] J. L. Fillol; Z. Codola; I. Garcia-Bosch; L. Gomez; J. J. Pla; M. Costas, *Nat. Chem.* **2011**, *3*, 807-813.
- [6] T. J. Collins, Acc. Chem. Res. 1994, 27, 279-285.

List of publications

'Evaluation of iron-based electrocatalysts for water oxidation — an on-line mass spectrometry approach'

K. G. Kottrup; D. G. H. Hetterscheid, Chem. Commun. 2016, 52, 2643-2646.

'Detangling Catalyst Modification Reactions from the Oxygen Evolution Reaction by Online Mass Spectrometry'

P. Abril; M. P. del Río; C. Tejel; T. W. G. M. Verhoeven; J. W. H. Niemantsverdriet; C. J. M. Van der Ham; <u>K. G. Kottrup</u>; D. G. H. Hetterscheid, *ACS Catal.* **2016**, *6*, 7872-7875.

'The synthesis, characterization, X-ray structure and magnetism of dinuclear-based bis[I-(1,1,3,3-tetracyano-2-ethoxypropenido-j2N,N0) (1,1,3,3-tetracyano-2-ethoxypropenido-jN)(2,20-bipyridine)copper(II)] organized in alternating chains via semi-coordinating Cu–N distances'

A. Addala; F. Setifi; K. G. Kottrup; C. Glidewell; Z. Setifi; G. Smith; J. Reedijk, *Polyhedron* **2015**, *87*, 307-310.

'Catalytic activity of an iron-based water oxidation catalyst – substrate effects of graphitic electrodes'

<u>K. G. Kottrup</u>; S. D'Agostini; P. H. van Langevelde; M. A. Siegler; D. G. H. Hetterscheid, *ACS Catal.* accepted for publication

In preparation

K. G. Kottrup; S. D'Agostini; J. L. Fillol; M. Costas; D. G. H. Hetterscheid, in preparation

Curriculum Vitae

Konstantin Kottrup was born in Berlin, Germany on the 11th of February in 1988. In 2007 he graduated from Goethe-Gymnasium high school. Later that year he started studying chemistry at the Humboldt Universität zu Berlin. During his studies he performed two research internships at the Humboldt Universität, in which he worked on the selective cleavage of disulfide bridges in immunoglobulin-G antibodies and on the activation of small molecules with fluorinated pincer-complexes of palladium and iridium. He also supervised undergraduate students in practical and theoretical courses on analytical chemistry as part of his position as a teaching assistant. In 2012 he graduated after finishing his diploma thesis (equivalent of MSc thesis) under the supervision of Prof. Dr. Thomas Braun. The topic of his diploma thesis was the activation of Si–Si bonds at platinum and palladium complexes.

In 2013 he started his PhD research in the group "Metals in Catalysis, Biomimetics & Inorganic Materials" (MCBIM) at Leiden University. The results of the work which was supervised by Prof. Dr. Lies Bouwman and Dr. Dennis Hetterscheid are described in this thesis. During his time as a PhD researcher, he attended the NIOK course "Catalysis, An Integrated Approach" (CAIA) and the Leiden University graduate school courses on time management, scientific integrity, effective communication and scientific writing.

Parts of the results reported in this thesis were presented at the following meetings and conferences:

- Netherlands' Chemistry and Catalysis Conference (NCCC) in Noordwijkerhout in 2014 (poster), 2015 (poster) and 2016 (oral)
- BioSolar Cells meeting in Amsterdam in 2014 (oral)
- International Solar Fuels (ISF) conference in Uppsala, Sweden in 2015 (poster)
- HRSMC symposium in Amsterdam in 2015 (poster)
- NWO CHAINS conference in Veldhoven in 2015 (oral)
- International Society of Electrochemistry (ISE) meeting in Den Haag in 2016 (poster)
- COST action CARISMA meeting in Lisbon, Portugal in 2017 (oral)